ภาคผนวก

ภาคผนวกนี้เป็นสำเนาของบทความ ที่ได้รับการตีพิมพ์ในวารสารทางวิชาการจำนวน 5 บทความ.

Electric Field Analysis using Image Charges of Spheroidal Harmonics and its Application to the Calculation of Field in Cavities

Boonchai Techaumnat
Department of Electrical Engineering, Chulalongkorn University
Phyathai road, Pathumwan, Bangkok 10330, Thailand

and **Tadasu Takuma**
Tokyo Denki University
2-2 Kanda-Nishiki-cho, Chiyoda-ku, Tokyo 201-8547, Japan

ABSTRACT

This paper describes a method of electric field analysis for configurations consisting of oblate spheroidal objects. In the method, electric potential is expressed as a sum of oblate spheroidal harmonics. The method utilizes the re-expansion and the image schemes of a dielectric oblate spheroid and a conducting plane to determine the solution of potential that satisfies all the boundary conditions involved. Electric field is calculated for an oblate spheroidal void enclosed in a solid dielectric near an electrode. The object of the calculation is to clarify the electric field inside the void which varies with (1) the separation between the void and the electrode, (2) the ratio of the major to minor axes of the void and (3) the dielectric constant of the solid dielectric. The results show that the effect of the electrode on the field inside the void is negligible when the separation is greater than the major semi-axis of the void. The presence of the electrode near the void mitigates the electric field on the axis of symmetry of the void. However, higher field stress exists at the region away from the axis, and the field maximum is not significantly reduced by decreasing the separation, in particular for flatter voids. In order to present the potential induced by the void, higher order multipoles must be incorporated. The effect of the planar electrode on the equivalent multipole moments of the void is also discussed.

Index Terms — **Electric fields, spheroids, ellipsoids, Laplace equations, cavities, bubbles, electrodes, electrostatic analysis.**

1 INTRODUCTION

A variety of numerical methods, such as the finite element method or the boundary element method, can be used for electric field calculation. However, they may accompany considerable error in cases of a curved surface near another surface [1]. On the other hand, the analytical approach permits of a strictly correct solution of the electric field. Analytical methods are also convenient when the equivalent charges, the electrostatic force, or the interaction between objects are of interest [2, 3]. The present work explains an analytical method based on the spheroidal harmonics, which can be used for calculating electric field in configurations of oblate spheroidal objects in a similar manner as the method presented for a sphere [4, 5] and that for a prolate spheroid [6]. A re-expansion formula is applied to the image charges of spheroidal harmonics in order to obtain multipole images representing the potential induced by the spheroidal object. The analytical method can realize high accuracy of calculation results even when a spheroid is located near an electrode or another spheroid.

Using the method, we study the distribution of the electric field in the configuration of an oblate spheroidal void in a solid dielectric. Solid dielectrics play an important role in high-voltage insulation systems. They are used in any systems as the main insulating material or as supporting components. Solid dielectrics have high dielectric strength, in comparison with gaseous or liquid materials. However, the presence of cavities (voids) in a solid dielectric is critical to the insulating performance. The electric field in a void is higher than that in the enclosing solid medium because of the lower dielectric constant of the medium inside the void, usually gaseous one. The fundamental characteristics of electric field in composite dielectrics are explained in [7]. When the electric field is

---

Manuscript received on 22 March 2012, in final form 22 July 2012.

excessively high, partial discharge (PD) initially takes place in the void. The PD activity involves chemical, mechanical, and thermal processes, which can cause deterioration in the solid dielectric. In critical cases, PDs may result in breakdown or insulation failure of the insulation system [8, 9].

The electric field inside a void embedded in a solid dielectric has been studied in a number of works, as the field strength is a decisive factor for PD inception. In early studies, Salvage analyzed the electric field in an oblate spheroidal and elliptic cylindrical void located at the middle point between parallel plane electrodes. Spheroidal harmonics were utilized to obtain the approximate solution when the diameter of the spheroidal void was not greater than the distance between the electrodes. The electric field along the axis of symmetry of the void was investigated for various separations between the void and the electrodes [10]. The results clearly show the influence of the void shape on the electric field. The analytical approach was applied to a similar configuration of a conducting spheroid between parallel electrodes [11]. The field variation with the dimensions of a circular cylindrical void and the electrode spacing was calculated by using the finite difference method [12]. It was found that the mean electric field on the void axis increased with the ratio of the radius to the axial length of the void. Chang et al. calculated the electric field in a void using the finite element method for circular cylindrical shapes. They reported the effect of the void orientation on the electric field including the cases where multiple voids exist near each other [13]. The maximum electric field in the void decreased with increasing number of voids in series. Note that a rather high dielectric constant values (10–10000) of the solid dielectric was used in this work. Ghourab and El-Makkawy applied the charge simulation method to the calculation of the mean electric field in spherical voids [14]. They reported the effect of the dielectric constant on the maximum electric field along the void axis. Also investigated are the location of a void, and the orientation of a void in its proximity. Hossam-Eldin et al. used the indirect boundary element method to analyze the electric field in configurations of a spherical void and those of a circular cylindrical void [15]. Their results showed again a variation of the maximum field stress on the void axis with the shape and the position of the void. Field behavior was found to be similar between a spherical void and a corresponding cylindrical one.

The solution of electrostatic potential in a void also has an application in the analysis of transient behavior of charge associated with partial discharge in a void [16-19]. Ellipsoidal and spheroidal voids were treated in the works with the simplification that omitted the influence of electrodes on the potential and neglected multipole potential. In the other work related to the field calculation of a spheroidal object, an on-axis field approximation was given for evaluating electric field outside a conducting prolate spheroid under a uniform field [20], however, only for the case of an isolated spheroid.

As mentioned above, the previous works mainly treated spherical voids or cylindrical voids. For cylindrical voids, small height-to-width ratios were used because the field is higher in the void than in the surrounding medium. On the other hand, there is still lack of detailed analysis on the field behavior for a spheroidal void, in particular when the void is located in the vicinity of an electrode. Note that in this case, the symmetrical property of potential in the vertical direction is not applicable; therefore, the simplification used in [10, 11] is not appropriate to obtain the harmonic solutions. The objective of the calculation in the present work is to clarify the field behavior in a void in the PD-free condition, as it contributes to the space charge distribution during PD process.

2 CONFIGURATION OF ANALYSIS

The configuration of analysis is an oblate spheroidal void enclosed in a solid dielectric near a planar electrode, as shown in Figure 1. The major and minor semi-axes of the void are denoted by b and c, respectively. The void is separated from the electrode by distance s. The configuration is subjected to uniform electric field $\mathbf{E}_0$ in the downward direction parallel with the minor axis of the void. $\mathbf{E}_0$ represents an electric field due to a potential difference applied between the planar electrode and the other electrode located so far from the void that its interaction with the spheroid is negligible. The dielectric constant of the void and that of the surrounding solid dielectric are denoted by ε_I (= 1) and ε_E, respectively. In the current analysis, we vary the axis ratio b/c of the void, the separation s, and the dielectric constant ε_E to observe the behavior of electric field. Typical values of dielectric constant $\varepsilon_E = 2$ and 4 are used for the solid dielectric. The condition of no space charge is assumed for the calculation.

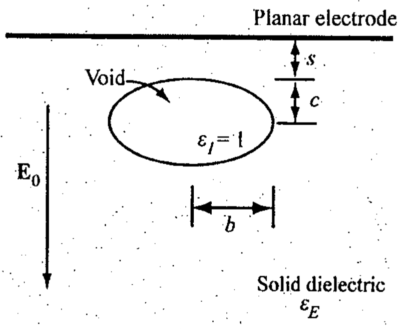

Figure 1. Configuration of analysis.

3 METHOD OF CALCULATION

3.1 OBLATE SPHEROIDAL COORDINATES AND HARMONICS

Figure 2 shows the oblate spheroidal coordinates (ζ, ξ, φ) used for the electric field analysis. They are related to the Cartesian coordinates (x, y, z) and the cylindrical coordinates (ρ, z, φ) by the following equations:

$$\begin{aligned} z &= a\zeta\xi \\ x &= \rho\cos\varphi \\ y &= \rho\sin\varphi \\ \rho &= a\sqrt{1+\zeta^2}\sqrt{1-\xi^2} \end{aligned} \tag{1}$$

where the coordinates $\zeta \geq 0$, $-1 \leq \xi \leq 1$, $0 \leq \varphi < 2\pi$, and a is a constant associated with the spheroidal coordinates. Any surface $\zeta = \zeta_0$ defines an oblate spheroid having $b = a\sqrt{1+\zeta^2}$, $c = a\zeta$, and foci at $\rho = a$ on the z = 0 plane. For $\zeta = 0$, the surface degenerates to a circular cylinder of radius a and zero thickness (i.e., a circular disc) on the z = 0 plane, as shown in figure 2. The scale factors h_1, h_2 and h_3 with respect to ζ, ξ and φ are as follows [21]:

$$\begin{aligned} h_1 &= a\sqrt{\frac{\zeta^2+\xi^2}{1+\zeta^2}} \\ h_2 &= a\sqrt{\frac{\zeta^2+\xi^2}{1-\xi^2}} \\ h_3 &= a\sqrt{(1+\zeta^2)(1-\xi^2)} \end{aligned} \tag{2}$$

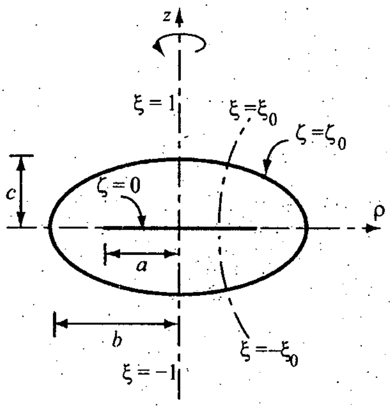

Figure 2. Oblate spheroidal coordinates.

For the analysis in this work, the potential is axisymmetric, independent of φ. We may express the potential ϕ in a general form as a sum of oblate spheroidal harmonics Φ and Ψ as

$$\phi(\zeta,\xi) = \Psi_B(\zeta,\xi) + \Phi_L(\zeta,\xi) \tag{3}$$

$$\Psi_B(\zeta,\xi) = \sum_{n=0}^{\infty} B_n Q_n(\mathrm{i}\zeta) P_n(\xi) \tag{4}$$

$$\Phi_L(\zeta,\xi) = \sum_{n=0}^{\infty} L_n P_n(\mathrm{i}\zeta) P_n(\xi) \tag{5}$$

In these equations, B_n and L_n are the potential coefficients, $\mathrm{i} = \sqrt{-1}$ is the imaginary unit, and P_n and Q_n are the nth-order Legendre functions of the first and second kinds, respectively. Note that the potential Ψ is singular at $\zeta = 0$ and vanishes as $\zeta \to \infty$. On the other hand, Φ is bounded at $\zeta = 0$ but singular at infinite ζ. The subscripts of the harmonic potentials denote the coefficients associated with them, for example, B and L of Ψ_B and Φ_L. Due to the property of $P_n(\mathrm{i}\zeta)$ and $Q_n(\mathrm{i}\zeta)$, the coefficients L_n and B_n must be imaginary numbers for odd and even orders n, respectively, for Φ and Ψ to be a real number.

3.2 POTENTIAL OF AN OBLATE SPHEROID

Consider an oblate spheroid defined by $\zeta = \zeta_0$. The spheroid is subjected to external potential ϕ^{ext} due to any sources located outside the spheroid. We can write ϕ^{ext} in the form of equation (5).

$$\phi^{ext} = \Phi_M(\zeta,\xi) = \sum_{n=0}^{\infty} M_n P_n(\mathrm{i}\zeta) P_n(\xi) \tag{6}$$

Because the potential ϕ^I inside the oblate spheroid ζ_0 is finite, we express the potential as

$$\phi^I = \Phi_L(\zeta,\xi) = \sum_{n=0}^{\infty} L_n P_n(\mathrm{i}\zeta) P_n(\xi) \quad \text{for } \zeta \leq \zeta_0 \tag{7}$$

The potential ϕ^E in the exterior of the spheroid is the sum of ϕ^{ext} and the potential due to charge induced on the spheroid surface, which vanishes as $\zeta \to \infty$. Therefore, we represent the induced potential with Ψ_B, and write for $\zeta \geq \zeta_0$,

$$\phi^E = \phi^{ext} + \Psi_B(\zeta,\xi) = \Phi_M(\zeta,\xi) + \sum_{n=0}^{\infty} B_n Q_n(\mathrm{i}\zeta) P_n(\xi) \tag{8}$$

The coefficients M_n, L_n and B_n must fulfill the boundary conditions of potential and electric field on the surface of the spheroid. That is, for $\zeta = \zeta_0$,

$$\phi^I = \phi^E \tag{9}$$

and

$$\varepsilon_E E_\zeta^E - \varepsilon_I E_\zeta^I = \frac{\sigma}{\varepsilon_0} \tag{10}$$

where σ is free-charge density at the interface, ε_0 is the permittivity of free space, and

$$E_\zeta = -\frac{1}{h_1}\frac{\partial}{\partial\zeta}\phi \tag{11}$$

In the absence of free charge at the boundary interface, from equations (7)–(11), we can deduce the coefficients L_n and B_n in the terms of M_n as follows:

$$L_0 = M_0 \tag{12}$$

$$B_0 = 0 \tag{13}$$

and for $n \geq 1$,

$$L_n = \frac{\left[\dfrac{Q_n'(\mathrm{i}\zeta_0)}{P_n'(\mathrm{i}\zeta_0)} - \dfrac{Q_n(\mathrm{i}\zeta_0)}{P_n(\mathrm{i}\zeta_0)}\right]}{\left[\dfrac{\varepsilon_I}{\varepsilon_E}\dfrac{Q_n'(\mathrm{i}\zeta_0)}{P_n'(\mathrm{i}\zeta_0)} - \dfrac{Q_n(\mathrm{i}\zeta_0)}{P_n(\mathrm{i}\zeta_0)}\right]} M_n \tag{14}$$

$$B_n = \frac{\left[\dfrac{\varepsilon_I}{\varepsilon_E} - 1\right]}{\left[\dfrac{\varepsilon_I}{\varepsilon_E}\dfrac{Q_n'(\mathrm{i}\zeta_0)}{P_n'(\mathrm{i}\zeta_0)} - \dfrac{Q_n(\mathrm{i}\zeta_0)}{P_n(\mathrm{i}\zeta_0)}\right]} M_n \tag{15}$$

In equations (14) and (15), P'_n and Q'_n are the derivatives with respect to ζ of $P_n(\mathrm{i}\zeta)$ and $Q_n(\mathrm{i}\zeta)$, respectively.

3.3 IMAGE CHARGE REPRESENTATION OF OBLATE SPHEROIDAL HARMONICS

For the condition of no space charge, the potential Ψ_B in equation (8) originates from charges on the surface of the spheroid. From each term of the harmonic potential

$\sum_{n=0}^{\infty} B_n Q_n(\mathrm{i}\zeta) P_n(\xi)$ in equation (4), we can deduce the image charges of an oblate spheroid. An oblate spheroidal harmonic of even order *n* corresponds to a single layer charge on the $\zeta = 0$ circular disc. The charge density $\rho_{s,n}$ can be deduced by using the Gauss' s theorem with the following limit:

$$\frac{\rho_{s,n}}{2\varepsilon_E} = -B_n P_n(\xi)\frac{1}{a|\xi|}\left[\lim_{\zeta\to 0}\frac{\mathrm{d}}{\mathrm{d}\zeta}Q_n(\mathrm{i}\zeta)\right] \tag{16}$$

The derivative of Q_n has a finite value at $\zeta = 0$,

$$\left[\frac{\mathrm{d}}{\mathrm{d}\zeta}Q_n(\mathrm{i}\zeta)\right]_{\zeta=0} = \mathrm{i}(-1)^{\frac{n}{2}}\frac{n!!}{(n+1)!!}(n+1) \tag{17}$$

From equations (16) and (17), we obtain the charge density as a function of ξ and *n* as

$$\frac{\rho_{s,n}}{2\varepsilon_E} = \mathrm{i}\,(-1)^{\frac{n}{2}+1}\frac{1}{a}\frac{n!!(n+1)}{(n+1)!!}\frac{P_n(\xi)}{|\xi|}B_n \tag{18}$$

for any even order *n*. Equation (18) indicates that the image charge density $\rho_{s,n}$ is infinitely large at the edge of the $\zeta = 0$ disc.

For an oblate spheroidal harmonic of odd order *n*, the corresponding image charge is a double layer charge or dipole on the $\zeta = 0$ disc. There is no singularity of the charge density for odd order *n*. We can deduce the dipole density $\rho_{d,n}$ from the discontinuity of potential values across the disc.

$$\frac{\rho_{d,n}}{2\varepsilon_E} = B_n P_n(\xi)\left[\lim_{\zeta\to 0}Q_n(\mathrm{i}\zeta)\right] \quad \text{for } \xi \ge 0 \tag{19}$$

The value of Q_n at $\zeta = 0$ is expressed by

$$Q_n(\mathrm{i}0) = (-1)^{\frac{n+1}{2}}\frac{(n-1)!!}{n!!} \tag{20}$$

Therefore, we obtain the dipole density

$$\frac{\rho_{d,n}}{2\varepsilon_E} = (-1)^{\frac{n+1}{2}}\frac{(n-1)!!}{n!!}P_n(\xi)B_n \quad \text{for } \xi \ge 0 \tag{21}$$

3.4 RE-EXPANSION OF THE OBLATE SPHEROIDAL HARMONICS

Consider an *n*th-order unit prolate spheroidal harmonic in coordinates (ζ', ξ', φ')

$$\Psi_{B,n}(\mathbf{r}') = Q_n(\mathrm{i}\zeta')P_n(\xi') \tag{22}$$

where $\mathbf{r}'$ is the vector from the origin *O'* to the point of calculation, as shown in Figure 3.

We want to re-expand $\Psi_{B,n}$ in the form of Φ_M about the origin *O* of coordinates (ζ, ξ, φ), which is at a distance z_0 below the center *O'* (see figure 3). That is,

$$\Psi_{B,n}(\mathbf{r}') = \Phi_M(\mathbf{r}) = \sum_{m=0}^{\infty} M_m^n P_m(\zeta)P_m(\xi) \tag{23}$$

where the vector **r** is from *O* to the point of calculation, and M_m^n are the coefficients of the re-expansion from $\Psi_{B,n}$ to $\Phi_{M,m}$. We can determine M_m^n by using the orthogonal property of the Legendre function,

$$\begin{aligned}\int_{-1}^{1} P_n(\xi)P_m(\xi)\,\mathrm{d}\xi &= \frac{2}{2m+1} && \text{if } n = m \\ &= 0 && \text{if } n \ne m \\ P_n(0) &= (-1)^{n/2}\frac{1}{n+1}\frac{(n+1)!!}{n!!} &&\end{aligned} \tag{24}$$

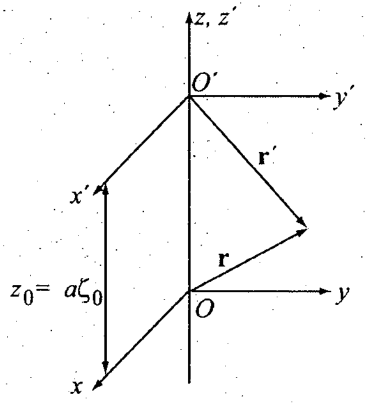

Figure 3. Re-expansion of prolate spheroidal harmonics.

For even order *m*, $P_m(\xi) = P_m(-\xi)$, i.e. the potential is the same on the upper and lower sides of the disc $\zeta = 0$. Therefore, for even *m*,

$$\begin{aligned}M_m^n &= (-1)^{m/2}(2m+1)\frac{m!!(m+1)}{(m+1)!!} \\ &\quad\times \int_0^1 \Psi_{B,n}(\mathbf{r}')P_m(\xi)\,\mathrm{d}\xi\end{aligned} \tag{25}$$

For odd order *m*, $P_m(\xi) = -P_m(-\xi)$. The integral in equation (25) becomes zero for odd *m*. Therefore, in order to determine M_m^n, we consider electric field in the ζ direction, which is again invariant across the disc $\zeta = 0$. From the identity of the Legendre function,

$$P_m'(\mathrm{i}0) = \frac{\mathrm{d}}{\mathrm{d}\zeta}P_m(\mathrm{i}\zeta)\bigg|_{\zeta=0} = \mathrm{i}(-1)^{\frac{m-1}{2}}\frac{m!!}{(m+1)!!}(m+1) \tag{26}$$

we can write the electric field E_ζ on the disc as

$$E_\zeta = \sum_{m=1}^{\infty}\mathrm{i}(-1)^{\frac{m+1}{2}}\frac{m!!}{(m+1)!!}(m+1)\frac{P_m(\xi)}{a|\xi|}M_m^n \tag{27}$$

Consider the upper half, where $E_\zeta = E_z$, we obtain

$$\begin{aligned}M_m^n &= \mathrm{i}(-1)^{\frac{m+1}{2}}(2m+1)\frac{(m-1)!!}{m!!} \\ &\quad\times a\int_0^1\left[-\frac{\mathrm{d}}{\mathrm{d}z}\Psi_{B,n}(\mathbf{r}')\right]\xi P_m(\xi)\,\mathrm{d}\xi\end{aligned} \tag{28}$$

for odd *m*.

Equations (25) and (28) can be numerically evaluated to determine the coefficient M_m^n from B_n.

3.5 CALCULATION PROCEDURE

For the configuration shown in figure 1, in addition to the boundary conditions (9) and (10) on the spheroid surface, the potential ϕ^E in the exterior of the spheroid must also satisfy the condition of a constant potential on the planar electrode. If we consider the single layer charge $\rho_{s,B}$ and double layer (dipole) charge $\rho_{d,B}$ representing the induced potential Ψ_B by the spheroidal void, the constant-potential condition can be fulfilled by placing the image charge in the opposite side of the electrode at the same separation d, as shown in figure 4. The image charge $\rho_{s,C}$ and dipole $\rho_{d,C}$ are of the same magnitude and at the same distance from the electrode. $\rho_{d,C}$ has the same polarity with $\rho_{d,B}$ but $\rho_{s,C}$ has the opposite polarity to $\rho_{s,B}$. We express the potential Ψ_C due to $\rho_{s,C}$ and $\rho_{d,C}$ as

$$\Psi_C = \sum_{n=0}^{\infty} C_n Q_n(\zeta') P_m(\xi') \tag{29}$$

where the coordinates ζ' and ξ' are taken with respect to the center of the image (charge or dipole) layer. It can be readily shown that

$$C_n = (-1)^{n+1} B_n \tag{30}$$

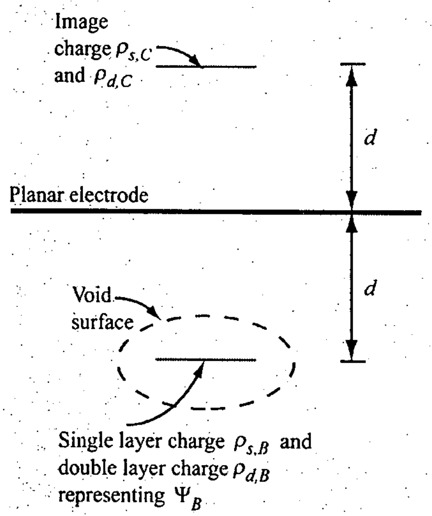

Figure 4. Image charge with respect to the planar electrode for satisfying the condition of a constant potential on the electrode.

The solution of the potential ϕ^E outside and ϕ^I inside the void for the configuration in figure 1 is determined using an iterative procedure similar to that used in [5] as follows:

1. The calculation begins with the potential Φ^{ext} of the externally applied field E_0. Taking the center of the spheroid as the origin, we note from equation (1) that $aP_1(i\zeta)P_1(\xi) = iz$. Therefore,

$$\Phi^{ext} = V_0 - iaE_0 P_1(i\zeta) P_1(\xi) \tag{31}$$

where V_0 is a constant depending on the potential of the planar electrode. We may notice that equation (31) is in the form of equation (6) with $M_0 = V_0$ and $M_1 = -iaE_0$.

2. We use equations (7), (8) and (12)–(15) to obtain the potential ϕ^E and ϕ^I that satisfy the boundary conditions on the spheroid surface.

$$\phi^E = \Phi^{ext} + \Psi_B^{(1)} \tag{32}$$

where the superscript '(1)' indicates the step of iteration.

3. As the condition of a constant potential on the conducting plane is not fulfilled by ϕ^E due to the added term $\Psi_B^{(1)}$, potential due to the image charge inside the conducting plane is applied to modify the potential. That is,

$$\phi^E = \Phi^{ext} + \Psi_B^{(1)} + \Psi_C^{(1)} \tag{33}$$

4. Using the re-expansion formulae in equations (25) and (28), we can re-expand $\Psi_C^{(1)}$ in term of Φ_M, and rewrite equation (27) as

$$\phi^E = \Phi^{ext} + \Psi_B^{(1)} + \Phi_M^{(1)} \tag{34}$$

5. The potential $\Psi_C^{(1)}$ or $\Phi_M^{(1)}$ in turn perturbs the boundary conditions on the spheroid surface. In order to fulfill the conditions again, we consider $\Phi_M^{(1)}$ as the external potential, and apply equations (7), (8) and (12)–(15) with respect to the potential. Thus,

$$\phi^E = \Phi^{ext} + \Psi_B^{(1)} + \Phi_M^{(1)} + \Psi_B^{(2)} \tag{35}$$

6. Perform Steps 3 to 5 to satisfy the boundary conditions on the conductor and those on the spheroid surface repetitively until the solution of ϕ^E converges. Then, the potential ϕ^I can be determined using equations (14) and (15).

4 CALCULATION RESULTS AND DISCUSSION

The method described in Section 3 is applied to the field analysis for the void shown in Figure 1. The highest order N of the harmonics is about 20, depending on the axis ratio of the void and the separation between the void and the electrode. The accuracy of the calculation results is evaluated from the boundary conditions of the normal components of the electric field on the void surface, as the harmonic potentials naturally satisfy the Laplace equation. In all cases of calculation, the ratio of the normal electric field differs from $\varepsilon_E/\varepsilon_I$ by less than 0.2%.

4.1 ISOLATED VOID

This section briefly explains the electric field behavior where the ratio s/c is so large that the influence of the electrode is negligible. It is well known that the electric field E_I in this case is uniform everywhere in the void [7, 21, 22].

For external uniform electric field $\mathbf{E}_0$ parallel to the major axis of the void,

$$\frac{E_I}{E_0}=\frac{\varepsilon_E/\varepsilon_I}{(\varepsilon_E/\varepsilon_I)-[(\varepsilon_E/\varepsilon_I)-1]\alpha} \tag{36}$$

The constant α in equation (35) is a function of the eccentricity,

$$\beta=\sqrt{1-(c/b)^2} \tag{37}$$

$$\alpha=\frac{1}{\beta^2}\left[1-\frac{\sqrt{1-\beta^2}}{\beta}\arcsin\beta\right] \tag{38}$$

The value of α varies from 1/3 for a sphere to unity for an infinitesimally thin spheroid or β = 1 (See Appendix B). Figure 5 shows the magnitude of the electric field normalized by E_0 inside the spheroidal void as a function of the dielectric-constant ratio $\varepsilon_E/\varepsilon_I$ for different values of the axis ratio b/c. It is clear from the figure that the electric field inside the void increases with the dielectric-constant ratio The field reaches its limiting value $(1-\alpha)^{-1}$ depending on the b/c ratio when $\varepsilon_E/\varepsilon_I$ is sufficiently large. For the same dielectric constant ratio, the field is higher in a void having larger axis ratio b/c, i.e. a flatter void. Theoretically, E_I/E_0 in equation (36) converges to $\varepsilon_E/\varepsilon_I$ as $b/c \to \infty$; however, from figure 5 we can see that the field is still considerably lower than this limit when b/c = 6.

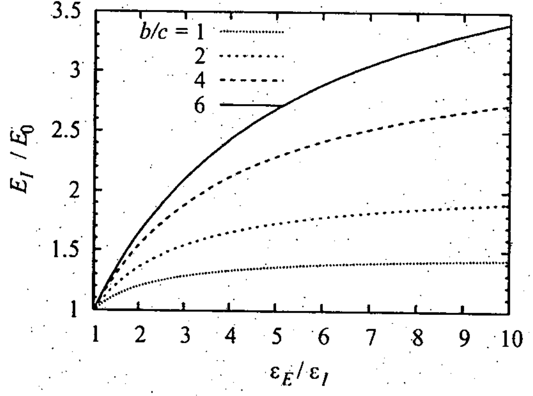

Figure 5. Electric field inside an isolated oblate spheroidal void under electric field $\mathbf{E}_0$.

4.2 FIELD VARIATION WITH SEPARATION

This section presents the effect of the electrode on the electric field inside the void. Figure 6 shows the electric field distribution also normalized by E_0 on the axis of symmetry, the minor axis, for the spheroidal voids of different axis ratio b/c values located in a solid dielectric having ε_E = 2. In each graph, the field is given for the normalized separation s/c ranging from zero to infinity. It is clear from the figure that the electric field on the axis is reduced when the void is located near an electrode. This behavior is similar to those reported in [6-8]. For small ratio b/c in Figure 6a, the field reduction with decreasing s/c is relatively prominent at the top pole (z/c = 1). However, for larger ratio b/c in Figures 6b and 6c, the electric field is reduced more uniformly along the axis when s/c becomes smaller. In all cases, the on-axis field converges well to its minimum when s/c is about 0.1. Similar plots of the electric field are shown in Figure 7 for ε_E = 4. We can see that the effect of the electrode is the same as that in Figure 6. In comparison with Figures 6, Figure 7 exhibits higher reduction of the electric field and stronger effect on the field at the top pole for the same ratio b/c.

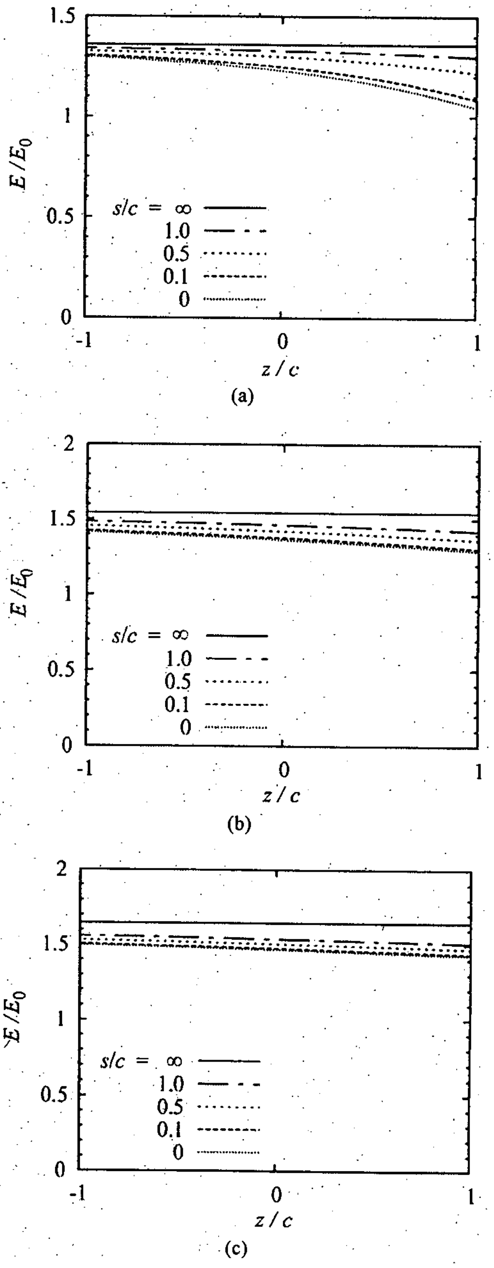

Figure 6. Electric field on the axis of symmetry of the spheroidal void inside a solid dielectric of ε_E = 2 for different separation s from the electrode: (a) b/c = 2, (b) b/c = 4 and (c) b/c = 6.

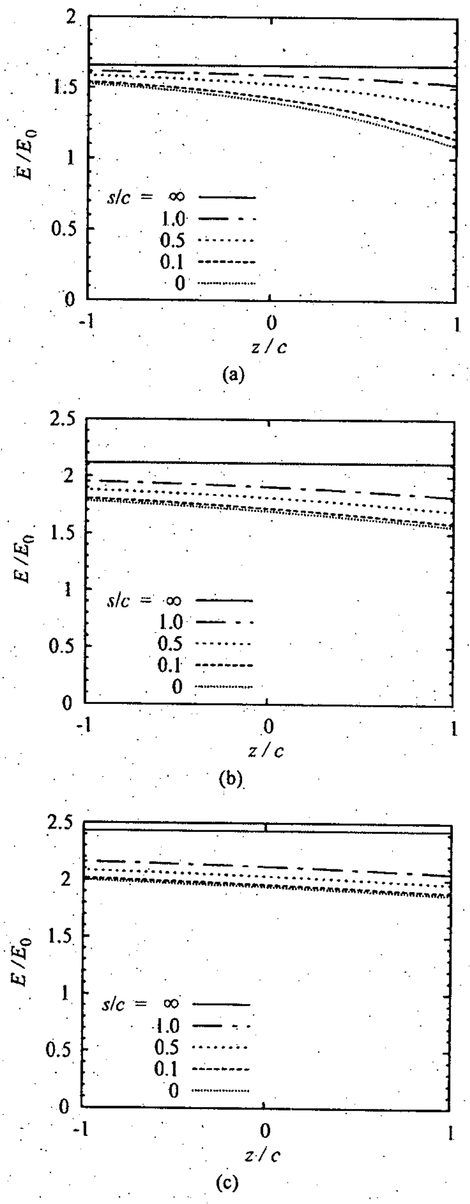

Figure 7. Electric field on the axis of symmetry of the spheroidal void inside a solid dielectric of $\varepsilon_E = 4$ for different separation s from the electrode: (a) $b/c = 2$, (b) $b/c = 4$ and (c) $b/c = 6$.

In Figure 8, the electric field E_I on the void surface is plotted for different separation s when $\varepsilon_E = 4$. The abscissa is the coordinate ξ of points on the surface, e.g. $\xi = 1$ and -1 at the top and bottom poles of the void, respectively. As can be seen from Figure 8, the effect of the electrode is negligible when the separation s is greater than the major semi-axis b of the void, i.e. $s/c > 2$, 4 and 6 in Figures 8a, b and c, respectively. For smaller separations, the electric field mitigation is more pronounced on the surface at the top-pole area. The voids with larger axis ratio b/c in Figures 8b and 8c also clearly exhibit field mitigation at the bottom pole. On the area between the poles, however, the degree of field reduction is smaller. The field maximum is located approximately at a small ξ value. This maximum decreases only slightly when the normalized separation s/c decreases from 1.0 to zero. The field distribution on the void surface for $\varepsilon_E = 2$ is similar to that in Figure 8, although it is not shown here. The difference between the field maximum when $s = \infty$ and that when $s = 0$ is reduced with decreasing ε_E for the same axis ratio c/b.

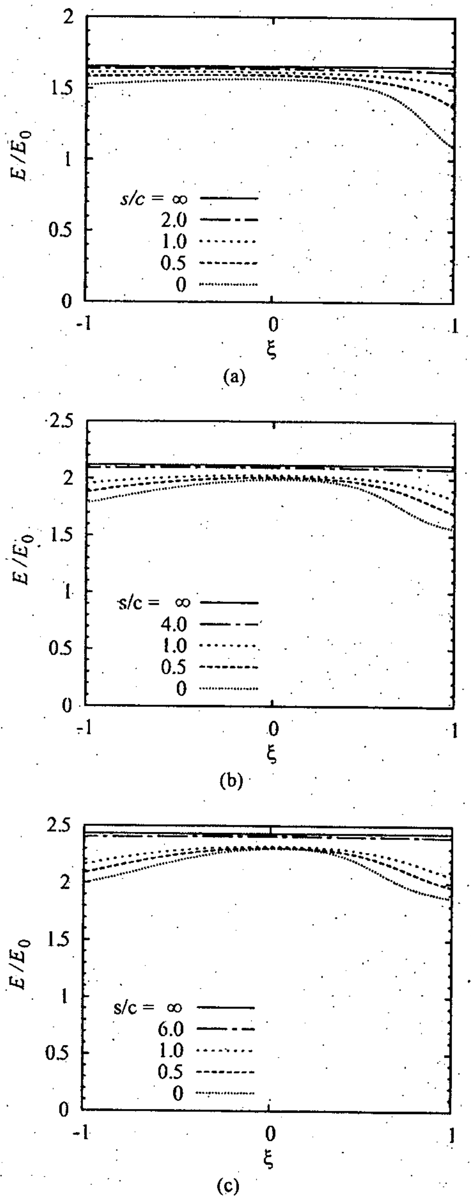

Figure 8. Electric field on the void surface for $\varepsilon_E = 4$ for different separation s: (a) $b/c = 2$, (b) $b/c = 4$ and (c) $b/c = 6$.

4.3 ELECTRIC FIELD IN THE LIMIT $s \to 0$

This section considers the extremity of field reduction, which takes place in the limit $s \to 0$, i.e. the void is in contact with the planar electrode. Figure 9 compares the electric field in such cases for different axis ratio b/c. The solid dielectric ε_E is 4 for the figure. The electric field in a spherical void ($b/c = 1$) is also included in the figures for comparison. It is clear that the field shown in Figure 9a follows the behavior explained in the previous section. For a spherical void or an oblate spheroidal void with small ratio b/c, the field reduction on the axis of symmetry is prominent near the top pole. With a larger axis ratio or a flatter shape, the field distribution is rather uniform on the axis, although the field minimum is still at the top pole. The minimum field stress increases with the axis ratio b/c.

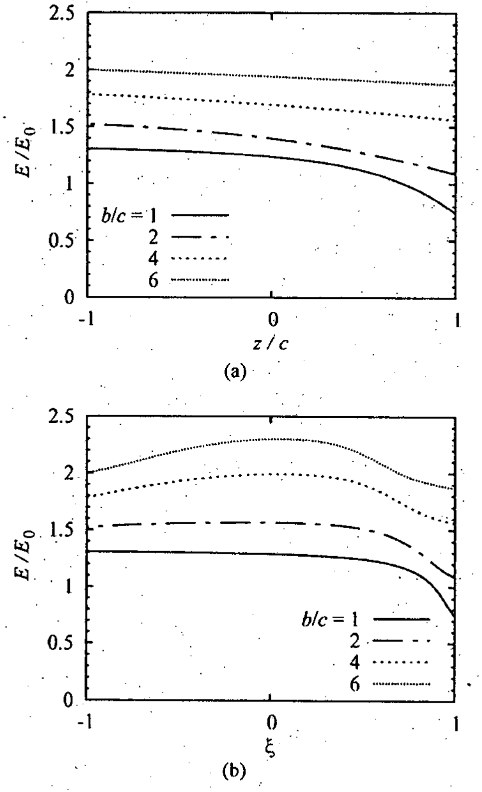

Figure 9. Electric field inside the void for different axis ratios c/b in the limit $s \rightarrow 0$ for $\varepsilon_E = 4$: (a) on the axis and (b) on the surface.

In Figure 9b, the electric field on the void surface is maximal at the bottom pole for $b/c = 1$, i.e. a spherical void. On the spherical void, electric field is rather uniform on a large portion of its surface. For an oblate spheroid with $b/c = 2$, the field distribution remains more or less uniform except at the top-pole area. With increasing ratio b/c to 4 and 6, the peak of the electric field and the shift of its position can be clearly observed in the figure.

Figure 10 displays the distribution of the potential and electric field inside spheroidal voids in the limit $s \rightarrow 0$ when the solid dielectric constant $\varepsilon_E = 4$. In the figure, the potential in relation with the electrode potential and the magnitude of the electric field are presented on the color scale given as the inset on each plot. The contours of equipotential and constant field magnitude are also plotted so as to clearly represent the distribution. From the equipotential lines in figure 10a for $b/c = 2$, it can be seen that the electric field direction is diverted from the minor axis of the void, which implies the reduction of the on-axis electric field. The corresponding electric field distribution of the void is shown in Figure 10b. It is clear from the figure that the region of the field maximum is located near the side surface of the void. Figure 10c shows the field variation inside the void having larger ratio b/c.

The aforementioned field behavior may be explained by considering the image of a void with respect to the plane electrode. The electric field near the axis of symmetry tends to divert from the axis due to the existence of the image void whose dielectric constant is smaller than that of the surrounding solid dielectric. However, the top pole is closest to its image and the distance from the image increases when moving away from the pole. Therefore, such shielding effect results in the field maximum near the side surface of the void.

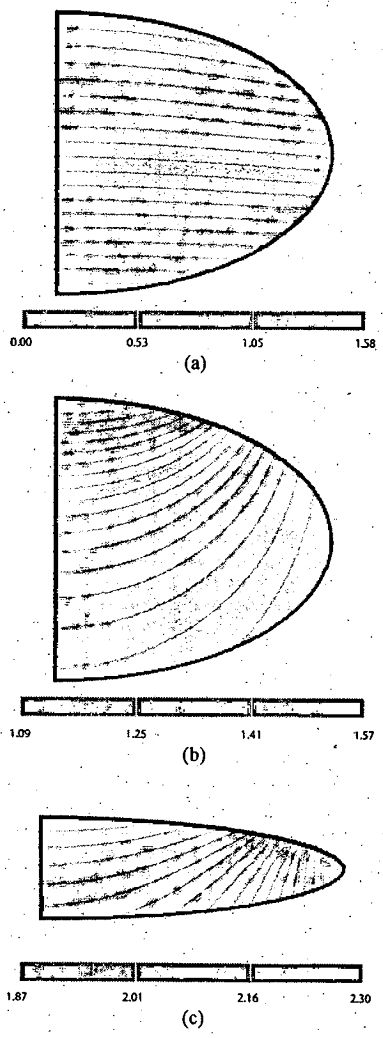

Figure 10. Potential and electric field inside the void of different ratios b/c in the limit $s \rightarrow 0$ for $\varepsilon_E = 4$: (a) potential for $b/c = 2$, (b) electric field for $b/c = 2$, and (c) electric field for $b/c = 6$.

It is worth noting here that the configuration of Figure 1 is identical in electric field to a configuration of two spheroidal voids aligned with vertical separation $2s$ in parallel with external field $\mathbf{E}_0$. Calculation results in the past showed the reduction of maximum field stress in the cylindrical voids when they were aligned parallel to an electric field [13-15].

However, the electric field distributions in Figures 7–10 exhibit that for a spherical void or a void with small ratio *b*/*c*, the field reduction is local at the region closer to the other void. The remaining portion of the void is still subjected to approximately the same field stress as for the isolated void. For a flatter void (larger ratio *b*/*c*), the electric field is reduced more uniformly along the axis of symmetry; however, higher electric field still exists at the side of the void volume.

Figure 11 presents the variation of the maximum electric field inside the oblate spheroidal voids in the limit $s \rightarrow 0$ with the dielectric constant ratio $\varepsilon_E/\varepsilon_I$. In comparison with the corresponding case of the isolated void (Figure 5), the reduction of the maximum field increases with $\varepsilon_E/\varepsilon_I$. For example, the maximum field is reduced by 1.3, 2.0 and 2.4% in the spherical void ($b/c = 1$) for $\varepsilon_E = 2$, 4 and 10, respectively. The field reduction is more prominent in the oblate spheroidal void, but the reduction is still only by 1.7, 5.3 and 10.3% with $b/c = 6$ for $\varepsilon_E = 2$, 4 and 10, respectively. Therefore, the discharge inception voltage should not be significantly reduced as expected from the on-axis electric field for the ε_E values treated here.

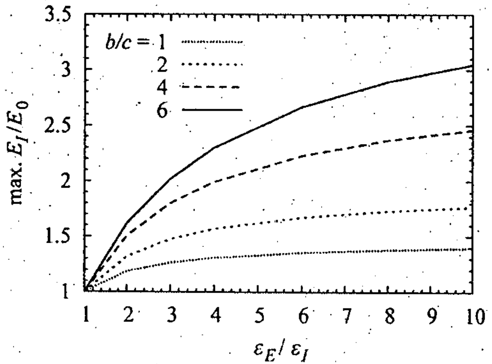

Figure 11. Maximum electric field inside the void as a function of the dielectric constant ratio in the limit $s \rightarrow 0$.

4.4 EQUIVALENT MULTIPOLE MOMENTS OF A VOID

The influence that the void exerts on the electric field in the exterior can be represented by using equivalent charges [23, 24]. Define axisymmetric potential Ψ_k^{sph} of the *k*th order multipole p_k in spherical coordinates (r, θ, φ) as

$$\Psi_k^{sph}(r,\theta) = \frac{p_k}{4\pi\varepsilon_E r^{k+1}} P_k(\cos\theta) \tag{39}$$

Note that factor $k!$ is excluded from this definition for simplicity. Conventionally, an equivalent dipole moment p_1 is utilized to represent the induced potential and the higher order terms are omitted. It is well known that for an isolated spherical void, p_1 is sufficient for the representation of the induced potential [23]. For an oblate spheroidal void, equivalent multipole moment p_k can be determined from the potential coefficient B_n by the corresponding image charge of density $\rho_{s,n}$ and image dipole of density $\rho_{d,n}$ corresponding to B_n.

For an even *n*th order harmonic,

$$p_k = 4\pi a^{k+1}(-1)^{k/2} 2^{n/2} \frac{\left(\frac{k}{2}\right)!}{\left(\frac{k-n}{2}\right)!} \frac{1}{(k+1)} \frac{(k+1)!!}{(k+n+1)!!} B_n \tag{40}$$

for $k = 0, 2, 4, \ldots$

For an odd *n*th order,

$$p_k = 4\pi a^{k+1}(-1)^{\frac{k+1}{2}} 2^{\frac{n-1}{2}} \frac{\left(\frac{k-1}{2}\right)!}{\left(\frac{k-n}{2}\right)!} \frac{k!!}{(k+n+1)!!} B_n \tag{41}$$

for $k = 1, 3, 5, \ldots$ More details on the determination of p_k are in Appendix A.

For an isolated oblate spheroidal void under external uniform field $\mathbf{E}_0$ parallel to its minor axis, the induced potential

$$\Psi_B = \Psi_{B,1} = B_1 Q_1(\mathrm{i}\zeta) P_1(\xi) \tag{42}$$

where B_1 is determined from $M_1 = aE_0$ by using equation (15). From equation (41),

$$p_k = 4\pi a^{k+1}(-1)^{\frac{k+1}{2}} \frac{1}{(k+2)} B_1 \quad \text{for odd } k \tag{43}$$

For even k, $p_k = 0$. Equation (43) indicates that even for an isolated spheroidal void under a uniform field, multipole moments must be incorporated to completely represent the induced potential, which is Ψ_{B1} in this case. As the magnitude p_k/p_1 decreases only gradually with the multipole order by the factor $(k + 2)^{-1}$ in equation (43), it is obvious that the multipole moments of higher orders cannot be ignored for the potential to be evaluated accurately near the void.

Figure 12 shows the equivalent multipole moments p_k, normalized by the p_1 in the corresponding cases of the isolated void, for different separation s values. Although the results in the preceding sections illustrate the change of the electric field distribution inside the void with separation s, the variation with s of the equivalent multipole moments is small in Figure 12. With decreasing s/c ratio, the multipole moments of odd orders slightly decrease. On the other hand, the moments of even order k become noticeable. The even orders arise from the influence of the image charges with respect to the electrode. The changes are observed more clearly at lower order multipoles. The comparison between Figures 11a ($b/c = 2$) and 11b ($b/c = 4$) indicates that the reduction of the equivalent multipoles at low odd orders are slightly enhanced with increasing the axis ratio. With higher ε_E value in Figure 12c, we can observe the change in p_k more clearly. Since for higher order k the multipole potential vanishes faster with the distance from the multipole, we may consider only the change in p_1 in order to approximate the influence of the electrode on the induced potential outside the void.

5 CONCLUSIONS

This work presents a method for calculating the electric field in configurations of an oblate spheroidal object. The method is applied to the study of electric field in a spheroidal void located in a solid dielectric below a planar electrode under an external uniform electric field. The results obtained from the study can be summarized as follows:

- Electric field in the void increases with the axis ratio *b*/*c* and with the dielectric constant of the surrounding solid dielectric.
- The influence of the electrode on the field is negligible if the separation *s* between the electrode and the void is larger than the major semi-axis of the void.
- With smaller separation, the electric field on the axis of symmetry of the void is reduced by the presence of the electrode near the void. The field distribution becomes rather uniform with increasing *b*/*c*.
- In a void having large ratio *b*/*c* (flatter void), the field maximum is not on the axis of symmetry but on the region near the side of the void.
- The reduction of the maximum field with decreasing *s* is not as significant as that of the on-axis electric field.
- Equivalent multipole moments of higher orders vary only slightly with decreasing the separation between the void and the electrode.

APPENDIX A

The equivalent multipole moments that give the same potential as $\Psi_{B,n}$ can be determined from the image charge described in Section 2. For a ring of charge on $z = 0$ plane, its equivalent multipole moments at the origin are based on the following relation [25]:

$$p_k = (-1)^{k/2} \frac{1}{(k+1)} \frac{(k+1)!!}{k!!} R^k Q_s \quad \text{for } k = 0, 1, 2, \dots \quad \text{(A1)}$$

where R is the radius of the ring charge and Q_s is the total charge of the ring. For a ring of dipole having radius R on the $z = 0$ plane,

$$p_{k+1} = (-1)^{k/2} \frac{1}{(k+1)} \frac{(k+1)!!}{k!!} (k+1) R^k Q_d \quad \text{(A2)}$$

for k = 0, 1, 2, ..., where Q_d is the total dipole moments of the ring.

Consider the image charge on the disc $\zeta = 0$ of an oblate spheroid. From equation (A1) and the distribution of charge in equation (18), we determine p_k from even order harmonic B_n by using an integral

$$p_k = \left[(-1)^{k/2} \frac{1}{(k+1)} \frac{(k+1)!!}{k!!} \int_0^a 2\pi\rho^{k+1} \frac{\rho_{s,n}(\xi)}{\varepsilon_E} \mathrm{d}\rho \right] B_n \quad \text{(A3)}$$

where $\xi = \sqrt{1-(\rho/a)^2}$. The integral (A3) yields

$$p_k = 4\pi a^{k+1} (-1)^{k/2} 2^{n/2} \frac{\left(\frac{k}{2}\right)!}{\left(\frac{k-n}{2}\right)!} \frac{1}{(k+1)} \frac{(k+1)!!}{(k+n+1)!!} B_n \quad \text{(A4)}$$

for k = 0, 2, 4, ... and $p_k = 0$ for odd k values.

From equation (A2) and the distribution of charge in equation (19), we can determine p_k from odd order harmonic B_n in a similar manner.

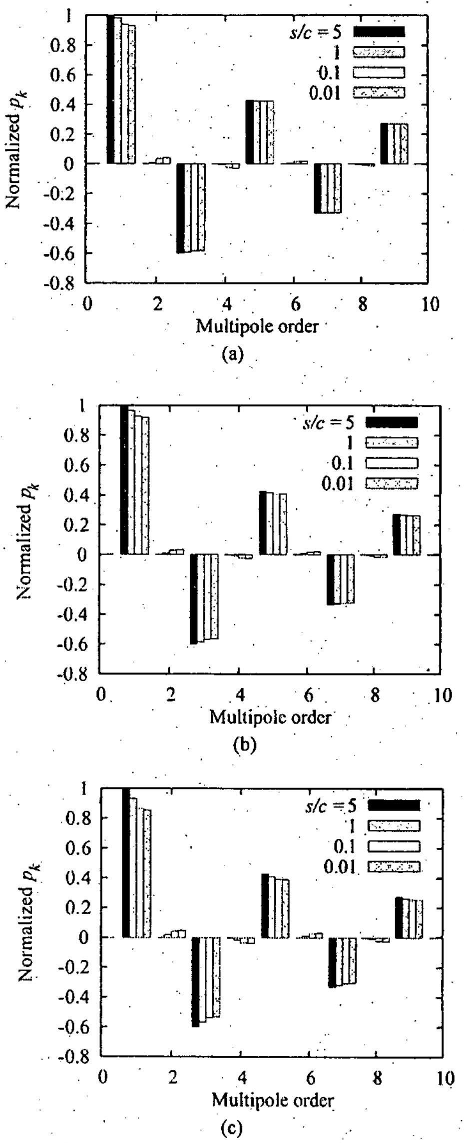

Figure 12. Variation of equivalent multipole moments with separation *s*: (a) *c*/*b* = 2 and $\varepsilon_E = 2$; (b) *c*/*b* = 4 and $\varepsilon_E = 2$; and (c) *c*/*b* = 4 and $\varepsilon_E = 4$.

APPENDIX B

From equation (38), it is clear that α approaches unity for an infinitely thin void ($\beta = 1$). On the other hand, for the limiting value of α when the void shape becomes a spherical one, we expand

$$\sqrt{1-\beta^2} = 1 - \frac{\beta^2}{2} - \frac{\beta^4}{8} - \frac{\beta^6}{16} - \dots \quad \text{(B1)}$$

$$\arcsin\beta = \beta + \frac{\beta^3}{6} + \frac{3\beta^5}{40} + \dots \quad \text{(B2)}$$

The limit of equation (38) is then written as

$$\lim_{\beta\to 0} \alpha = \lim_{\beta\to 0} \frac{1}{\beta^2} \left[1 - \left(1 - \frac{\beta^2}{2} - \dots\right)\left(1 + \frac{\beta^2}{6} + \dots\right) \right]$$

which yields

$$\lim_{\beta \to 0} \alpha = \frac{1}{3} \tag{B3}$$

Figure B1 shows the variation of the α value as β increases from 0 to 1.

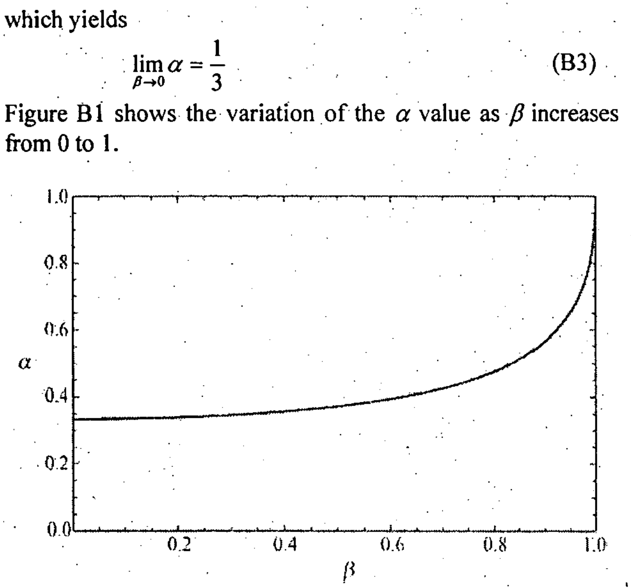

Figure B1. Variation of α value with β between 0 and 1.

ACKNOWLEDGMENT

Boonchai Techaumnat would like to thank Prof. Masao Washizu, University of Tokyo, for the discussion and comments on the spheroidal harmonics. This work was supported by the Thailand Research Fund (TRF).

REFERENCES

[1] B. Techaumnat and T. Takuma, "Field intensification at the contact point between a conducting plane and a spheroid or an elliptic cylinder", Int'l. Sympos. Electr. Insulating Materials (ISEIM), Vol. 3, pp. 808-811, 2005.

[2] T. B. Jones, R. D. Miller, K. S. Robinson and W. Y. Fowlkes, "Multipolar interactions of dielectric spheres", J. Electrostatics, Vol. 22, pp. 231-244, 1989.

[3] M. Washizu and T. B. Jones, "Dielectrophoretic interaction of two spherical particles calculated by equivalent multipole-moment method", IEEE Trans. Ind. Appl., Vol. 32, pp. 233-242, 1996.

[4] B. Techaumnat, B. Eua-arporn and T. Takuma, "Calculation of electric field and dielectrophoretic force on spherical particles in chain", J. Appl. Phys., Vol. 95, pp. 1586-1593, 2004.

[5] B. Techaumnat and T. Takuma, "Calculation of the electric field for lined-up spherical dielectric particles", IEEE Trans.Dielectr. Electr. Insul., Vol. 10, pp. 623-633, 2003.

[6] B. Techaumnat and M. Washizu, "Equivalent image charges of a prolate spheroid under an external electric field", J. Electrostatics, Vol. 69, pp. 388-393, 2011.

[7] T. Takuma and B. Techaumnat, *Electric Fields in Composite Dielectrics and their Applications*, Springer Netherlands, 2010.

[8] J. H. Mason, "The deterioration and breakdown of dielectrics resulting from internal discharges", Proc. IEE, Part I: General, Vol. 98, pp. 44-59, 1951.

[9] M. G. Danikas and G. Adamidis, "Partial discharges in epoxy resin voids and the interpretational possibilities and limitations of Pedersen's model", Electrical Engineering (Archiv fur Elektrotechnik), Vol. 80, pp. 105-110, 1997.

[10] B. Salvage, "Electric stresses in gaseous cavities in solid dieletrics", Proc. IEE, Vol. 111, pp. 1162-1172, 1964.

[11] B. Salvage, "Electric stresses at conducting surfaces located in the field between plane parallel electrodes", Proc. IEE, Vol. 111, pp. 1173-1176, 1964.

[12] G. Mitra and B. Salvage, "Electric stress in a circular cylindrical gaseous cavity in a solid dielectric, the axis of the cylinder being parallel to the field", Proc. IEE, Vol. 113, pp. 931-935, 1966.

[13] D. D. Chang, T. S. Sudarshan and J. E. Thompson, "Analysis of Electric Stress Distribution in Cavities embedded within Dielectric Structures", IEEE Trans. Electr. Insul., Vol. 21, pp. 213-219, 1986.

[14] M. E. Ghourab and S. M. El-Makkawy, "Analysis of electric field distribution in cavities within solid dielectric materials", IEEE Conf. Electr. Insul. Dielectr. Phenomena (CEIDP), pp. 155-160, 1994.

[15] A. A. Hossam-Eldin, S. S. Dessouky, S. M. El-Mekkawy and R. A. A. El-Aal, "Analysis and simulation of field distribution in micro cavities in solid insulating materials", IEEE Conf. Electr. Insul. Dielectr. Phenomena (CEIDP), pp. 792-796, 2007.

[16] G. C. Crichton, A. Karlsson and A. Pedersen, "A theoretical derivation of the transients related to partial discharges in ellipsoidal voids", IEEE Int'l. Sympos. Electr. Insul., pp. 238-241, 1988.

[17] G. C. Crichton, P. W. Karlsson and A. Pedersen, "Partial discharges in ellipsoidal and spheroidal voids", IEEE Trans. Electr. Insul., Vol. 24, pp. 335-342, 1989.

[18] I. W. McAllister and G. C. Crichton, "Influence of bulk dielectric polarization upon partial discharge transients: effect of void geometry and orientation", IEEE Trans. Dielectr. Electr. Insul., Vol. 12, pp. 240-247, 2005.

[19] I. W. McAllister, "Partial discharges in spheroidal voids - Void orientation", IEEE Trans.Dielectr. Electr. Insul., Vol. 4, pp. 456-461, Aug 1997.

[20] S. Boggs, "On-axis field approximations for a (semi-)spheroid in a uniform field", IEEE Trans. Dielectr. Electr. Insul., Vol. 10, pp. 305-306, 2003.

[21] W. R. Smythe, *Static and Dynamic Electricity*, 3rd ed., New York, USA, McGraw-Hill Book Company, 1968.

[22] T. Takuma, "Field behaviour at a triple junction in composite dielectric arrangements", IEEE Trans. Electr. Insul., Vol. 26, pp. 500-509, 1991.

[23] T. B. Jones, *Electromechanics of Particles*, Cambridge Univ Press, 2005.

[24] N. G. Green and T. B. Jones, "Numerical determination of the effective moments of non-spherical particles", J. Phys. D-Appl. Phys., Vol. 40, pp. 78-85, 2007.

[25] L. Grengard and V. Rokhlin, "The rapid evaluation of potential fields in three dimensions Vortex Methods", Vol. 1360, C. Anderson and C. Greengard, Eds., ed: Springer Berlin, Heidelberg, pp. 121-141, 1988.

Boonchai Techaumnat (M'02) was born in Bangkok, Thailand in 1970. He received the B.Eng. and M.Eng. degrees in 1990 and 1995, respectively from Chulalongkorn University, Thailand, and the doctoral degree in electrical engineering from Kyoto University in 2001. He joined the Faculty of Engineering, Chulalongkorn University as a lecturer in 1995. He is now an Associate Professor at the faculty. Dr. Techaumnat received the medal prize for new scholars from the Thailand Research Fund in 2005, the Nanobiotechnology Premium from the Institution of Engineering and Technology (IET) in 2009, and the book prize from the Institute of Electrical Engineers Japan in 2011 for "Electric Fields in Composite Dielectrics and their Applications". His research interests include numerical field analysis, electrical insulation, bioelectromagnetics, and particle electrokinetics.

Tadasu Takuma (S'84-M'91) was born in Mie prefecture, Japan, on 30 September 1938. He received the B.S., M.S., and Ph.D. degrees in electrical engineering from Tokyo University in 1961, 1963, and 1966, respectively. He worked for the Central Research Institute of Electric Power Industry (CRIEPI) from 1967 to 1995. He served as a Professor in the Department of Electrical Engineering, Kyoto University from 1995 to 2002 and as a Professor at the Tokyo Denki University from 2004 to 2009. He is now a part-time teacher at the Tokyo Denki University. His principal fields of interest are SF6 gas insulation, gas discharges, environmental problems of overhead transmission lines, numerical field calculation, and new energy problems. He is an author of "Electric Fields in Composite Dielectrics and their Applications" (Springer, 2010) and several Japanese books. Dr. Takuma received the Maxwell Premium from the Institution of Electrical Engineers, Great Britain in 1974, and three times the book prize from the IEE (the Institute of Electrical Engineers), Japan in 1981, 1991 and 2011, and Commendation from the Minister of State for Science and Technology, Japan in 1992.

Study on the Electromechanics of a Conducting Particle under Nonuniform Electric Field

Nisarut Phansiri and **Boonchai Techaumnat**
Department of Electrical Engineering, Chulalongkorn University
Phyathai Road, Pathumwan
Bangkok 10330, Thailand

ABSTRACT

This paper presents the study on the electromechanics of a conducting particle under nonuniform electric field between nonparallel electrodes. The purpose of the study is to investigate the feasibility of particle manipulation by the dielectrophoretic (DEP) force for insulation systems. A numerical simulation of the particle motion under electric field has been carried out to clarify the particle behavior without the application of particle manipulating technique. The results show that the charged particle moves to the region of lower electric field (wider gap), and the displacement increases with the tilt angle between the electrodes. The experimental measurement of the particle displacement agrees with the numerical results. For particle manipulation, the dielectric layers of silicone rubber and polyimide are placed on the grounded electrode. Numerical field calculation shows that with the dielectric layers, the DEP force attracts the particle to the region of higher field (smaller gap) and immobilizes it at the termination of the dielectric layers. Experiments are carried out to verify the theoretical prediction.

Index Terms — **Electric fields, electromechanical effects, force control, spheres, gas insulated switchgear, boundary element method.**

1 INTRODUCTION

GAS insulation is widely used for various high-voltage equipments in electric power transmission and distribution. For example, the gas insulated switchgears (GIS) and gas insulated lines (GIL) are the important components of power systems. The advantages of the gas insulation systems are high reliability and infrequent requirement of maintenance due to their closed structure. However, it is known that the existence of small particles in a gas insulation system can significantly reduce the insulating capability of the system [1]. Particles may appear in the insulation system in the process of manufacture, assembly or maintenance.

Up to now the dynamic behavior of conducting (metallic) particles under electric field has been studied in a number of works. A conducting particle acquires charge when it makes a contact with an electrode under electric field [2–4]. The interaction between the electric field and the induced charge results in the Coulomb force that tends to move the particle toward the other electrode [2]. Hence, depending on the electric field strength, the particle can be lifted from the electrode on which it is situated [5]. When the particle moves close to the other electrode, it may induce micro-discharge due to high electric field near it surface, resulting in the reduction of dielectric strength of the insulation system [6].

Under nonuniform electric field, particles also exhibit lateral movement along the electrode surface due to the electric gradient force [7, 8]. The theoretical and experimental studies on the horizontal movement of a spherical conducting particle on a coated electrode indicate that the particle can move to the region of higher field by the gradient force and then initiate discharge in the system for dc voltages [8] and ac voltages [9]. More complex behavior of particle has been reported in the presence of spacer [10]. In the work, it has been found that the particle may adhere to the spacer after its movement under electric field, depending on the spacer geometries. The adhesion of particle on the spacer affects considerably the surface flashover along the spacer [11, 12]. As the deactivation of particles becomes more important with the miniaturization of high-voltage equipments, particle controlling methods have been proposed based on the movement of charged particles under electric field (See references in [7] for details).

The present work follows the study of particle behavior in a configuration of nonparallel plate electrodes. Whereas the previous works stress on the charging mechanism in the case of dielectric-coated electrode [8], the current work mainly deals with the manipulation of small conducting particles (diameter less than 1 mm). We study the movement of a charged particle

---

Manuscript received on 26 July 2012, in final form 8 November 2012.

under nonuniform electric field in the atmospheric air. The experimental results are compared with the simulation results. With the purpose of particle deactivation, we apply a dielectric layer of appropriate thickness to restrain the particle from both direct charging by contact and indirect charging by micro-discharge in the background medium. The dielectrophoretic (DEP) force or the electrical gradient force functions to initiate the particle movement into the high-field region and trap the particle at the designated position. (In practical systems, appropriate conducting or dielectric profiles could be incorporated to create the field nonuniformity.) Although the DEP force is widely used for manipulation of particles in micrometer sizes, the application for insulation systems requires attention on the high electric field, which may bring about dielectric breakdown of the systems.

2 THEORETICAL BACKGROUND

Figure 1 shows the configuration of the conducting particle used in this work. In the configuration, a spherical conducting particle is located in the gap between nonparallel plate electrodes making a tilt angle θ_0. The lower electrode is grounded whereas potential $\phi = V_0$ is applied to the upper electrode. The surrounding medium is assumed to be air. A dielectric of thickness D may be inserted between the particle and the grounded electrode in order to prevent the particle from being charged. To indicate a position in the gap, we use the polar coordinates (ρ, θ) or Cartesian coordinates (x, z) as shown in figure 1 where

$$\begin{aligned} x &= \rho\cos\theta \\ z &= \rho\sin\theta \end{aligned} \qquad (1)$$

and the relationship between the unit vectors are

$$\begin{aligned} \mathbf{a}_\rho &= \cos\theta\,\mathbf{a}_x + \sin\theta\,\mathbf{a}_z \\ \mathbf{a}_\theta &= -\sin\theta\,\mathbf{a}_x + \cos\theta\,\mathbf{a}_z \end{aligned} \qquad (2)$$

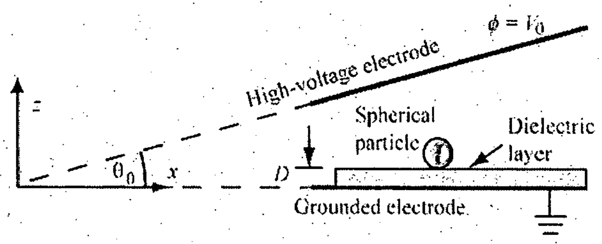

Figure 1. Configuration of a spherical conducting particle in nonparallel plate electrodes.

2.1 INDUCED CHARGE AND COULOMB FORCE

It is well known that a conducting particle in contact with an electrode under an electric field acquires charges from the electrode. For a conducting sphere of radius a under uniform electric field E, the analytical value of the charge q on the sphere is determined by [2, 3]

$$q = -\zeta(2)4\pi\varepsilon_0 a^2 E \qquad (3)$$

where $\zeta(2)$ is the Riemann's zeta function = $\pi^2/6$, and positive E is taken in the direction into the electrode. In the absence of the dielectric layer, the applied electric field $E = V_0(\rho\theta_0)^{-1}$ in the configuration of Figure 1. We can approximate the charge induced on the sphere whose center is at (x_p, a) as

$$q_p \approx -\frac{2}{3}\pi^3 a^2 \varepsilon_0 \frac{V_0}{\rho_p \theta_0} \qquad (4)$$

where $\rho_p = \sqrt{x_p^2 + a^2}$. While the particle stays on the electrode, it is subject to the Coulomb force $\mathbf{F}_q$ that tends to detach the particle from the electrode. The force is expressed by

$$\mathbf{F}_q = 0.832 q_p E \mathbf{a}_z \qquad (5)$$

When the particle is well separated from any electrode, the Coulomb force can be simply estimated by

$$\mathbf{F}_q = q_p \mathbf{E} \qquad (6)$$

2.2 DIELECTROPHORETIC FORCE

The dielectrophoretic (DEP) force $\mathbf{F}_{DEP}$ or the electrical gradient force acts on a particle having different polarization from the surrounding medium under nonuniform electric field. The DEP force can be estimated based on the effective dipole moment $\mathbf{p}_{eff}$ of the particle. For a conducting sphere,

$$\mathbf{p}_{eff} = 4\pi\varepsilon_0 a^3 \mathbf{E} \qquad (7)$$

The DEP force acting on this dipole is expressed as [13]

$$\mathbf{F}_{DEP} = (\mathbf{p}_{eff} \cdot \nabla)\mathbf{E} = 2\pi\varepsilon_0 a^3 \nabla E^2 \qquad (8)$$

For the nonparallel electrode configuration in figure 1, the analytical expression of $\mathbf{F}_{DEP}$ in the special case that $D = 0$ is

$$\mathbf{F}_{DEP} = -4\pi\varepsilon_0 a^3 \frac{V^2}{\rho^3\theta_0^2}\mathbf{a}_\rho \qquad (9)$$

The DEP force attracts the conducting particle to the region of higher electric field (so-called "positive dielectrophoresis"). Note that equation (9) neglects the higher-order multipolar forces [14]. More details on the DEP force are referred to references [13, 15].

The other forces acting on the spherical particle are the gravitational force $\mathbf{F}_g$, the friction force $\mathbf{F}_\mu$ and the viscous force $\mathbf{F}_\nu$. The viscous force for a sphere having velocity $\mathbf{v}$ is

$$\mathbf{F}_\nu = -6\pi\eta a v \qquad (10)$$

where the coefficient of viscosity η is about 18.2 μPa-s for the air. The total force $\mathbf{F}_{tot}$ on the particle is

$$\mathbf{F}_{tot} = \mathbf{F}_q + \mathbf{F}_{DEP} + \mathbf{F}_g + \mathbf{F}_\mu + \mathbf{F}_\nu \qquad (11)$$

Note that $\mathbf{F}_\mu$ in equation (11) is applicable when the sphere is on the lower substrate.

2.3 MOTION ONSET CONDITION

The motion onset voltages of the particle have already been analyzed for the levitation (lifting) and for the lateral movement when the particle is on a grounded electrode without a dielectric layer [6] or on a grounded electrode coated with a thin dielectric [8]. In brief, when the particle radius a is much smaller than coordinate x_p, the onset voltages can be estimated as follows:

The levitation-onset voltage V_L and electric field E_L of the particle centered at Cartesian coordinates (x_p, a) on the grounded electrode without the dielectric layer are determined by equating the gravitational force with the Coulomb force.

$$E_L = \frac{V_L}{\rho_p\theta_0} \approx 0.5\sqrt{\frac{a\rho_m g}{\varepsilon_0}} \tag{12}$$

where ρ_m is the mass density and g is the gravitational acceleration.

The condition for the lateral motion of the particle must be considered separately for (a) the case without a dielectric layer and (b) the case with a dielectric layer on the grounded electrode. Consider a particle that is directly on the grounded electrode, for which the static friction coefficient is μ. The onset voltage V_H and electric field E_H for the lateral motion are determined from the condition

$$F_{DEP} = \mu\left(F_g - F_q\right) \tag{13}$$

which yields

$$E_H = \frac{V_H}{\rho_p\theta_0} \approx \sqrt{\frac{\mu a\rho_m g}{\varepsilon_0\left[4\mu + (3a/\rho_p)\right]}} \tag{14}$$

Note that for the conducting particle resting on the grounded electrode, V_H is always smaller than V_L because when the Coulomb force F_q is comparable with the gravitational force, the friction is considerably reduced and the particle is ready for the lateral motion. In practice, however, other adhesive forces may inhibit the lateral movement of the particle before levitation.

If a very thin dielectric layer exists between the particle and the grounded electrode, and we assume the particle is uncharged, the Coulomb force is omitted from equation (13). As a result, the condition of the lateral motion onset becomes

$$E_H = \sqrt{\frac{\mu\rho_m g\rho_p}{3\varepsilon_0}} \tag{15}$$

which is higher than that by equation (14). However, it is worth noting that this condition may not hold due to two factors. First, with a thin dielectric layer, the electric field is highly intensified near the contact point [16]. Thus, the particle is possibly charged to a certain degree. Although the charge amount may not be as large as that in equation (4), the particle charging reduces the motion-onset voltage. The other factor is that even when the net charge is zero on the particle, there is still the interaction between the induced charges on the particle and the grounded electrode, which is also neglected in equation (15). The force on the induced charge results in the enhancement of the adhesion between the particle and the electrode.

3 EXPERIMENTAL SETUP

Aluminum and stainless steel spheres of 0.4 mm radius (Micro Surface Engineering) were mainly used as the particles in the experiments. The particles were cleaned by sonication and kept at 80–120 °C prior to each experiment.

Figure 2a shows the schematic diagram of the experimental setup for the observation of particle motion. The lower electrode was set on a 3-axis linear positioning stage, and the upper electrode was attached to a goniometer stage for the angle adjustment. The electrodes of diameter 27 mm were made from stainless steel and had appropriate contours in order to prevent excessively high electric field at their edges (Figure 2b). The tilt angle $\theta_0 = 3°$ was used for investigating the basic behavior of particle, and $\theta_0 = 15°$ was used for the experiments on particle manipulation. For the experiments, we placed a dielectric sheet about 1.0 mm in thickness on the grounded electrode. Poly-dimethylsiloxane or PDMS (KE-106, Shin-Etsu), a silicone rubber, was selected as the material due to fabrication convenience. A polyimide film of 74 μm thickness (Kapton, Dupont) was attached to the top surface of the PDMS to reduce the friction force. The dielectric constants of the PDMS and the polyimide are equal to 3.1 and 4, respectively.

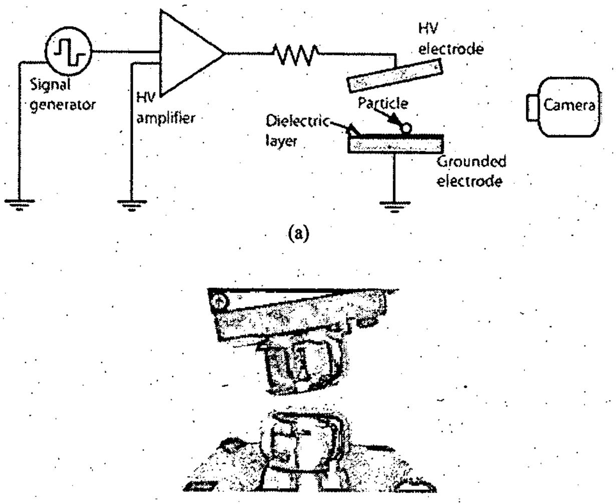

(a)

(b)

Figure 2. Experiment setup: (a) schematic Diagram; (b) electrodes.

The lower electrode was grounded, and the high voltage V_0 was applied to the upper electrode. The voltage was generated by a high-voltage amplifier (Model 610E, Trek) receiving the input from a signal generator (Model AFG3021, Tektronix). The electromechanical basics of the particle on the grounded electrode was observed by applying a dc voltage for 500 ms. For the DEP trapping experiments, we applied continuous 50-Hz ac voltage of the sinusoidal waveform.

The motion of the particle was observed through a 1/3-inch charge-coupled device (CCD) camera (Model 902H3 Ultimate, Watec) with a telecenteric lens. The camera was connected to a PC for recording images at 30 fps rate.

4 RESULTS AND DISCUSSION

4.1 PARTICLE ON THE GROUNDED ELECTRODE WITHOUT DIELECTRIC LAYERS

A preliminary experiment was carried out to measure the levitation-onset voltage for gaps of 2 and 4 mm without the dielectric layers. The difference between the measured values and the estimation by using equation (12) was about 10% for the aluminum particles and 3% for the stainless steel particles used in this work. To observe the electromechanical basics of the particle under the electrode system, the study began with the case in which the particle was on the grounded electrode in the absence of the dielectric layer. We carried out a numerical simulation of the particle trajectory for θ_0 = 3°, 6° and 9° when the applied voltage V_0 was higher than the levitation-onset voltage V_L. The particle velocity $\mathbf{v}_1$ before and $\mathbf{v}_2$ after the impact with the electrodes are related by

$$\mathbf{v}_{2,n} = -k_n \mathbf{v}_{1,n} \tag{16}$$

and

$$\mathbf{v}_{2,t} = k_t \mathbf{v}_{1,t} \tag{17}$$

where k_n and k_t are the coefficients of impact, and the subscripts '*n*' and '*t*' denote the normal and tangential directions of the velocities. We used k_n and k_t equal to 0.6 and 0.7, respectively, obtained from an experiment of the aluminum particle on the electrode.

To validate the numerical results, an experiment was done to measure the displacement of the aluminum particle. In the experiment, a PDMS film of thickness 30 µm was placed on the grounded electrode near the initial position of the particle. After the voltage application of a DC voltage, the particle repeatedly moved up and down across the air gap. The position of the PDMS sheet was chosen so that the particle fell on the sheet after two round trips. Because the sheet inhibited the particle from exchanging charges with the grounded electrode, the particle adhered to the PDMS layer after the impact, as schematically shown in Figure 3. The displacement Δx of the particle from the initial position was then measured and compared with the simulation results. For x_p = 106 mm, θ_0 = 3° and V_0 = 4 kV, the average value of the measured Δx was 0.75 mm whereas the numerical simulation yielded Δx = 0.83 mm, about 10.7% different from the measured value.

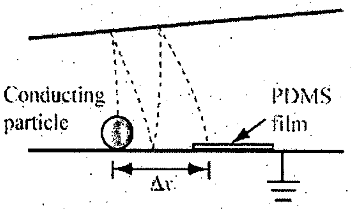

Figure 3. Schematic diagram for the measurement of particle displacement.

The calculated trajectory of the aluminum particle for a longer time (270 ms) is shown in Figure 4. It is clear from the figure that when the levitation takes place the particles move to the right hand side (lower-field region). When the particle is lifted from the electrode, the Coulomb force is predominant over the DEP force. The particle makes an impact with a electrode in a direction slightly deviated from the normal direction due to its velocity, and departs from the electrode with a larger angle of deviation because $k_t > k_n$.

Figure 5 shows the numerical results of the horizontal displacement Δx of the aluminum particle as a function of time for the same V_0 but different values of the tilt angle θ_0. The particle is subject to the same electric field strength at the initial position, i.e. constant $\rho\theta_0$ at the time t = 0. The figure illustrates that with increasing the tilt angle of the upper electrode, the particle moves faster to the right hand side. It is worth noting that when the applied voltage V_0 is larger than V_H but smaller than V_L, the particle is initially moved along the lower electrode by the DEP force to the higher-field region (left hand side), and then levitates from the electrode when the Coulomb force is strong enough [6]. The subsequent trajectory should follow the tendency shown in figures 4, i.e. toward the lower-field region.

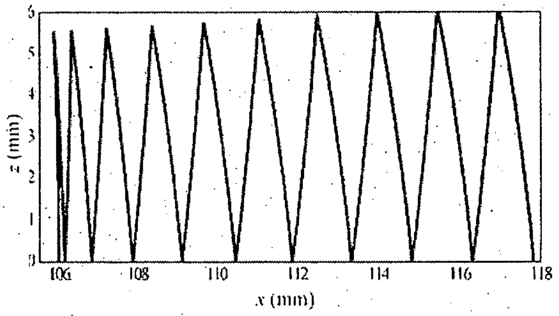

Figure 4. Calculated trajectory of the aluminum particle at initial x_p = 106 mm for V_0 = 4 kV and tilt angle θ_0 = 3°.

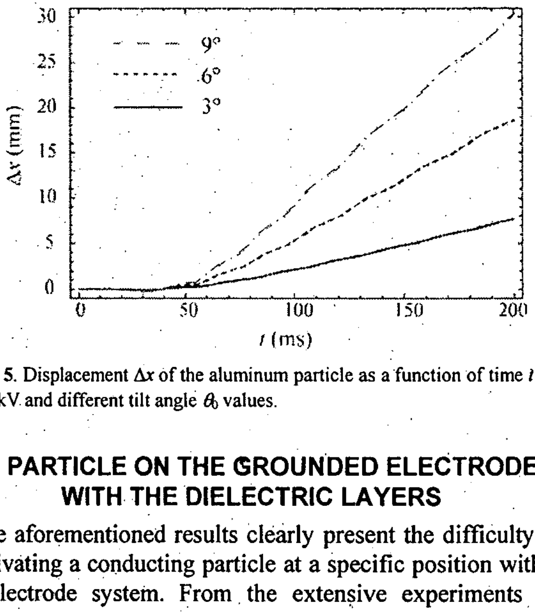

Figure 5. Displacement Δx of the aluminum particle as a function of time t for V_0 = 4 kV and different tilt angle θ_0 values.

4.2 PARTICLE ON THE GROUNDED ELECTRODE WITH THE DIELECTRIC LAYERS

The aforementioned results clearly present the difficulty in deactivating a conducting particle at a specific position within the electrode system. From the extensive experiments on diverging plate electrodes with a spacer by Hara's group, it has been found that in addition to the oscillation across the electrode gap, when a particle is charged, it may adhere to a spacer surface and move along the surface under high electric field [10]. In this section, we deal with a simple configuration to manipulate the conducting particle by using the DEP force. In this configuration, the nonuniform electric field at the termination of the dielectric layer is employed to trap the particle. Note that although we can design the electrode profiles or utilize a small gap to achieve high field gradient for the particle trap, such the configuration is more vulnerable to partial discharge.

As already mentioned, the PDMS sheet was placed on the grounded electrode to prevent the particle from being charged by direct contact with the electrode. We chose the thickness D of the sheet greater than the particle radius a in order to avoid excessively high electric field at the contact point between the particle and the dielectric, which would also increase the charging possibility. Another role of the thickness D was to reduce the normal (adhesive) force between the induced charge on the particle and the grounded electrode.

4.2.1 NUMERICAL RESULTS

To investigate the influence of the dielectric sheet on the electric field strength in the gap, we calculate the electric field in the air gap with the presence of the dielectric layers numerically by using the 2D boundary element method [17]. As the polyimide film is very thin, only the PDMS sheet is considered in the calculation. Figures 6a and 6b present the calculation results of the electric field distribution in the air gap between the dielectric surface and the upper electrode for $V_0 = 1$ kV, $\theta_0 = 15°$, $x = 11$–24 mm, corresponding to upper electrode height $z_u = 3.0$–6.4 mm. Two D values, 0.6 and 1.0 mm, are used to observe the effect of the thickness, respectively. The contours of constant field strength are also drawn in the figures to make clear the variation of the electric field. From Figure 6, we can see the increase of the electric field strength from right to left due to the shorter gap length. The influence of the dielectric layers becomes more prominent with decreasing the gap length, as we can see the lines of constant field deviate from the constant-r relationship. The electric field is intensified to the maximum value at the termination of the dielectric on the left. Another local peak of the electric field is located on the upper electrode, which terminates near the upper left corner of the figure.

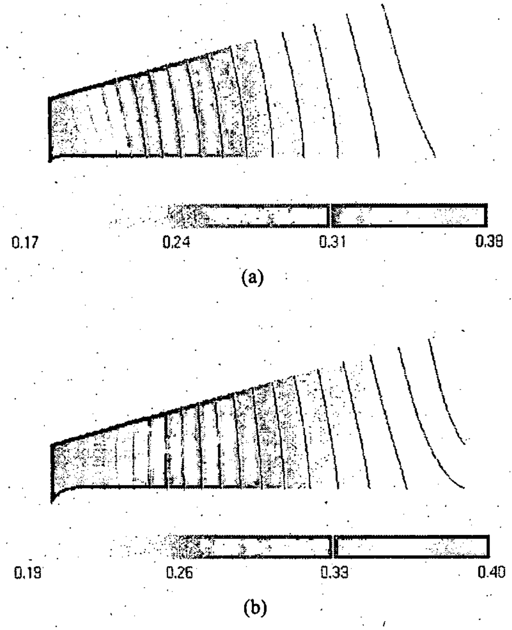

Figure 6. Calculation results of the electric field distribution in the air gap between the dielectric surface and the upper electrode for $V_0 = 1$ kV, $\theta_0 = 15°$ and (a) $D = 0.6$ mm; (b) $D = 1.0$ mm.

Figure 7 shows the electric field strength at height 0.4 mm (particle radius) above the dielectric surface. It can be seen from the figure that for the same x value, the field strength is slightly higher on the thicker dielectric layer. The maximum field strength is about 0.38 kV/mm for $D = 0.6$ mm and 0.40 kV/mm for $D = 1.0$ mm.

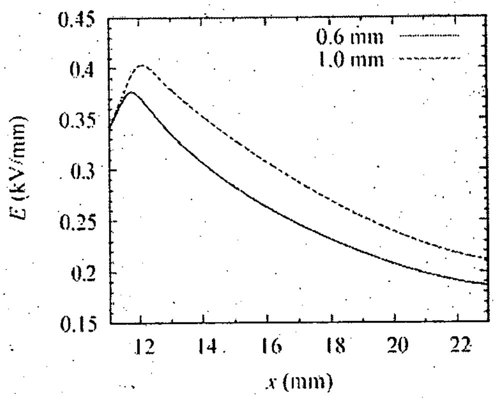

Figure 7. Electric field strength at 0.4 mm above the dielectric surface for $V_0 = 1$ kV, $\theta_0 = 15°$ and $D = 0.6$ or 1.0 mm.

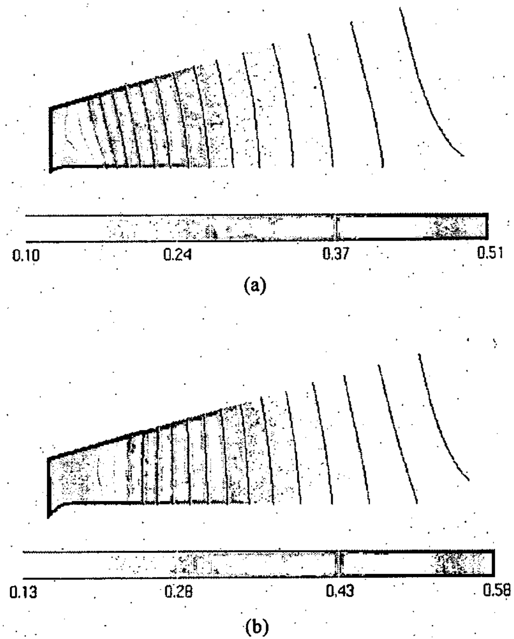

Figure 8. Distribution of $|W_E|$ for the uncharged conducting particle in the air gap for $a = 0.4$ mm, $V_0 = 1$ kV, $\theta_0 = 15°$ and (a) $D = 0.6$ mm; (b) $D = 1.0$ mm.

The electric field energy W_E for an uncharged conducting particle residing in the air gap is determined as [18]

$$W_E = -2\pi\varepsilon_0 a^3 E^2 \tag{16}$$

Figure 8 shows the profiles of $|W_E|$ in the air gap. Again, the variations similar to those in Figure 6 can be observed from Figure 8 for which higher energy magnitude is in the case $D = 1.0$ mm. Equations (8) and (16) imply that the DEP force can be determined from the energy gradient. Therefore, we may deduce the force direction from the contours of constant W_E in Figure 8. When a conducting particle is on the dielectric sheet, the DEP force attracts the particle to the field maximum at the termination of the dielectric sheet.

Figure 9a shows the magnitude of the DEP force estimated by equation (8) for dielectric thickness $D = 1.0$ mm. Note that the maximum force magnitude in the figure is limited to 100 nN for the color scale in order that we can clearly observe the force variation in the whole gap. The actual force is significantly stronger than 100 nN near the termination of the dielectric sheet. The force increases from a few nN on the right hand side of the figure along the dielectric surface to over 100 nN on the left hand side. Figure 9b displays the DEP force direction in the region near the dielectric termination. Due to large difference in force magnitudes in the region, all the force vectors are normalized to the same length. The figure illustrates that a conducting particle is attracted by the DEP force to the termination of the dielectric sheet, provided that it is not levitated so high from the dielectric surface.

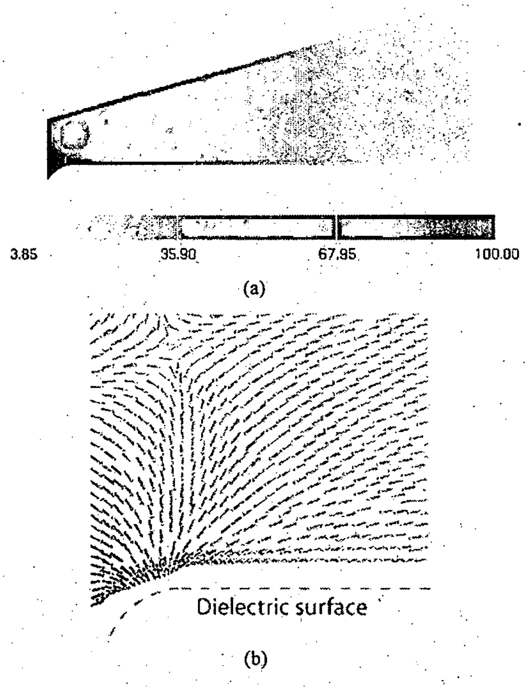

Figure 9. DEP force for $V_0 = 1$ kV, $\theta_0 = 15°$ and $D = 1.0$ mm: (a) Magnitude of the force on color scale; (b) Direction of the force near the termination.

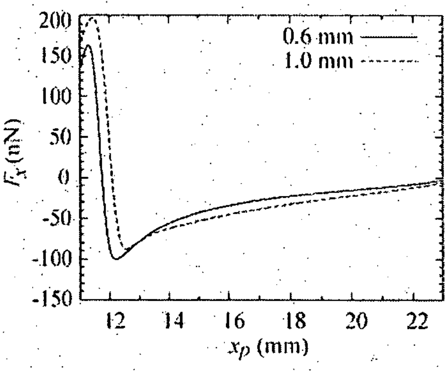

Figure 10. DEP force acting on the particle when it is on the surface of the dielectric sheet for $V_0 = 1$ kV, $\theta_0 = 15°$ for $D = 0.6$ or 1.0 mm.

In Figure 10, the horizontal component F_x of the DEP force is plotted for the conducting spherical particle located on the dielectric sheet, i.e. at $z_p = 1.0$ and 1.4 mm for $D = 0.6$ and 1.0 mm, respectively. It can be seen from the figure that when the particle is far from the termination of the dielectric sheet, it is subject to the force in the $-x$ direction. This force magnitude increases with decreasing x_p and is stronger for $D = 1.0$ mm than for $D = 0.6$ mm. The maximum positive F_x, which prevents a moving particle from breaking the DEP trap, is very high at the dielectric termination. The configuration with $D = 0.6$ mm yields slightly larger magnitude of the negative force, possibly because of the smaller curvature applied to the dielectric termination in the geometrical model.

From a preliminary measurement on the polyimide surface, the static friction ranges from 380 to 730 nN for the aluminum particle and from 368 to 1270 nN for the stainless steel particle. The DEP force varies proportionally with V_0^2 in equation (9). Based on the numerical field calculation results and the higher values of the measured friction force, the motion-onset voltage of the particle for $D = 1.0$ mm is estimated to be 5.0 kV for the aluminum particle and 6.6 kV for the stainless steel particle at $x_p = 18.66$ mm, corresponding to $z_u = 5$ mm. With these V_0 values, the maximum background electric fields (in the absence of the particle) at the dielectric termination are about 2.03 and 2.7 kV/mm for the particles, which are still below the critical field stress of the air for the experiment conditions. However, it is to be noted that the actual maximum field depends heavily on the geometrical profiles of the dielectric. In addition, the presence of the particle also intensifies the electric field in its proximity. Thus, the particle is possibly charged to a certain degree. However, if the amount of charge is sufficiently limited so that the levitation does not take place, the particle is still attracted to the dielectric surface by the DEP force, as shown in Figure 9.

4.2.2 EXPERIMENTAL RESULTS

To verify the numerical prediction, we performed experiments for the tilt angle $\theta_0 = 15°$ of the upper electrode. The thickness $D = 1.0$ mm was chosen for the PDMS as the numerical results showed that the thicker dielectric sheet enhanced the DEP force. We employed two kinds of the dielectric termination. For the first kind of termination, the PDMS sheet and the polyimide film were terminated at the same position. For the second kind, the polyimide film was extended longer than the edge of the PDMS sheet about 1–2 mm.

Figure 11 shows the recorded images of the particle motion on the dielectric layers when the first kind of dielectric termination is used. The particle was initially at $x_p \approx 16.4$ mm, corresponding to upper electrode height $z_u = 4.4$ mm (Figure 11a). After increasing the applied voltage V_0 to 3.5 kV, the particle began to move along the dielectric surface to the left hand side (Figure 11b). When the particle reached the termination of the dielectric layers, it was trapped at the edge of the PDMS layer, as shown in Figure 11c. The particle remained stabilized at this position under the continuous voltage application. From a series of experiments on this configuration, we found that the particle might be trapped at the termination of the dielectric layers or move through the smallest gap without deceleration. The probabilities of the fail and successful immobilization were approximately the same. The particle charge could be a critical factor for the particle behavior at the dielectric termination. Although the use of dielectric layers and appropriate gap length successfully suppressed the particle levitation, the particle was still charged to a certain degree. At the dielectric termination, the particle was closer to the electrode and the Coulomb force possibly negated the DEP force used for immobilization.

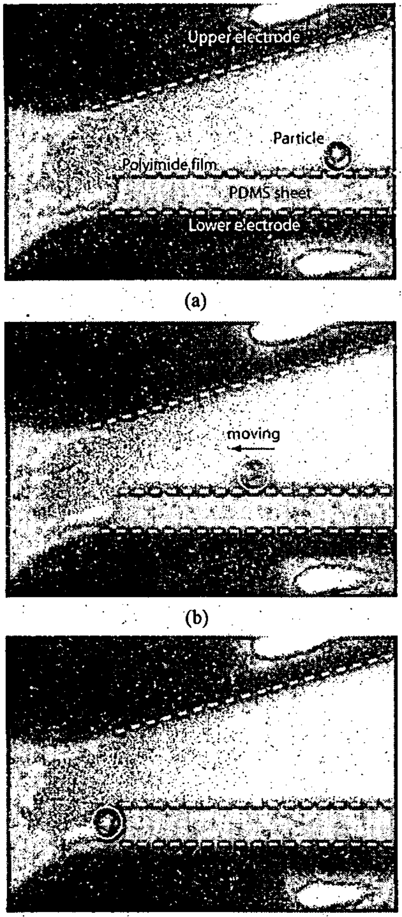

(a)

(b)

(c)

Figure 11. Temporal sequence of the particle positions when the first kind of the dielectric termination was used: (a) initial position; (b) movement after voltage application; (c) final position. The thickness of PDMS sheet is 1 mm.

According to the direction of the DEP force shown in Figures 9 and 10, it is implied that when the particle slightly passes the position of field maximum, it is still subject to the DEP force having a component in the $-x$ direction, pulling the particle back to the field maximum. Based on this observation, the second kind of dielectric termination was applied in the experiments, as shown in figure 12a. The initial position of the conducting particle was approximately the same as that in Figure 11a. The polyimide film was 1–2 mm longer than the PDMS. With the voltage application, the particle moved to the left hand side, and oscillated back and forth in the high field region (Figure 12b). The particle finally stopped at a point near the position of maximum field as shown in Figure 12c.

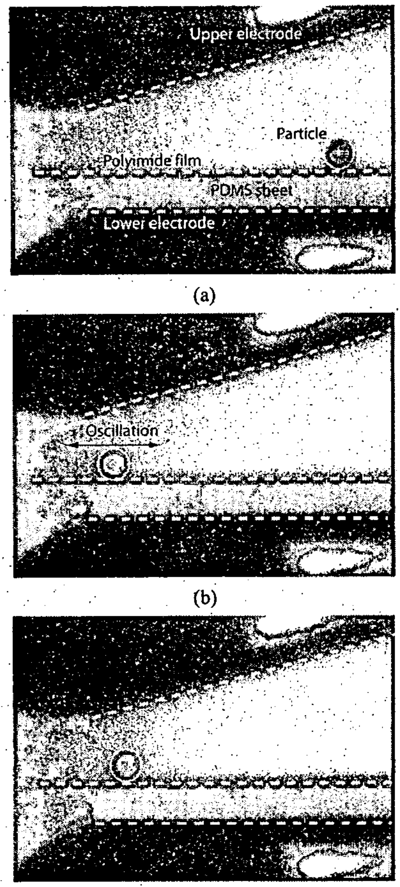

(a)

(b)

(c)

Figure 12. Temporal sequence of the particle images when the second kind of the dielectric termination was used: (a) initial position; (b) movement and oscillation after voltage application; (c) final position. The thickness of PDMS sheet is 1 mm.

The motion-onset voltage V_H was measured for the particles initially at the upper electrode height z_u between 4.5 and 6.0 mm. The average values of the measured V_H as a function of z_u are shown in Figure 13. For comparison with the theoretical V_H values, we also measured the friction force between the particles and the polyimide surface by using an angle-adjustable tilted plate. However, the measurement results varied significantly between experimental runs. The estimated V_H values based on the minimum and maximum magnitudes of the friction force are also given in the figure for comparison. From Figure 13, it is clear that V_H values from the experiments increase with the vertical gap length z_u. It is still inconclusive that the measured V_H values are higher or lower than the theoretical estimation.

The percentage of successful particle immobilization in the experiment also depended on the initial position of the particle. The aluminum particles initially at the upper electrode height z_u = 5, 5.5 and 6.5 mm were trapped at the dielectric termination by 100, 43 and 14% of the experimental runs, respectively. The stainless steel particles at z_u = 4.5, 5 and 5.5 mm were trapped by 100, 100 and 60%, respectively. With higher z_u values, the kinetic energy of the particle when it reached the dielectric termination was larger. The higher kinetic energy reflected the difficulty of particle immobilization. In addition, because higher electric field was required to initiate the particle motion with increasing z_u, the interference by the Coulomb force was also greater at the position of deactivation.

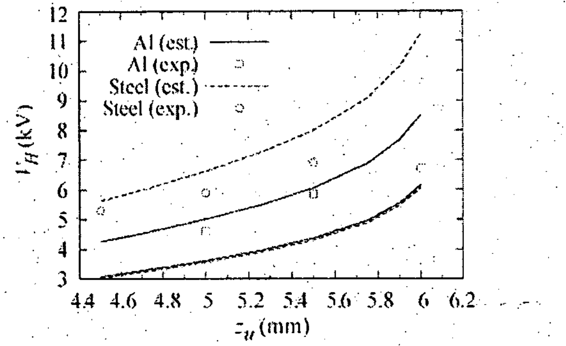

Figure 13. Measured motion-onset voltage (symbols) for the lateral movement of the aluminum and stainless steel particles in comparison with the minimum and maximum of the estimated values (solid and dashed lines).

7 CONCLUSION

In this work, we studied theoretically and experimentally the particle manipulation by using the DEP force. The simple configuration of nonparallel-plate electrodes was used with the insertion of dielectric layers to initiate and deactivate the particle motion. A numerical calculation was performed to confirm the distributions of the electric field and the force in the system. The experiments on the conducting particles were carried out to verify the theoretical prediction. We applied two kinds of the dielectric termination for the purpose of the particle deactivation. The experimental results confirmed the applicability of the DEP force for trapping; however, the performance deactivation still depended on the initial position of the particle. The motion-onset voltage of the particle from the experiment increased with the gap length.

ACKNOWLEDGMENT

This work was supported by the Thailand Research Fund (TRF) and the Graduate School, Chulalongkorn University. We would like to thank Prof. Noriyuki Hayashi of the University of Miyazaki and Dr. Kunihiko Hidaka of the University of Tokyo.

REFERENCES

[1] B. Qi, C. R. Li, Z. Hao, B. B. Geng, D. G. Xu, S. Y. Liu, and C. Deng, "Surface discharge initiated by immobilized metallic particles attached to gas insulated substation insulators: process and features", IEEE Trans. Dielectr. Electr. Insul., Vol. 18, pp.792–800, 2011.

[2] N.-J. Félici, "Forces et charges de petites objets en contact avec une electrode affecte d'un champ electrique", Rev. Gén. Elec., Vol. 75, pp. 1145–1160, 1966.

[3] N. N. Lebedev and I. P. Skal'skaya, "Force acting on a conducting sphere in the field of a parallel plate condenser", Sov. Phys. Tech. Phys., Vol. 7, pp. 268-270, 1962.

[4] M. Hara, T. Yamashita, and M. Akazaki, "Microdischarge characteristics in air gap between spherical particle and plane", IEE Proc., Part A, Vol. 130, pp. 329–335, 1983.

[5] S. P. Hornfeldt, "Lifting force on metallic particles in GIS systems", IEEE Trans. Dielectr. Electr. Insul., Vol. 13, pp. 838–841, 2006.

[6] K. Sakai, S. Tsuru, D. L. Abella, and M. Hara, "Conducting particle motion and particle-initiated breakdown in dc electric field between diverging conducting plates in atmospheric air", IEEE Trans. Dielectr. Electr. Insul., Vol. 6, pp.122–130, 1999.

[7] F. Endo, H. Goshima, M. Hanai, H. Hama, M. Hikita, and H. Okubo, "Metallic Particle Motion and Control under DC Voltages", Sympos. Electrical and Electronic Insulating Materials and Applications in Systems, pp. 49–52, Japan, 2004.

[8] K. Sakai, L. D. Abella, J. Suehiro, and M. Hara, "Charging and behavior of a spherically conducting particle on a dielectrically coated electrode in the presence of electrical gradient force in atmospheric air", IEEE Trans. Dielectr. Electr. Insul., Vol. 9, pp. 577–588, 2002.

[9] K. Sakai, D. L. Abella, Y. Khan, J. Suehiro, and M. Hara, "Theoretical and Experimental Studies for Spherical Free-Conducting Particle Behavior between Non-parallel Plane Electrodes with ac Voltages in Air", IEEE Trans. Dielectr. Electr. Insul., Vol. 10, pp. 404–417, 2003.

[10] Y. Khan, K. Sakai, E. K. Lee, J. Suehiro, and M. Hara, "Motion behavior and deactivation method of free-conducting particle around spacer between diverging conducting plates under DC voltage in atmospheric air", IEEE Trans. Dielectr. Electr. Insul., Vol. 10, pp. 444–457, 2003.

[11] M. Hara, H. Tobata, K. Hidaka, and H. Yakahe, "Influence of Conducting Particles on Insulation Performance of Conical Spacer in SF6, under DC Voltage", 5th Int'l. Sympos. HV Eng., Paper No. 15-03, Germany, 1987.

[12] M. Hara, K. Adachi, H. Tobata, M. Akazaki, and F. L. Mao, "Particle-Initiated Breakdown Characteristics of Conical Insulator in N2 Gas and N2/02 Mixture under DC Voltage", IEEE Trans. Electr. Insulat., Vol. 22, pp. 87–96, 1987.

[13] T. B. Jones, *Electromechanics of particles*, Cambridge University Press, 2005.

[14] A. Limsimarat and B. Techaumnat, "Electric field and force on a dielectric particle between two diverging plate electrodes", J. Electrostat., Vol. 63, pp. 789–794, 2005.

[15] T. Takuma and B. Techaumnat, *Electric Fields in Composite Dielectrics and their Applications*, Springer, Netherlands, 2010.

[16] B. Techaumnat and T. Takuma, "Analysis of the electric field and force in an arrangement of a conducting sphere and a plane electrode with a dielectric barrier", IEEE Trans. Dielectr. Electr. Insul., Vol. 13, pp. 336–344, 2006.

[17] C. A. Brebbia, L. C. Wrobel, and J. C. F. Telles, *Boundary Element Techniques: Theory and Applications in Engineering*, Springer-Verlag, Berlin, 1984.

[18] X. B. Wang, Y. Huang, J. P. H. Burt, G. H. Marks, and R. Pethig, "Selective dielectrophoretic confinement of bioparticles in potential energy wells", J. Phys. D: Appl. Phy., Vol. 26, pp. 1278–1285, 1993.

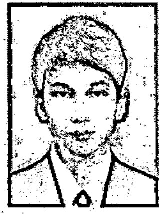

Nisarut Phansiri was born in Ubon Ratchathani, Thailand, on 8 June 1985. He received the B.E. degree in electronics engineering from King Mongkut's Institute of Technology Ladkrabang, Thailand, in 2008. He is now a master student at the department of electrical engineering (strategy research area of high-voltage engineering), at Chulalongkorn University, Thailand.

Boonchai Techaumnat (M'02) was born in Bangkok, Thailand in 1970. He received the B.Eng. degree in 1990, M. Eng. degree in 1995 from Chulalongkorn University, Thailand, and the doctoral degree in electrical engineering from Kyoto University in 2001. He joined the Faculty of Engineering, Chulalongkorn University as a lecturer in 1995. He is now an Associate Professor at the faculty. Dr. Techaumnat received the medal prize for new scholars from the Thailand Research Fund in 2005, the Nanobiotechnology Premium from the Institution of Engineering and Technology (IET) in 2009 and the book prize from the Institute of Electrical Engineers Japan in 2011 for "Electric Fields in Composite Dielectrics and their Applications". His research interests include numerical field analysis, electrical insulation, bioelectromagnetics, and particle electrokinetics.

Numerical Analysis of DC-Field-Induced Transmembrane Potential of Spheroidal Cells in Axisymmetric Orientations

Boonchai Techaumnat
Department of Electrical Engineering, Faculty of Engineering, Chulalongkorn University
Phyathai Road, Pathumwan, Bangkok 10330, Thailand

ABSTRACT

This paper presents the electrostatic analysis of direct-current and steady-state transmembrane potential of non-spherical biological cells. The purpose of this analysis is to clarify the influences of different cell geometries and conductivity of the extracellular medium on transmembrane potential. The cells are modeled as spherical or spheroidal and as having different ratios between the radii in different axial directions. The boundary element method, a numerical method, is applied to the calculation of the transmembrane potential. The calculations show that a decrease in the conductivity affects both magnitude and distribution of transmembrane potential. The cell membrane can be approximated as a perfect dielectric, provided that the conductivity of the extracellular medium is sufficiently high. For the same cell geometries, transmembrane potential is smaller for pairs of cells than for isolated cells, and this potential is more reduced at the contact poles than at the opposite poles. Either different axial lengths or different radii between the cells results in this disparity in transmembrane potential of the cell pair. However, the maximum potential of both cells approaches the same value and is located at the contact poles if the conductivity in the extracellular medium is very low.

Index Terms — **Electrostatic analysis, biological cells, biomembranes, electric fields, spheroids, conductivity, boundary element methods.**

1 INTRODUCTION

ELECTROSTATIC field effects are utilized in various applications involving biological cells [1]. When a suspension of cells is exposed to an electric field, charges of opposite polarities accumulate on both sides of the cell membrane, a layer of lipid molecules, by electric current. The accumulation of charges produces a transmembrane potential, whose magnitude depends on cell size, electric field strength, cell orientation with respect to the field direction, and electrical parameters of the media involved. Transmembrane potential is an important parameter in cell lysis, electroporation and electrofusion of biological cells [2]. When transmembrane potential reaches a critical value, membrane breakdown occurs. This breakdown may be reversible, i.e., the membrane can re-attain its insulating property after the applied electric field is removed, or permanent (resulting in cell death).

The analytical solution of transmembrane potential is available for an isolated spheroidal cell in a uniform field [3-7]. For an isolated spherical cell with a perfect dielectric membrane in a uniform electric field E_0, the analytical solution of the steady-state transmembrane potential V_m is

$$V_m = \frac{3}{2} E_0 R \sin\theta \qquad (1)$$

where R is the radius of the cell and θ is the zenith angle indicating position on the membrane. The time constant of the potential buildup depends on cell size, membrane capacitance, and conductivity of the intracellular and extracellular fluids.

Actual biological cells, such as those adhered to a surface, may have non-spherical shapes. Cell shape may also change under electric field stress or pressure. However, transmembrane potential of non-spherical cells has not been fully studied. For cells with complex geometries, numerical methods must be used to determine their transmembrane potential. In addition, the calculation is more complicated when cells exist near or in contact with each other, although the method of re-expansion can be applied to configurations of spherical cells [8].

This work presents a numerical analysis of a direct-current (DC) steady-state transmembrane potential of biological cells in an external electric field. The main objective of the analysis is to investigate the effects of (i) cell geometries, (ii) conductivity of extracellular medium and (iii) contact between cells on transmembrane potential. For cell geometries, cells are modeled as either oblate or prolate spheroids and compared with the spheres. Although cells are usually suspended in highly conductive medium, the conductivity is sometimes reduced to limit Joule heating in various procedures. Low conductivity media are also used in

---

Manuscript received on 19 October 2012, in final form 10 June 2013.

electrofusion protocols to obtain cell contact by dielectrophoresis. The boundary element method is utilized for calculations, in which the cell membrane is modeled either as a perfect dielectric medium or conductive medium to clarify the effect of membrane conductivity on the calculation results.

2 CONFIGURATIONS OF ANALYSIS

Figure 1 shows the configurations of cells used for analysis. Only the axisymmetric configurations are considered in this work. Figure 1a shows an isolated cell under an external electric field $\mathbf{E}_0$. Cell geometries are defined by axial length a, which is parallel to the external electric field, and radius R, which is normal to the field, as shown in the figure. For a spherical cell, $a = R$. In Figure 1b, two cells are in contact and aligned in the direction of the external electric field. Subscripts 'l' and 'u' are used to denote the parameters of the lower and upper cells, respectively. This configuration is of practical importance for the process of electrofusion, in which cells are brought into contact with each other before electric pulses initiate membrane breakdown [2, 9]. The cells in the pair may be of the same or different geometries. The conductivity of the cytoplasm in the interior of the cell is denoted by μ_I and that of the external medium is μ_E.

3 CALCULATION METHOD

The boundary element method (BEM), which is an integral-based numerical method, is used to calculate steady-state transmembrane potential. ϕ^E and E_n^E are the potential on the membrane and electric field normal to the cell membrane Γ, respectively, on the exterior of the cell. Since the membrane is very thin compared with the cell size, it is treated geometrically as a zero-thickness surface. We can write potential ϕ in the exterior in terms of the integrals of ϕ^E and E_n^E as [10]

$$c^E\phi(\mathbf{r}) = \int_\Gamma \psi(\mathbf{r},\mathbf{r}_s)E_n^E\,\mathrm{d}S + \int_\Gamma \frac{\partial\psi(\mathbf{r},\mathbf{r}_s)}{\partial n}\phi^E\,\mathrm{d}S - \mathbf{E}_0\cdot(\mathbf{r}-\mathbf{r}_0) \tag{2}$$

where $\mathbf{r}$ is the position of the potential to be evaluated, $\mathbf{r}_s$ is the position on the membrane surface, and $\mathbf{r}_0$ is the reference point of zero potential. $\psi(\mathbf{r}, \mathbf{r}_s)$ is the fundamental solution. Note that positive normal n is taken in the direction from the interior of the cell to the exterior. The constant c^E in equation (2) depends on the solid angle at $\mathbf{r}$: $c^E = 1$ if $\mathbf{r}$ is not on the boundary, and $c^E = 1/2$ if $\mathbf{r}$ is on a smooth boundary interface. For axisymmetric configurations, in which the coordinates of $\mathbf{r}$ are defined by (ρ, z), the fundamental solution is expressed as

$$\psi(\mathbf{r},\mathbf{r}_s) = \frac{K\left(\sqrt{2n/(m+n)}\right)}{\sqrt{m+n}} \tag{3}$$

K is the complete elliptic integral of the first kind, and

$$m = \rho^2 + \rho_s^2 + (z - z_s)^2 \tag{4}$$

$$n = 2\rho\rho_s \tag{5}$$

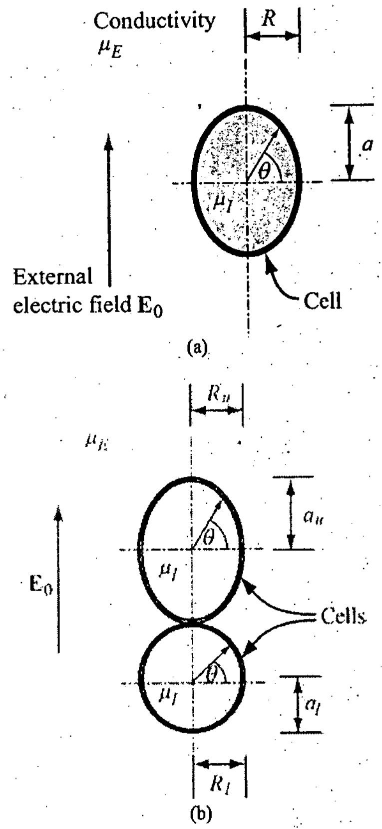

Figure 1. Configurations of cells used for analysis: (a) isolated cell and (b) cell pair.

For the BEM, we discretize the cell membrane Γ into elements, and express ϕ^E and E_n^E with nodal values $\phi_i^E = \phi(\mathbf{r}_i)$ and $E_{n,i}^E = E_n^E(\mathbf{r}_i)$ as

$$\phi^E(\mathbf{r}_s) = \sum N_i(\mathbf{r}_s)\phi_i^E \tag{6}$$

$$E_n^E(\mathbf{r}_s) = \sum N_i(\mathbf{r}_s)E_{n,i}^E \tag{7}$$

where N_i is the interpolating function associated with the ith node for $i = 1, 2, \ldots, n_N$. Applying equation (2) at the node position $\mathbf{r} = \mathbf{r}_i$, from equations (3)–(7) we obtain n_N linear equations, which may be written in matrix form as

$$[H_E][\phi^E] = [G_E][E_n^E] + [\phi_{E0}] \tag{8}$$

$[\phi^E]$ and $[E_n^E]$ are $n_N \times 1$ matrices of the nodal values, $[H_E]$ and $[G_E]$ are $n_N \times n_N$ matrices determined from the boundary integral, and $[\phi_{E0}]$ corresponds to the last term on the right hand side of equation (2).

For the interior of each cell, the relationship between the potential ϕ^I and normal component E_n^I of the electric field on the membrane is

$$c^I\phi^I(\mathbf{r}) = -\int_\Gamma \psi(\mathbf{r},\mathbf{r}_s)E_n^I\,\mathrm{d}S - \int_\Gamma \frac{\partial\psi(\mathbf{r},\mathbf{r}_s)}{\partial n}\phi^I\,\mathrm{d}S \tag{9}$$

where $c^I(\mathbf{r}) + c^E(\mathbf{r}) = 1$. In a similar manner to the formulation of equation (7), we can obtain linear equations

$$[H_I][\phi^I] = [G_I][E_n^I] \tag{10}$$

The boundary condition to be satisfied in the steady state is

$$\mu_I[E_n^I] = \mu_E[E_n^E] \tag{11}$$

For the biological cells, another boundary condition of current density is needed to relate the potential and the normal component of the electric field

$$\frac{\mu_m}{t_m}([\phi^I] - [\phi^E]) = \mu_I[E_n^I] = \mu_E[E_n^E] \tag{12}$$

where μ_m is the membrane conductivity and t_m is the membrane thickness. The transmembrane potential V_m is defined here as

$$V_m = \phi^I - \phi^E \tag{13}$$

If the membrane is treated as a perfect dielectric ($\mu_m = 0$), we can simplify the calculation. Equations (11) and (12) become trivial as the current normal to the membrane vanishes in the steady state because the membrane has no conductivity. That is, we can apply the condition of zero normal field to all $E_{n,i}^E$ and solve the linear equation system (8) for unknown ϕ_i^E without needing to consider equations (10)–(12). For each cell, the potential ϕ_i^I on the membrane in the interior has a single value because the electric field is zero everywhere inside the cell if the membrane is a perfect dielectric. Based on the fact that the transmembrane potential V_m originates from charges that accumulate on both sides of the membrane and an assumption that the total charge inside each cell is equal to zero, it can be deduced that

$$\int_{\Gamma}(\phi^E - \phi^I)\mathrm{d}S = 0 \tag{14}$$

The integral is taken over the membrane of each cell. In other words, ϕ^I is the average value of ϕ^E over the entire cell membrane surface. It is worth noting here that with the use of the appropriate fundamental solution $\psi(\mathbf{r}, \mathbf{r}_s)$, the calculation principles described here can be applied to any configurations not limited to the axisymmetric case alone.

4 RESULTS AND DISCUSSION

4.1 CELL PROPERTIES AND MODEL

In the calculation, the conductivity μ_I of the intracellular fluid is equal to 0.2 S/m, a typical value for the cytoplasm. The conductivity μ_E of the extracellular medium is varied from 0.1 mS/m to 1 S/m. The membrane conductivity μ_m used for calculations is 0.5 μS/m and the membrane thickness t_m is 5 nm [11]. Note that the membrane specific capacitance, which is about 1 μF/cm^2, is not involved in the steady state calculations. The variation of cell geometries analyzed in this work is illustrated in Figure 2. For oblate spheroidal cells, axial length a = 10 μm, and cell radius is varied to obtain a/R = 1/4 and 1/2. The spherical cell has $a = R$ = 10 μm. For the prolate spheroidal cells, R = 10 μm, and axis length is increased to obtain a/R = 2 and 4. Therefore, the smallest dimension of the cells, which can be either axial length a or radius R, is equal to 10 μm in all of the calculations.

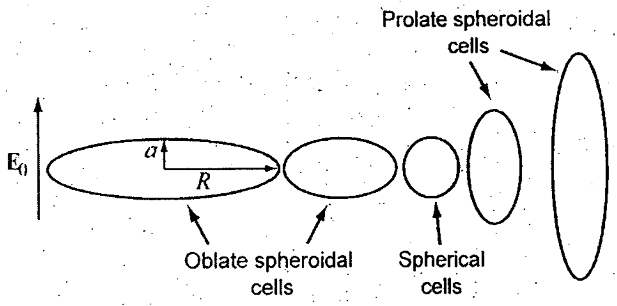

Figure 2. Variation of cell geometries used for analysis. The axial length a = 10 μm for the oblate spheroidal cells, and the radius R = 10 μm for the prolate spheroidal cells.

For the boundary element calculation, the cell membrane is discretized into 128 or more elements depending on the cell geometries. Second-order curved elements are used to attain high accuracy results.

4.2 ISOLATED CELLS

Figure 3 shows the transmembrane potential V_m, normalized by aE_0, of an isolated spherical cell as a function of zenith angle θ (see Figure 1) for various values of exterior conductivity μ_E. From the figure, we can see that for $\mu_E \geq 0.1$ S/m, the transmembrane potential reaches its limiting value for a spherical cell, which is equal to $1.5aE_0$ at the poles in the case of a perfect dielectric membrane [3]. With μ_E = 0.01 S/m, the potential is still close to the limit. Further decreases in exterior conductivity result in lower magnitudes of transmembrane potential; for example, the maximum V_m of a spherical cell is reduced by 33% when μ_E = 0.001 S/m.

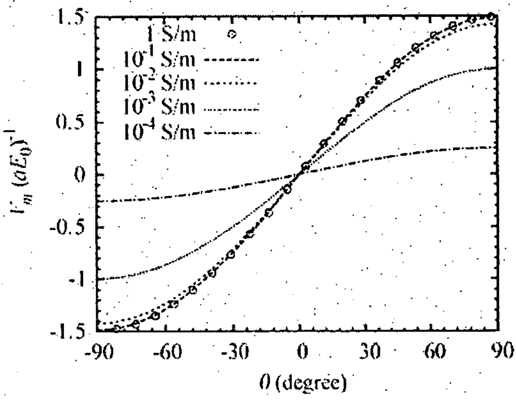

Figure 3. Transmembrane potential of an isolated spherical cell for various μ_E values.

The analytical solution of the transmembrane potential is available for isolated spherical and spheroidal cells under a uniform electric field [4, 7]. Figure 4 compares the maximum transmembrane potential (at the top and bottom poles of spherical cells) calculated by the BEM with the analytical solution given in [4]. It is clear from the figure that the numerical results agree very well with the analytical solution for all μ_E values considered here.

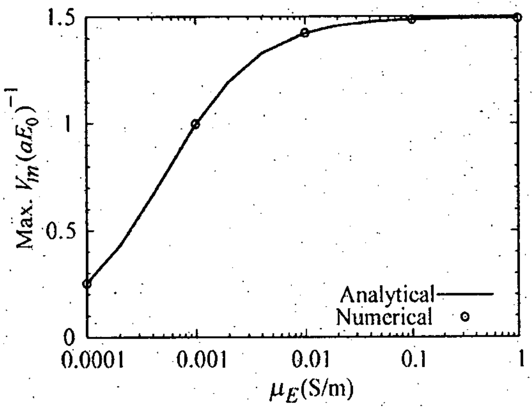

Figure 4. Comparison of the maximum transmembrane potential at the poles of an isolated spherical cell with the analytical solution.

The distribution of transmembrane potentials on isolated non-spherical cells is calculated for various exterior conductivity values. The calculation results are shown in Figures 5a and 5b for oblate spheroidal cells and Figures 5c and 5d for prolate spheroidal cells. From the figures, we can see that the variation of the transmembrane potential on the spheroidal cells is similar to that of spherical cells. That is, the magnitude of the transmembrane potential is substantially reduced when the external conductivity is lower than 10^{-2} S/m. However, one may notice that the reduction of transmembrane potential by lowering the exterior conductivity is more prominent for the oblate spheroidal cells than for the prolate spheroidal cells. As shown in Figures 5a and 5b, the region of high transmembrane potential is wider on the oblate spheroidal cells than on the spherical cells shown in Figure 3. This tendency is reversed for the prolate spheroidal cells, whose transmembrane potential is shown in Figures 5c and 5d.

Figure 6 compares the calculated maximum transmembrane potential of spheroidal cells (at the poles) with the analytical solution [4] for various values of a/R. The cell profiles are referred to Figure 2. From the figure, a good agreement can be observed between the numerical results (symbols) and the analytical values (lines). However, whereas we cannot see any difference between the numerical and analytical values for the spherical cell in Figure 4, the calculation results slightly deviate from the analytical solution for the spheroidal cells as shown in Figure 6. The calculated maximum V_m is higher than the analytical value for the oblate spheroidal cells and lower than the analytical value for the prolate spheroidal cells. The disparity increases as the axis-to-radius ratio differs more from one. In addition to numerical errors, another potential cause of the disparity between the calculation results and the analytical solution is the assumption of a confocal membrane in the analytical method, which is based on spheroidal coordinates. As the thickness of the confocal membrane varies with the position, it is implied that the conductivity of the cell membrane is nonuniform for a constant specific conductance μ_m/t_m value.

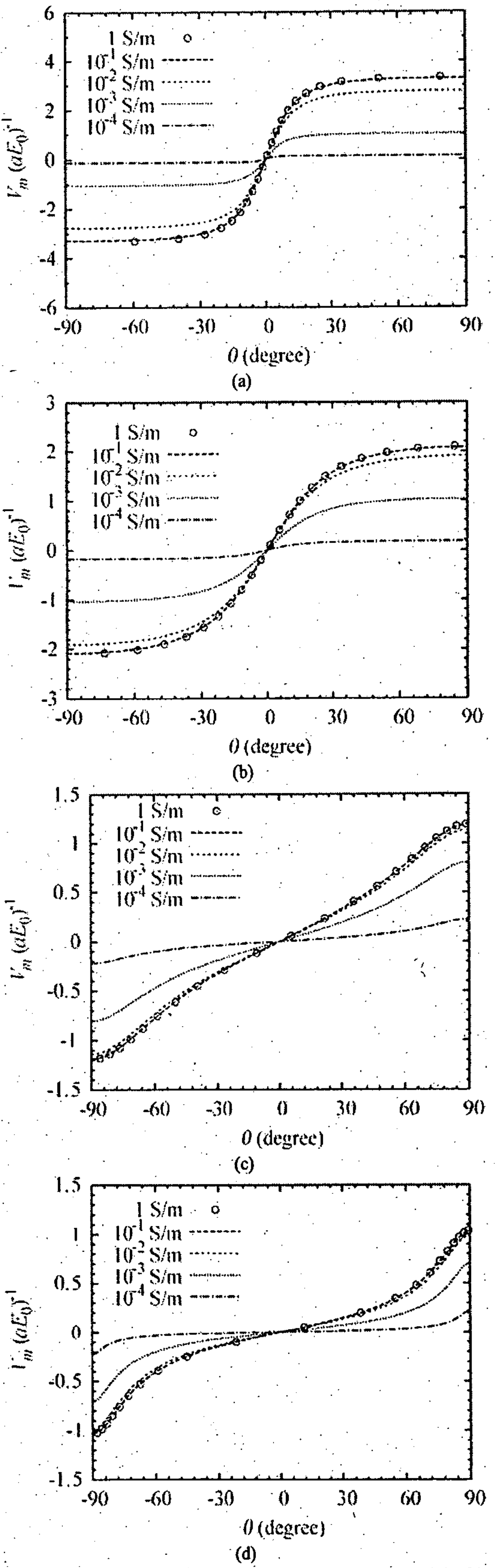

Figure 5. Distribution of the normalized transmembrane potential of isolated spheroidal cells for various μ_E values. (a) $a/R = 1/4$, (b) $a/R = 1/2$, (c) $a/R = 2$, and (d) $a/R = 4$.

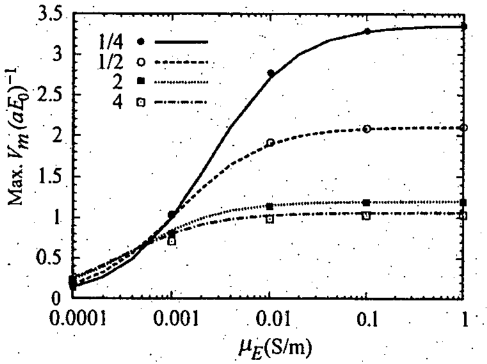

Figure 6. Comparison of the maximum transmembrane potentials obtained from the numerical calculation (symbols) with the analytical solution (lines) for the isolated spheroidal cells.

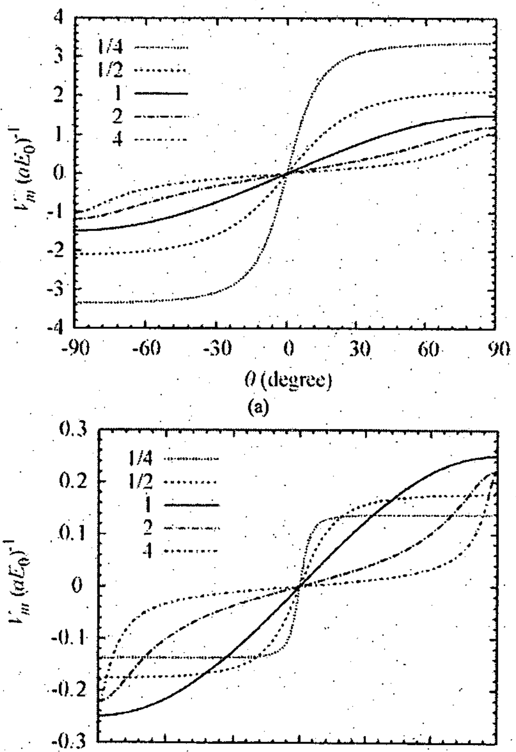

(a)

(b)

Figure 7. Comparison of the normalized transmembrane potential between cells with different axis-to-radius ratios. (a) $\mu_E = 1$ S/m, (b) $\mu_E = 10^{-4}$ S/m.

Figure 7 compares the normalized transmembrane potential of cells with different a/R ratios when they are in a high conductivity (μ_E = 1 S/m) and low conductivity (μ_E = 10^{-4} S/m) media. When the conductivity of the extracellular medium is sufficiently high, the normalized transmembrane potential consistently increases with decreasing axis-to-radius ratio as shown in Figure 7a. On the other hand, when the conductivity is low (Figure 7b), the normalized transmembrane potential is highest for the spherical cell and decreases with either increasing or decreasing axis-to-radius ratio. Note that this behavior depends on the condition of cell geometries illustrated in Figure 2. If the axial length a is held constant and the radius R is varied for all cell profiles, the transmembrane potential in Figure 7b will increase monotonously with an increasing a/R ratio, which can be explained by using the concept of influential radius [4].

4.3 CELL PAIR WITH PERFECT DIELECTRIC MEMBRANE

This section discusses the transmembrane potential of a cell pair in the configuration of Figure 1b when the cell membrane is modeled as a perfect dielectric. We begin with the case of an identical cell pair, i.e., $a_l = a_u = a$ and $R_l = R_u = R$. Note that for a perfect dielectric membrane, the exterior conductivity μ_E affects the time constant of the membrane charging, but does not have any influence on the steady-state potential. Figure 8 shows the transmembrane potential on the lower cell for different cell geometries, where a/R is varied from 1/4 to 4. It can be seen from the figure that the transmembrane potential of the cells is clearly smaller when compared with that in Figure 7a of the isolated cells. There is more reduction in the normalized potential at the contact pole (θ = 90°) than at the opposite pole (θ = −90°). These results agree with those reported for spherical cell pairs [6]. The variation in normalized transmembrane potential at both poles due to cell geometry is summarized in Figure 9. The analytical solution [7] in the corresponding case for isolated cells is also plotted as the dotted line in Figure 9 to clarify the reduction of transmembrane potential. It is clear from Figures 8 and 9 that the potential reduction is enhanced with decreasing a/R ratio, i.e., more prominent for the oblate spheroidal cells than for the prolate spheroidal ones.

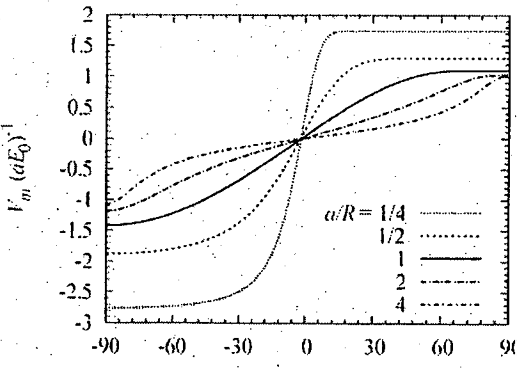

Figure 8. Transmembrane potential on the lower cell of the identical cell pair for different values of a/R.

Figure 10 presents the effect of cell sizes on transmembrane potential when both cells are spherical ($a_u = R_u$ and $a_l = R_l$) but have different sizes. Here we assume that the upper cell is the larger one. Although the results are practically similar to those in reference [6], they are worth given here for comparison with the case of non-spherical cells. In Figure 10, the potential of both upper and lower cells is normalized by a_lE_0 and plotted on the same graph. The contact point is at θ = 90° of the lower cell and −90° of the upper cell. It can be clearly seen from the graph that the larger (upper) cell has a higher transmembrane potential. The potential of the smaller (lower) cell decreases with increasing the size of the upper cell. We may refer that the reduction in V_m results from a "shielding effect". For electrofusion, the optimal transmembrane potential (about 1 V) at the contact point of both cells is critical for attaining high yield from the process [2, 12]. Figure 10 clearly demonstrates the difficulty in achieving effective electrofusion between differently-sized cells.

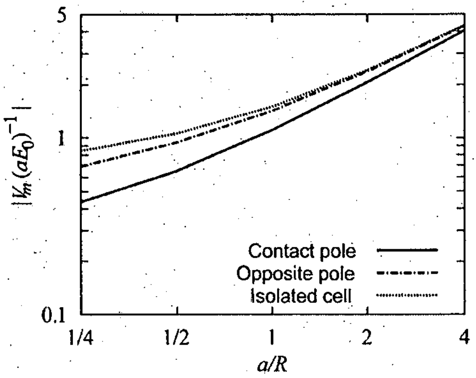

Figure 9. Variation of transmembrane potential at the cell poles due to changes in a/R.

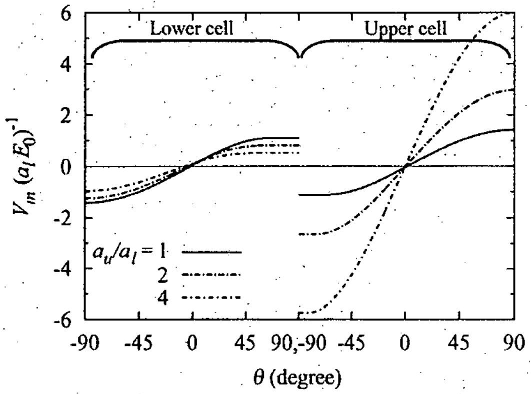

Figure 10. Transmembrane potential of pair of spherical cells with different cell sizes.

The shielding effect is also investigated for a pair of cells having different shapes (axis-to-radius ratios). In this case, the lower cell is spherical, whereas the ratio a_u/R_u of the upper cell is varied from oblate spheroidal to prolate spheroidal. To observe the shielding effect of the upper cell on the lower cell, the lower cell is designated to be the smaller of the pair. That is, we take $a_u = a_l = R_l$ and increase the radius R_u when the upper cell is an oblate spheroid. When the upper cell is a prolate spheroid, we take $R_u = R_l = a_l$ and increase the axial length a_u. Figures 11a and 11b present the distribution of the normalized transmembrane potential on the cell pair when the upper cell is oblate spheroidal and prolate spheroidal, respectively. Note that the normalizing factor for the potential on the graphs is based on the axial length of the lower cell, which is the same value for both graphs. It is clear from Figure 11a that the shielding effect depends mainly on the radius of the cell, as the transmembrane potential of the smaller (lower) cell is significantly reduced when the upper cell is oblate spheroidal. On the other hand, in Figure 11b, an increase in the axial length of the upper cell results in a slight increase in the transmembrane potential near the contact point of the lower cell; the change is hardly noticeable on any other portion of the lower cell. It is also worth noting that the magnitudes of the potential near the contact point (at $\theta = -90°$) of the upper cells in Figure 11a are higher than the corresponding values for a pair of identical oblate spheroidal cells (at $\theta = 90°$ in Figure 8). This indicates the mitigation of the shielding effect on the upper cell when the size of the other cell in the pair is smaller. In Figure 12, the absolute values of the normalized transmembrane potentials at the poles of the lower spherical cell are plotted as a function of a/R of the upper spheroidal cell. The figure shows that with decreasing a/R, the magnitudes of the transmembrane potentials are reduced at both poles.

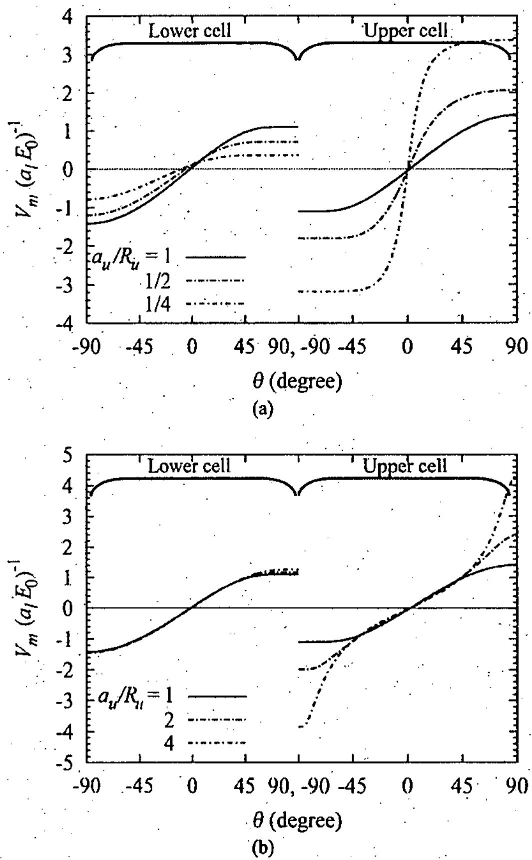

(a)

(b)

Figure 11. Transmembrane potential on the lower spherical cell ($a_l = R_l = 10$ μm) and upper spheroidal cell when the upper cell is (a) an oblate spheroidal cell with $a_u = 10$ μm and (b) a prolate spheroidal cell with $R_u = 10$ μm.

Figure 11 clearly shows that the disparity between the transmembrane potential at the contact points of the upper and lower cells is magnified by increasing either radius or axial length of a cell in the pair. The oblate spheroidal cells have higher transmembrane potentials and cause a reduction in the potential of the other cell in the pair. The prolate spheroidal cells have higher transmembrane potentials than the oblate ones, although they do not significantly affect the potential of the lower cell.

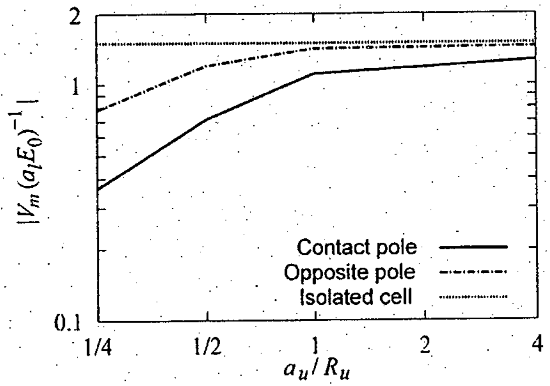

Figure 12. Absolute values of the normalized transmembrane potential at the poles of the lower spherical cell as a function of a/R of the upper cell.

4.4 CELL PAIR WITH CONDUCTIVE MEMBRANES

Section 4.2 described the influence of exterior conductivity on transmembrane potential. In this section, the influence is further investigated for the configuration of a cell pair shown in Figure 1b. Figure 13 shows the distribution of the transmembrane potential on the lower cell of a spherical cell pair having the same size for different μ_E values. It can be seen from the figure that lower exterior conductivity results in a decreased potential. The potential decreases more at the bottom pole than at the top pole, which is the contact point between the cells. With sufficiently low conductivity, the magnitude of the transmembrane potential becomes larger at the contact pole than at the opposite pole, as shown in Figure 13. The area with high transmembrane potential also becomes smaller at reduced exterior conductivity values. Under such conditions, it becomes possible to restrict membrane breakdown to the vicinity of the contact point.

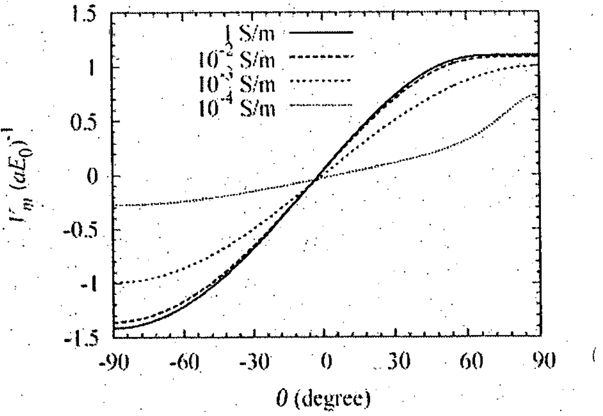

Figure 13. Variation of transmembrane potential distribution on the lower cell of an identical spherical cell pair at different exterior conductivity (μ_E) values.

The variation of transmembrane potential due to μ_E for the non-spherical cell pair is shown in Figure 14 for identical spheroidal cells. From the figure, we can observe higher degree of transmembrane potential reduction at the bottom pole than at the top pole, much like that seen in Figure 13 for spherical cells.

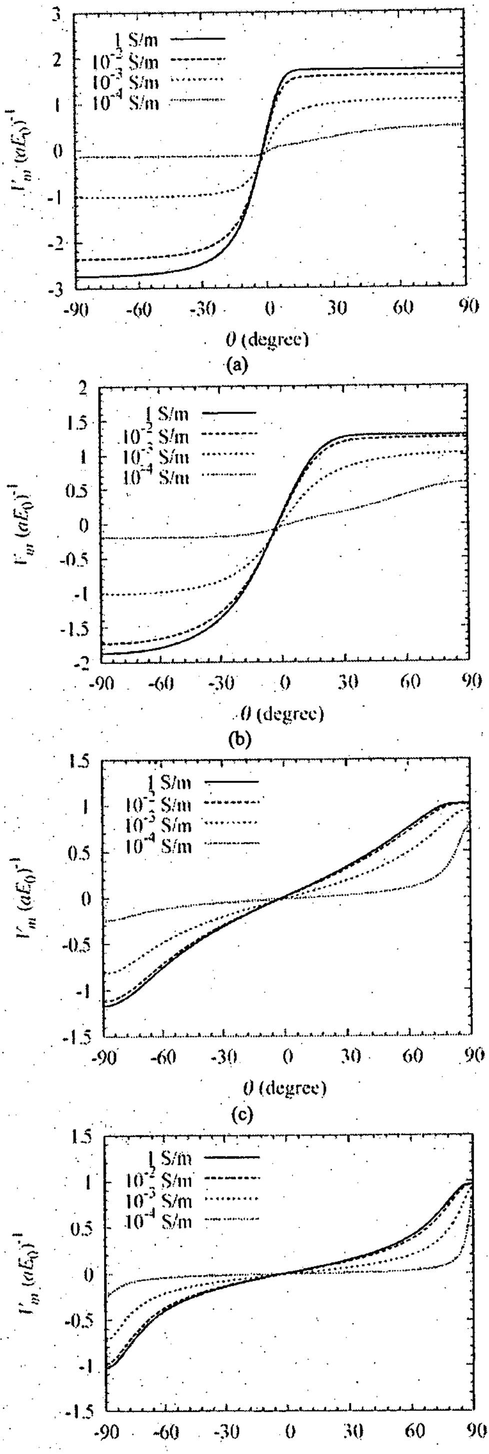

(a)

(b)

(c)

(d)

Figure 14. Transmembrane potential distribution on the lower cell of the identical spheroidal cell pair for various μ_E values. (a) $a/R = 1/4$, (b) $a/R = 1/2$, (c) $a/R = 2$ and (d) $a/R = 4$.

In comparing Figures 13 and 14, for the oblate spheroidal cells, the area of high transmembrane potential in Figures 14a and 14b is still considerably large unless the exterior conductivity is very low. In particular, it is almost impossible to limit the area of high transmembrane potential when a/R is small, as shown in Figure 14a. For prolate spheroidal cells, the influence of the exterior conductivity on the transmembrane potential at the contact point (top pole) is comparatively very small, as shown in Figures 14c and 14d. However, the area of high transmembrane potential near the contact point becomes smaller with decreasing μ_E. At the other pole, a decrease in μ_E reduces the transmembrane potential, but the potential distribution is more or less the same.

The magnitudes of transmembrane potential at cell poles are plotted as a function of external conductivity in Figures 15a for the oblate spheroidal cell pairs and 15b for the prolate spheroidal cell pairs. The lines and the symbols represent the potential at the contact pole and opposite pole, respectively. From the figures, it is clear that the potential magnitude is smaller at the contact pole than at the opposite pole. However, the difference between the potential at the poles can be reduced by decreasing μ_E. With very low μ_E, the potential can be higher at the contact pole.

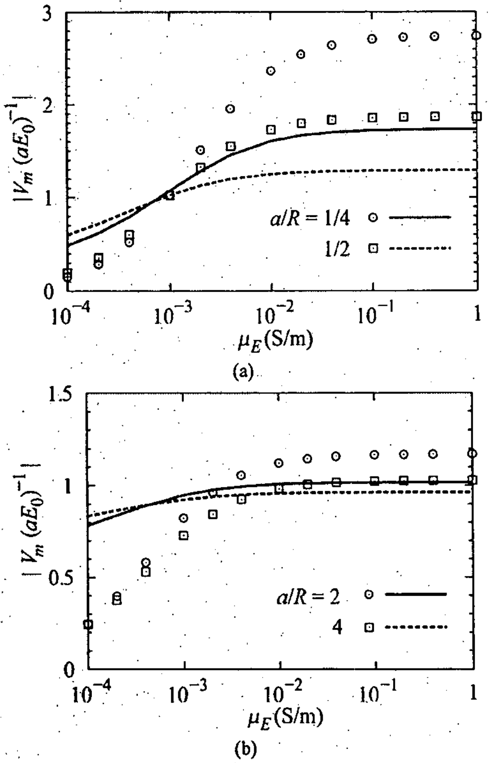

Figure 15. Absolute values of the normalized transmembrane potential at the contact pole (lines) and opposite pole (symbols) for a pair of identical spheroidal cells as a function of μ_E. (a) Oblate spheroidal cells and (b) prolate spheroidal cells.

Table 1 compares the saturation values (when μ_E = 1 S/m) of the normalized potential at the contact point for cells with conductive membranes (Figure 15) and cells with perfect-dielectric membranes (Figure 9). The table shows that the difference between the potential values is very small for the oblate spheroidal cells and increases with larger values of a/R. As the difference is only 5.83% for a/R = 4, the perfect-dielectric membrane model may be used to approximate the transmembrane potential for the axis-to-radius ratios considered here.

Table 1. Comparison of the normalized transmembrane potential, $V_m(aE0)^{-1}$, at the contact pole between the cases with dielectric membranes and conductive membranes.

a/R	$V_m(aE0)^{-1}$ at the contact point		Difference (%)
	Dielectric membrane	Conductive membrane	
1/4	1.740	1.733	0.40
1/2	1.299	1.292	0.54
1	1.105	1.098	0.64
2	2.065	2.034	1.52
4	4.036	3.850	5.83

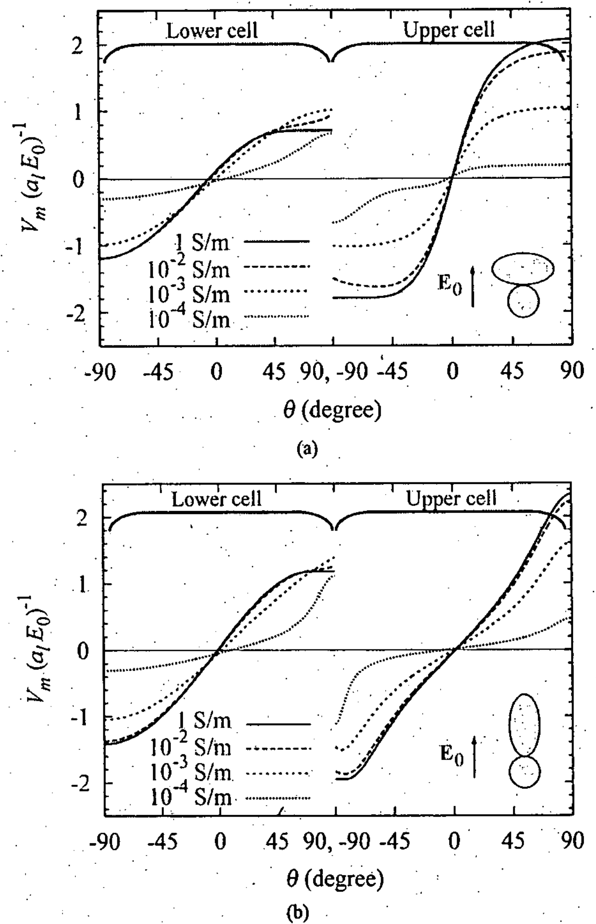

Figure 16. Transmembrane potential on the lower spherical cell ($a_l = R_l$ = 10 μm) and upper spheroidal cell that is (a) an oblate spheroid with a_u = 10 μm and a_u/R_u = 1/2, or (b) a prolate spheroid with R_u = 10 μm and a_u/R_u = 2.

When the cells in the pair are of different geometries, the behavior of the transmembrane potential becomes more complicated. The distribution of the potential is demonstrated in Figure 16 for a lower spherical cell and an upper spheroidal cell. Similar to the previous cases with a perfect dielectric membrane, $a_u = a_l$ for the oblate spheroidal cell and $R_u = R_l$ for the prolate spheroidal cell such that the lower cell is the smaller one. As can be seen from the figure, for low exterior conductivity, the transmembrane potential is reduced on both cells except near the contact point (the top pole) of the lower spherical cell. Instead, in this area the potential may be reduced or enhanced with decreasing exterior conductivity. On the spheroidal (upper) cell, the potential is reduced more significantly at the top pole than at the bottom pole.

The absolute values of the potential at the contact point between the upper spheroidal and lower spherical cells are plotted as a function of exterior conductivity in Figure 17a for the case of an oblate spheroid and 17b for the case of a prolate spheroid. In the figures, the open and solid (circular and rectangular) symbols represent the potential on the upper and lower cells, respectively. It is clear from the figure that with decreasing the exterior conductivity, the transmembrane potential at the contact point of both cells approaches the same value. For low exterior conductivity, the transmembrane potential at the contact point differs only slightly for $a/R_u = 1/4$ and 1/2 (Figure 17a), whereas the difference is clear for $a/R_u = 2$ and 4 (Figure 17b). Therefore, with an extracellular medium of sufficiently low conductivity, the steady-state transmembrane potential at the contact point is governed mainly by the axial length of the cells.

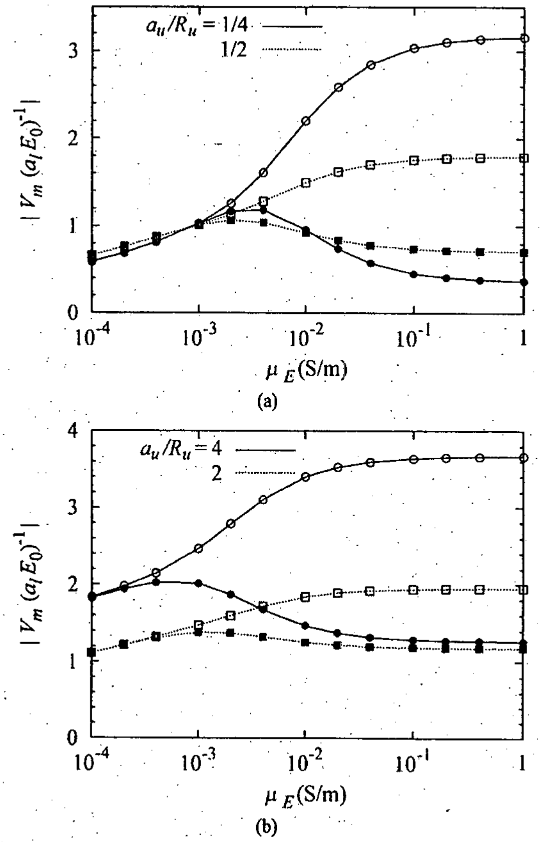

Figure 17. Absolute values of the normalized transmembrane potential at the contact poles as a function of μ_E for the lower spherical cell ($a_l = R_l = 10$ μm) paired with (a) an oblate spheroid with $a_u = 10$ μm or (b) a prolate spheroid with $R_u = 10$ μm.

5 CONCLUSION

In this work, a numerical method was used to analyze the transmembrane potential of isolated cells and cell pairs. The results may be summarized as follows:

Isolated cell:

The calculation results agree well with the analytical solution. Decreases in the conductivity of the extracellular medium may reduce the magnitude of V_m. The influence of exterior conductivity is observable when $\mu_E < 0.1$ S/m and is more prominent for oblate spheroidal cells than for prolate spheroidal cells. Normalized V_m increases with decreasing the axis-to-radius ratio a/R of the cell for high μ_E medium conditions. In low μ_E medium, normalized V_m is maximal on the spherical cell for the cell geometries considered in this work.

5.1 CELL PAIR

For spherical and oblate spheroidal cells, V_m of an identical pair of cells in contact with each other is smaller than for isolated cells. When the sizes of the cells are different, V_m is clearly reduced on the cell with a smaller radius. This size difference, which can be due to differences in axial length or radius of cells, usually results in a disparity of membrane potential at the contact point between the cells, and implies difficulty in achieving efficient electrofusion. Decreases in the conductivity of the extracellular medium reduce the magnitude of V_m, but the reduction is small near the contact point in comparison with other regions. In particular, the reduction of V_m is very small for prolate spheroidal cells. When the extracellular conductivity is sufficiently low, the membrane potential is maximal at the contact point and approaches the same magnitude for both cells in the pair.

ACKNOWLEDGMENT

This work has been supported by the Thailand Research Fund (TRF). The author wants to thank Prof. Masao Washizu of the University of Tokyo, Japan.

REFERENCES

[1] J.-S. Chang, A.J. Kelly and J.M. Crowley, Eds., *Handbook of Electrostatic Processes*, Marcel Dekker, Inc., New York, Ch.29, 1995.

[2] U. Zimmermann, W.M. Arnold, and W. Mehrle, "Biophysics of electroinjection and electrofusion", J. Electrostatics, Vol. 21, pp. 309-345, 1988.

[3] E. Jeltsch and U. Zimmermann, "Particles in a homogeneous electrical field: A model for the electrical breakdown of living cells in a coulter counter", J. Electroanal. Chem. and Interfac. Electrochem., Vol. 104, pp. 349-384, 1979.

[4] J. Gimsa and D. Wachner, "Analytical description of the transmembrane voltage induced on arbitrarily oriented ellipsoidal and cylindrical cells", Biophys. J., Vol. 81, pp. 1888-1896, 2001.

[5] J. Gimsa and D. Wachner, "On the analytical description of transmembrane voltage induced on spheroidal cells with zero membrane conductance", Eur. Biphys. J., Vol. 30, pp. 463-466, 2001.

[6] B. Valič, M. Golzio, M. Pavlin, A. Schatz, C. Faurie, B. Gabriel, J. Teissié, and M.-P. Rols, "Effect of electric field induced transmembrane potential on spheroidal cells: theory and experiment", Eur. Biphys. J., Vol. 32, pp. 519-528, 2003.

[7] T. Kotnik and D. Miklavcic, "Analytical Description of Transmembrane Voltage Induced by Electric Field on Spheroidal Cells", Biophys. J., Vol. 79, pp.670-679, 2000.

[8] M. Washizu and B. Techaumnat, "Cell membrane voltage during electrical cell fusion calculated by re-expansion method", J. Electrostatics, Vol. 65, pp. 555-561, 2007.

[9] N. Urano, M. Kamimura, T. Nanba, M. Okada, M. Fujimoto, and M. Washizu, "Construction of a yeast cell fusion system using a fluid integrated circuit", J. Biotechnology, Vol. 20, pp. 109-115, 1991.

[10] C.A. Brebbia, L.C. Wrobel, and J.C.F. Telles, *Boundary Element Techniques: Theory and Applications in Engineering*, Springer-Verlag, Berlin, 1984.

[11] G. Pucihar, T. Kotnik, B. Valič, and D. Miklavčič, "Numerical determination of transmembrane voltage induced on irregularly shaped cells", Annals of Biomed. Eng., Vol. 34, pp. 642-652, 2006.

[12] U. Zimmermann, G. Pilwat, and F. Riemann, "Dielectric breakdown of cell membranes", Biophys. J., Vol. 14, pp.881-899, 1974.

Boonchai Techaumnat (M'02) was born in Bangkok, Thailand in 1970. He received the B.Eng. in 1990, the M.Eng. degrees in 1995 from Chulalongkorn University, Thailand, and the doctoral degree in electrical engineering from Kyoto University in 2001. He joined the Faculty of Engineering, Chulalongkorn University as a lecturer in 1995. He is now an Associate Professor at the faculty. Dr. Techaumnat received the medal prize for new scholars from the Thailand Research Fund in 2005, the Nanobiotechnology Premium from the Institution of Engineering and Technology (IET) in 2009, and the book prize from the Institute of Electrical Engineers Japan in 2011 for "Electric Fields in Composite Dielectrics and their Applications". His research interests include numerical field analysis, electrical insulation, bioelectromagnetics, and particle electrokinetics.

Analysis on Electrostatic Behavior of a Conducting Prolate Spheroid under an Electric Field

Viet Quoc Huynh, Boonchai Techaumnat
Department of Electrical Engineering, Chulalongkorn University
Phyathai Road, Pathumwan, Bangkok 10330, Thailand

and **Kunihiko Hidaka**
Department of Electrical Engineering and Information Systems, University of Tokyo
7-3-1 Hongo, Bunkyo-ku, Tokyo 113-8656, Japan

ABSTRACT

This paper presents the electrostatic analysis of a conducting prolate spheroid under an external electric field in axisymmetric configurations. The configurations consist of a conducting spheroid which is in contact with or separated from a grounded plane. We apply the method of images using multipoles to the electric field calculation. The calculation uses the multipole re-expansion formulae and the equivalent image charges of a prolate conducting spheroid. The induced charge and force are determined from the multipole images. For a spheroid on the grounded plane, the calculation results show that the maximal field increases nonlinearly with the major-to-minor axis ratio of the spheroid. The charge and the force are compared between the spheroids of the same major axis or the same surface area. We propose empirical formulae for approximating the maximal field, charge and force with the errors smaller than 2% for the axis ratio between 1 and 32. We examine the propriety of the approximation of the electric field, charge and force based on a hemispheroidal model. For an uncharged spheroid separated from the grounded plane, we clarify the relationship between the separation and the field intensification at the bottom pole of the spheroid. Based on the critical field strength of a background medium, the position of the spheroid where the partial discharge takes place is estimated. For a charged spheroid, we found that the maximal electric field hardly depends on the separation from the plane.

Index Terms — **Induced charge, electrostatic force, hemispheroidal approximation, multipole re-expansion, spheroidal harmonics.**

1 INTRODUCTION

RECENTLY gas insulated systems such as gas insulated switchgears (GIS) and gas-insulated transmission lines (GITL) are widely used in the electric power systems for increasing operational reliability and safety as well as reducing space, etc. However, the insulation of the GIS and GITL can be appreciably affected by the existence of particles, which may enter the insulation systems during the process of manufacturing, assembly, or installation. In particular, conducting particles gain charge when they make contact with an electrode under an electric field. A charged particle tends to move between electrodes by the Coulomb force. The particle movement intensifies electric field significantly in its vicinity. As a result, partial discharge or breakdown may take place in the gaseous dielectric [1, 2].

The movement of a conducting particle under a nonuniform electric field in the air and SF_6 has been reported by many researchers [2-6]. Spherical and cylindrical profiles were considered for the particles. The analysis of induced charge and electrostatic force on a particle in contact with an electrode was an important ground for studying the particle movement. For example, the charge and the force on a spherical particle were analyzed by Felici [7] and by Hara and Akazaki [8]. For a wire particle, the model of an infinite conducting cylinder in contact with an electrode was used for estimating the charge and force [9]. It was found that the wire particle was in the standing position before it was lifted from an electrode [9, 10]. This is because the charge and force on the particle are greater when it stands up on an electrode than that when it lies on the electrode. Under a nonuniform electric field, a particle may move along the electrode surface to the higher-field region and then elevates from the electrode [3, 4]. The movement of a wire particle is more complicated and depends heavily on the corona discharge phenomenon at its ends [2, 5].

In practice, free particles in the gas insulated systems are of irregular profiles, not limited to the spherical or the wire

---

Manuscript received on 7 January 2013, in final form 10 June 2013.

profile. The induced charge and force for non-spherical particles have not been fully presented yet. The analytical solution does not exist in a closed form when a non-spherical particle is near or in contact with an electrode. Although numerical methods can calculate the electric field on any profiles, it is difficult to realize high accuracy due to the complexity of the particle profiles.

This paper presents an analysis of the electric field, induced charge, and electrostatic force in configurations of a non-spherical particle and a plane electrode under an external electric field. The non-spherical particle is approximated as prolate spheroidal one. This approximation is convenient for applying an analytical method and for varying the particle shapes from sphere-like to wire-like ones. The objective of this paper is to determine the effect of the particle shape on the electrostatic behavior under charged or uncharged conditions. In order to achieve high accuracy, the electric field has been analyzed by using the method of multipole images, an analytical method.

2 CONFIGURATIONS OF ANALYSIS

The configurations of analysis are shown in Figure 1. The first configuration (Figure 1a) is a conducting spheroid in contact with a grounded plane. The second one (Figure 1b) is a conducting spheroid located at distance δ above a grounded plane. The permittivity of the background medium is denoted by ε_E (= ε_0 for vacuum or a gaseous dielectric). The spheroid in Figure 1a is at a grounded potential and under a uniform electric field $\mathbf{E}_0$ in the z direction. On the other hand, we assume that the spheroid in Figure 1b is electrically floating and consider both uncharged and charged conditions.

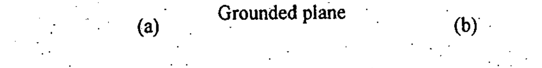

Figure 1. Conducting prolate spheroid under an external electric field: (a) in contact with a grounded plane, (b) above a grounded plane.

The minor and major semi-axes of the spheroid are denoted by b and c, respectively. The surface area S of a prolate spheroid is

$$S = 2\pi b^2 \left[1 + \frac{c}{b} \frac{\arccos(b/c)}{\sqrt{1-(b/c)^2}} \right] \tag{1}$$

The electric field on the spheroid in both configurations is independent of b and c values, provided the c/b and δ/c ratios are constant. By contrast, the net charge and electrostatic force vary proportionally to the surface area for the same axis ratio and δ/c ratio.

For presenting calculation results, we define l as the arc length measured from the top pole of the spheroid and L as the length between the top and bottom poles. The area obtained by rotating l around the z-axis is defined as S_l. Figure 2 presents the ratios S_l/S, which are independent of the spheroid size, as a function of the normalized arc length l/L for different c/b values.

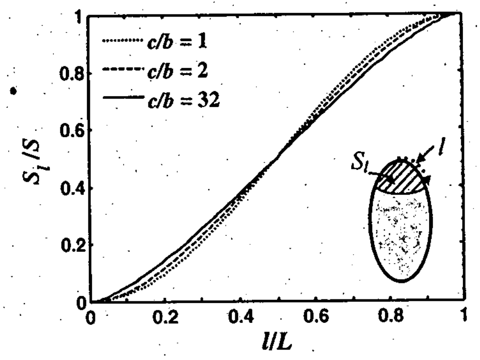

Figure 2. Ratio of surface area S_l to whole surface area S for spheroids having different c/b values.

3 CALCULATION METHOD

3.1 PROLATE SPHEROIDAL HARMONICS

The prolate spheroidal coordinates are formed by rotating elliptic coordinates about the major axis of the ellipses, as shown in Figure 3. The focal points of ellipses are located on z-axis at $\pm a$. The relationship between the prolate spheroidal coordinates (η, ξ, φ) and the Cartesian coordinates (x, y, z) is expressed as follows:

$$\begin{aligned} x &= a\sqrt{\eta^2-1}\sqrt{1-\xi^2}\cos\varphi \\ y &= a\sqrt{\eta^2-1}\sqrt{1-\xi^2}\sin\varphi \\ z &= a\eta\xi \end{aligned} \tag{2}$$

where $\eta \geq 1, -1 \leq \xi \leq 1, 0 \leq \varphi < 2\pi$. In the spheroidal coordinates, each surface of constant $\eta > 1$ corresponds to the surface of a prolate spheroid whose major semi-axis $c = a\eta$ and minor semi-axis $b = a(\eta^2 - 1)^{1/2}$. Note that $c^2 - b^2 = a^2$.

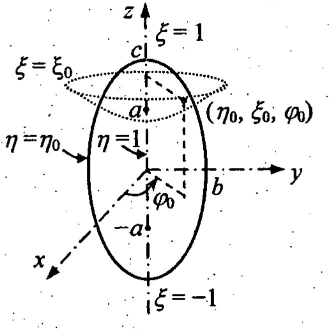

Figure 3. Prolate spheroidal coordinates.

The general solutions of the Laplace equation in the prolate spheroidal coordinates are a sum of prolate spheroidal harmonics. Due to the symmetry about the z-axis, the solutions are independent of azimuth angle φ. Let a spheroid surface be defined by $\eta = \eta_0$. We can expand the potential ϕ_{ext} produced by any charges outside the spheroid about the origin as a sum of harmonics in the form of local expansion [11],

$$\phi_{ext} = \sum_{n=0}^{\infty} L_n P_n(\eta) P_n(\xi) \tag{3}$$

where P_n is the nth-order Legendre function of the first kind, and L_n is a real-number potential coefficient. The potential ϕ_{ext} induces free charge on the spheroid surface. The induced potential ψ due to this charge can be expressed as a sum of harmonics in the form of multipole expansion,

$$\psi = \sum_{n=0}^{\infty} B_n Q_n(\eta) P_n(\xi) \tag{4}$$

where Q_n is the Legendre function of the second kind. $Q_n(\eta)$ is singular at $\eta = 1$ and approaches zero with increasing η to infinity. The coefficients B_n are determined from L_n to fulfill the boundary conditions on the spheroid surface. For example, if the surface is a grounded conducting one,

$$B_n = -\frac{P_n(\eta_0)}{Q_n(\eta_0)} L_n \quad \text{for } n \geq 0 \tag{5}$$

If the conducting spheroid has total charge Q, equation (5) holds for $n \geq 1$ and the theory in [12] is used for $n = 0$ as

$$B_0 = \frac{Q}{4\pi\varepsilon_E a}. \tag{6}$$

3.2 METHOD OF ANALYSIS

The method of multipole images for the prolate spheroidal coordinates is applied to the calculation in an iterative manner. The calculation begins with the expansion of potential ϕ_0 due to the external field $\mathbf{E}_0$ in prolate spheroidal harmonics about the center of the spheroid ($\eta = 1$ and $\xi = 0$),

$$\begin{aligned}\phi_0 &= -(c+\delta)E_0 - zE_0 \\ &= -(c+\delta)E_0 - aE_0\left[P_1(\eta)P_1(\xi)\right]\end{aligned} \tag{7}$$

where $\delta = 0$ for Figure 1a. Equation (7) means that $L_0^{(1)} = -(c+\delta)E_0$, $L_1^{(1)} = -aE_0$, and $L_n^{(1)} = 0$ for $n > 1$, where the superscript "(1)" represents the iteration step.

Next, for the grounded spheroid in Figure 1a we use equation (5) to compute $B_n^{(1)}$ (n=0, 1, ...) to satisfy the boundary condition on the spheroid surface. For the electrically-floating spheroid in Figure 1b, both equations (5) and (6) are applied.

After calculating $B_n^{(1)}$, images $B'^{(1)}_n$ are inserted below the plane to satisfy the zero potential on the grounded plane (see Figure 4). The magnitude of $B'^{(1)}_n$ is determined from $B_n^{(1)}$ as

$$B'^{(1)}_n = (-1)^{n+1} B_n^{(1)} \quad \text{for } n \geq 0 \tag{8}$$

Then, we re-expand the potential of images $B'^{(1)}_n$ about the center of the spheroid. Let η' and ξ' be the prolate spheroidal coordinates with the origin at the center of the image spheroid. A unit harmonic $\bar{\psi}_n = Q_n(\eta')P_n(\xi')$ can be re-expanded as

$$\bar{\psi}_n = Q_n(\eta')P_n(\xi') = \sum_{m=0}^{\infty} L_{m,n} P_m(\eta) P_m(\xi) \tag{9}$$

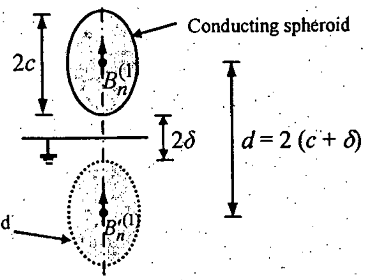

Figure 4. Image of the multipole $B_n^{(1)}$ by the grounded plane.

where $L_{m,n}$ is a re-expansion coefficient. Note that we may use the transformation between spherical and spheroidal harmonics [13] and the re-expansion of spherical harmonics [14] to determine $L_{m,n}$. However, in this paper $L_{m,n}$ in equation (9) is directly derived for the spheroidal harmonics based on the equivalent image [12] to reduce the complicated procedures. Details are given in the Appendix. By using the re-expansion formula (A7), the calculation time and the accuracy are also significantly improved in comparison with the method of direct (numerical) integration.

In the next iteration, $B_n^{(2)}$ are then calculated from $L_{m,n}$ by equations (5) and (6) to satisfy again the condition on the spheroid. The application of image schemes and the re-expansion is repeated until the solutions converge. Then, B_n and B'_n are determined as the sum of all $B_n^{(i)}$ and $B'^{(i)}_n$ to represent the induced charge on the spheroid and its image with respect to the grounded plane, respectively.

3.3 ELECTRIC FIELD, INDUCED CHARGE AND ELECTROSTATIC FORCE

From the calculation, the resultant potential ϕ outside the spheroid surface is equal to the sum of the potential ψ_B produced by the image B_n, $\psi_{B'}$ by image B'_n, and ϕ_0 by the applied field,

$$\phi = \psi_B + \psi_{B'} + \phi_0. \tag{10}$$

The expressions ψ_B and $\psi_{B'}$ are in the form of multipole expansion, as presented in equation (4). The electric field E on the spheroid surface can be numerically calculated from the potential gradient. For example, from the potential ψ in equation (4), the electric fields in the η and ξ directions are

$$E_\eta = -\frac{1}{h_\eta} \sum_{n=0}^{\infty} B_n Q'_n(\eta) P_n(\xi) \tag{11}$$

$$E_\xi = -\frac{1}{h_\xi} \sum_{n=0}^{\infty} B_n Q_n(\eta) P'_n(\xi) \tag{12}$$

where $Q'_n(\eta)$ and $P'_n(\xi)$ are the derivatives of the corresponding Legendre functions, h_η and h_ξ are the scale factors of the spheroidal coordinates [11].

The total charge Q and force F can be determined directly from the multipole images. Q is related to B_0 by equation (6). The electrostatic force is calculated from the interaction between electric field and the multipoles in spherical coordinates [15]. For a jth-order spherical multipole B_j^{sph} under the potential

$$\phi^{sph} = \sum_j L_j^{sph} r^n P_j(\cos\theta) \tag{13}$$

where L_j^{sph} is potential coefficient, the force F is in the z direction, and referring to [15]

$$F = -4\pi\varepsilon_E \sum_{j=0}^{\infty} (j+1) B_j^{sph} L_{j+1}^{sph} \tag{14}$$

To apply equation (14), the calculated spheroidal multipoles B_n are transformed into spherical multipole B_j^{sph} as explained in [11],

$$B_j^{sph} = \frac{a^{j+1}}{2} \sum_{n=0}^{\infty} I_{n,j} B_n \, , \tag{15}$$

where I_{nj} is defined in the Appendix.

The external potential ϕ^{sph} in equation (13) is the sum of ϕ_0 and $\psi_{B'}$. It is obtained by transforming multipoles B'_n to B'^{sph}_n by using equation (15) and re-expanding their potentials about the spheroid center in the form of local expansion [14].

The calculation results in this paper are obtained by using the highest order $N = 200$ for the harmonics. We have confirmed that the maximum electric field changes only slightly (<0.004%) even when increasing N to 500 for the calculation. As the Laplace equation is satisfied by spheroidal harmonics, we have verified calculation results by comparing the calculated potential with the boundary conditions on the spheroid surface and the grounded plane. With $c/b \to 1$, the results also converge well to the analytical solutions for the case of a conducting sphere in corresponding configurations [7, 8].

4 RESULTS AND DISCUSSION

4.1 SPHEROID IN CONTACT WITH THE PLANE

4.1.1 ELECTRIC FIELD

Figure 5 shows the distribution of electric field along the spheroid surface for c/b = 1, 2, and 4. In the figure, the electric field is maximal at the top pole (l/L = 0) and zero at the bottom pole (l/L = 1). Since the field is very high on the upper half of the spheroid, almost all of the induced charge and electrostatic force on the spheroid are distributed on the upper half. Figure 6 shows the variation of the maximal field E_{max} for c/b = 1 to 32. The maximal field is significantly intensified with increasing c/b.

The following empirical formula, obtained by curve fitting, may be used for estimating the maximal filed magnitude:

$$\frac{E_{max}}{E_0} = 1.37\left(0.92 + \frac{c}{b}\right)^{\sqrt{3}} \tag{16}$$

This expression has a similar form to the approximation of the electric field at the contact point of an uncharged conducting spheroid on a solid dielectric, which is proposed by one of the authors [16]. The estimation by equation (16) is presented by the symbols in Figure 6. Table 1 shows the error of the estimated values in comparison with the maximal field by the calculation results. It can be seen from Table 1 that the error is smaller than 1% for the c/b ratio up to 32.

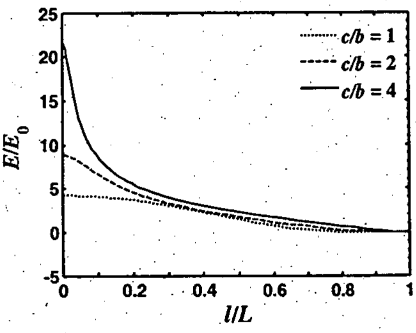

Figure 5. Distribution of electric field along the spheroid surface.

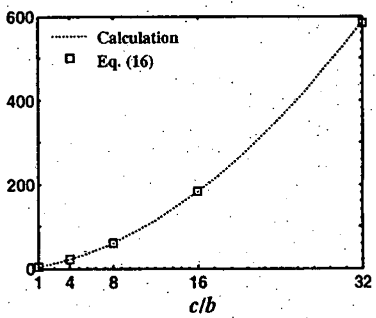

Figure 6. Maximal field as a function of the axis ratio c/b.

Table 1. Comparison of the maximal field with the approximation by equation (16).

c/b	E_{max}/E_0		Error
	Calculation	Equation (16)	(%)
1	4.21	4.24	0.71
4	21.7	21.6	0.46
8	60.4	60.6	0.33
16	183	184	0.55
32	587	582	0.85

4.1.2 INDUCED CHARGE AND ELECTROSTATIC FORCE

Figures 7a and 7b present the charge Q_l and force F_l on the surface S_l (mentioned in Figure 2) as a function of l/L. Q_l and F_l are calculated by using numerical quadratures, and normalized by the total charge Q and total force F on the whole spheroid, respectively. As shown in Figure 7a, about 80% of the net induced charge resides on the upper half of the sphere and spheroid, for example, 77% for c/b = 32. For higher c/b, a higher portion of the induced charge is located around the top pole. It is clear from Figure 7b that the force on the lower half is negligible for all cases of c/b. For high c/b, the force in the vicinity of the top pole becomes predominant. For instance, 90% of the total force acts on 5% surface area around the top pole (at $l/L \approx 0.1$, see Figure 2) when c/b = 32.

The net charge Q and force F on a spheroid depend on its surface area. We examine the effect of the spheroid shape by varying the c/b ratio, and compare Q and F between spheroids of the same major semi-axis $c = c_0$ (Figure 8a) or between those of the same surface area S (Figure 8b). The latter case means that the spheroid is slender and longer with increasing c/b. We normalize the charge and force by $Q_0 = \varepsilon_E S_0 E_0$ and $F_0 = \varepsilon_E S_0 E_0^2$ in Figure 8a, where $S_0 = 4\pi c_0^2$, and by $Q_1 = \varepsilon_E S E_0$ and $F_1 = \varepsilon_E S E_0^2$ in Figure 8b.

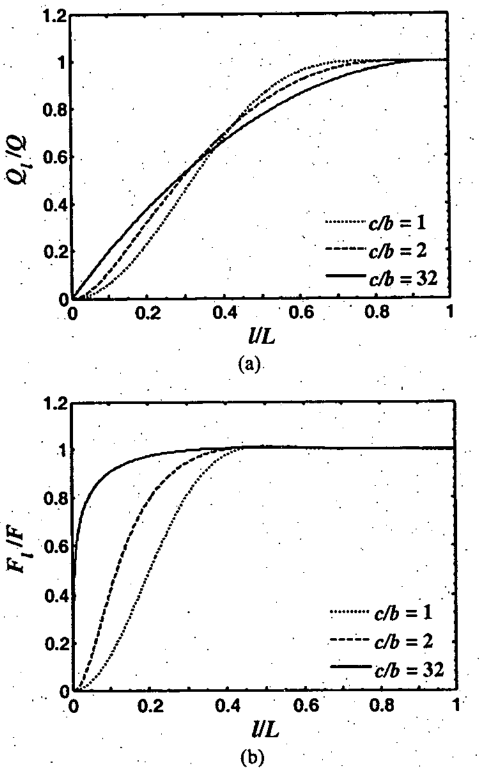

Figure 7. Induced charge (a) and electrostatic force (b) on the surface area S_l as functions of l/L.

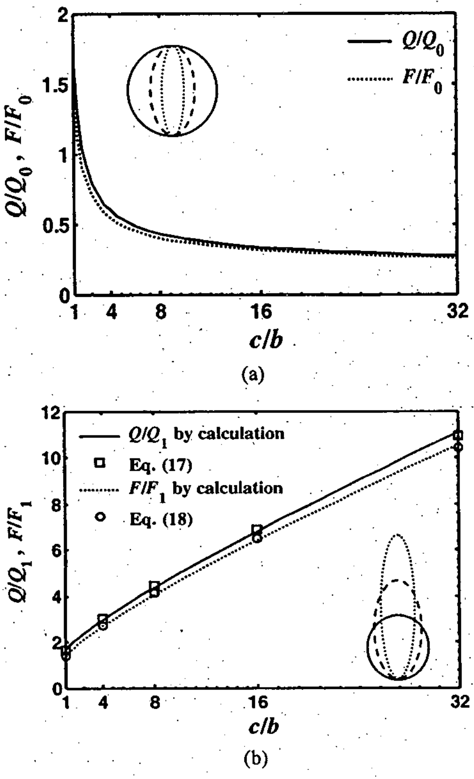

Figure 8. Total charge Q and force F on the spheroids having the same (a) major axis and (b) surface area as functions of c/b.

Figures 8a shows that for the same major axis, the charge and force decrease with increasing c/b. The decreasing rates are remarkable for $c/b \leq 4$. For example, the charge and force decrease by about 60% when c/b increases from 1 to 4. In Figure 8b, the calculation results of the normalized Q and F having the same surface area are presented by the curves as a function of c/b ratio. We can see from Figure 8b that for the same surface area, the charge and force increase with c/b. When c/b increases from 1 to 8, the charge and force increase by about two times, respectively. It is worth noting that the characteristics of the normalized charge and force are very similar to each other.

Based on the calculation results, the following empirical formulae are proposed to evaluate the normalizing factors of the total charge and force on a spheroid in range c/b = 1 to 32:

$$\frac{Q}{Q_1} = 0.917\left(1.33+\frac{c}{b}\right)^{\frac{1}{\sqrt{2}}}, \tag{17}$$

$$\frac{F}{F_1} = 0.88\left(0.92+\frac{c}{b}\right)^{\frac{1}{\sqrt{2}}}. \tag{18}$$

The approximated charge and force values by equations (17) and (18) are presented by symbols in Figure 8b. Table 2 shows the errors of the approximated charge and force with our calculation results. We can see from the table that the error by the approximation is smaller than 2% for the considered range of c/b.

Table 2. Errors of the induced charge and force by the approximation in equation (17) and equation (18).

c/b	Q/Q_1		F/F_1	
	Calculation	Error (%) by Eq. (17)	Calculation	Error (%) by Eq. (18)
1	1.65	1.09	1.37	1.90
4	2.98	0.47	2.71	0.18
8	4.38	1.55	4.06	1.85
16	6.81	1.20	6.42	1.25
32	11.1	1.41	10.6	1.78

4.1.3 HEMISPHEROID APPROXIMATION

The force on a prolate hemispheroid standing on a grounded plane under an external electric field is studied analytically and numerically [17]. The exact solution of the charge for the hemispheroid was also presented and compared with an approximate formula [18]. This section compares our calculation results with those approximated by using a hemispheroid model. The hemispheroidal model is presented in Figure 9, where the major semi-axis is $2c$. We consider two cases of the minor semi-axis b_H, i.e. $b_H = b$ and $2b$. We expect that the former model works for slender spheroids because the results in the previous section show that the electric field is very small on the lower-half surface of these spheroids.

The difference of the maximal electric field by the approximation is given in Figure 10. For $b_H = b$, the approximation is always greater than the actual values. The difference is larger than 37% for $c/b = 1$ and increases with c/b. On the other hand, for $b_H = 2b$, the approximation is always smaller than the actual values. The difference is between 20% and 40% for the range of c/b. Therefore, neither case of b_H is appropriate for evaluating of the maximal field.

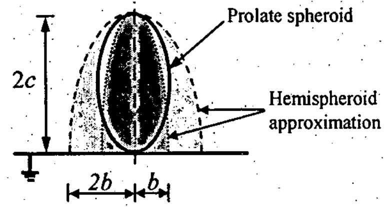

Figure 9. Hemispheroidal approximation for a prolate spheroid.

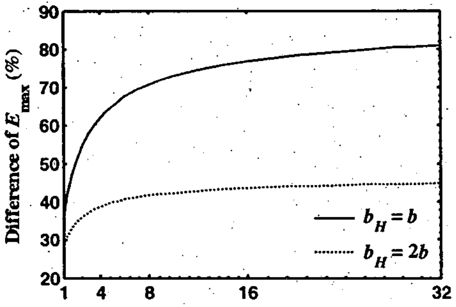

Figure 10. Difference of E_{max} by the hemispheroidal approximation in comparison with the results by the multipole image method.

Figure 11 presents the differences of Q and F by the hemispheroid approximation when $b_H = b$. The differences are smaller than 15% for $c/b = 1$ and decrease with c/b. This approximation can estimate Q and F with a difference smaller than 10% for $c/b > 3$. The charge and force by the approximation are smaller than our calculation results. With increasing c/b, the difference of E_{max} increases in Figure 10; however, the region of high electric field is more restricted. Therefore, the difference of Q and F becomes smaller with increasing c/b in Figure 11. Note that the comparison when $b_H = 2b$ is not presented here because the differences of Q and F are much larger than those when $b_H = b$.

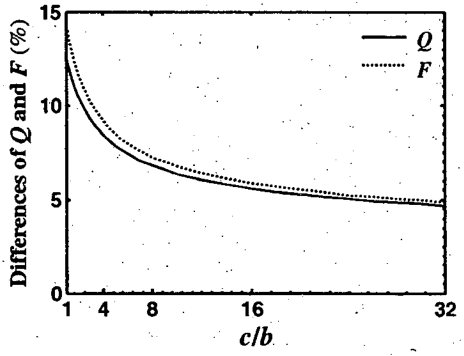

Figure 11. Differences of Q and F by hemispheroidal approximation when $b_H = b$ in comparison with the results by the multipole image method.

4.2 UNCHARGED SPHEROID ABOVE THE PLANE

In this section we consider a spheroid located above the grounded plane by distance or separation δ (Figure 1b). The spheroid is assumed to be uncharged. Under an external field, a potential difference exists between the spheroid and the grounded plane. With decreasing δ, the electric field can be highly intensified at the bottom pole of the spheroid.

4.2.1 ELECTRIC FIELD

Figure 12 presents the distribution of electric field along the spheroid surface for different axis ratios c/b when $\delta/c = 0.1$. The positive field magnitude is referred to the direction outward from the spheroid. It is clear from the figure that the electric field is stronger for higher c/b. The field enhances significantly at the two poles. The field maximum is always at the bottom pole ($l/L = 1$). Figure 13 presents the maximal field magnitude E_{max} at the bottom pole as a function of the normalized distance δ/c from 0.01 to 10. The figure indicates that the maximal field increases siginificantly with decreasing δ/c from 0.1 to 0.01.

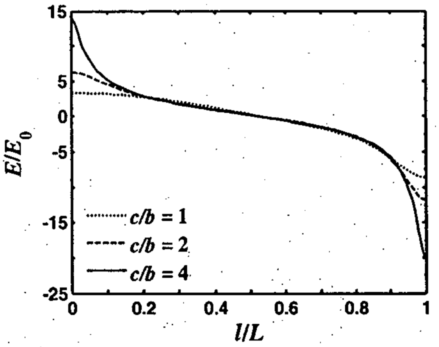

Figure 12. Distribution of electric field along the spheroid surface for different c/b ratios when $\delta/c = 0.1$.

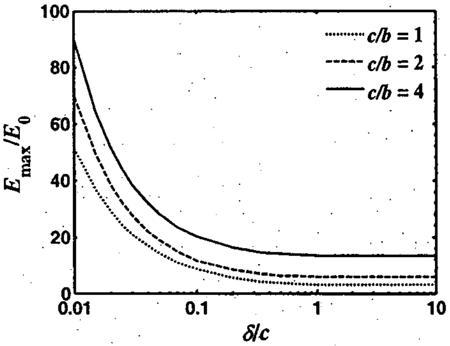

Figure 13. Magnitude of maximal electric field at the bottom pole as a function of δ/c.

4.2.2 CRITICAL SEPARATION

As mentioned in the previous section, the electric field at the bottom pole of the spheroid is enhanced significantly on an uncharged spheroid located near the grounded plane. This may result in the partial discharge inception near the bottom pole. For the case of a sphere, the discharge threshold in the gap was estimated by using the Paschen curve for a uniform field [19]. For the spheroid, due to the field nonuniformity in the gap, the application of the Paschen curve may be inappropriate. For approximation, we compare the maximum field E_{max} on the spheroid with the critical field stress E_c of a medium to observe the variation of the critical separation δ_c of the partial discharge onset. This estimation is applied to different axis ratio c/b values.

As an example, $E_c = 30$ kV/cm is used for the atmospheric air. Figure 14 presents the relationships of the critical separation δ_c for the partial discharge onset and the external field E_0, varied from 0.1 kV/cm to 10 kV/cm, for $c/b = 1, 2, 4$, and 8. Needless to say that with decreasing E_0, δ_c becomes smaller. For $\delta_c/c > 1$, the influence of the plane is negligible; hence, the external field E_0 for the partial discharge hardly depends on δ_c. For smaller δ_c/c ratio, the relationships in Figure 14 become approximately linear in the logarithmic scale. That is,

$$\frac{\delta_c}{c} \propto E_0^k \tag{19}$$

where $k = 1.16$, 1.19, 1.21, and 1.59 for $c/b = 1$, 2, 4 and 8, respectively. For other background medium, we can modify Figure 14 for other medium by scaling the abscissa with the ratio of the critical field strength E_c corresponding to the medium. For example, E_0 in the figure is scaled by 9 times when the medium is SF_6 at 0.3 MPa whose E_c is about 270 kV/cm. Note that the estimation based on E_c does not consider the physical discharge mechanisms. For a very small gap, the microdischarge process may play an important role on the determination of the discharge onset [20].

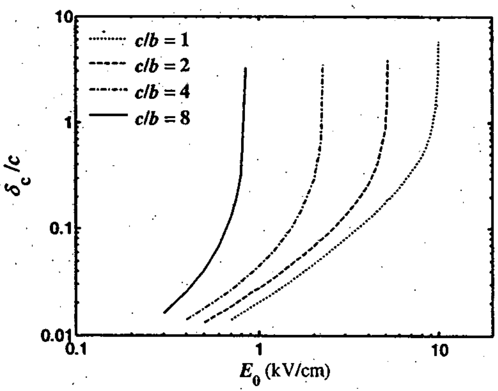

Figure 14. Relationship between the critical separation for the partial discharge onset and the external field for different axis ratios.

4.3 CHARGED SPHEROID ABOVE THE PLANE

This section considers the spheroid in the configuration of Figure 1b for the case in which the spheroid is charged, maybe by the contact treated in section 4.1 or by the discharge explained in section 4.2. At a separation δ value, the field and the force vary with the charge on the spheroid. We assume that the spheroid is fully charged to amount Q, the total induced charge of the spheroid in contact with the grounded plane. The value of Q varies with the axis ratio, as already presented in Figure 8.

As an example, Figure 15 presents the electric field distribution along the spheroid surface of axis ratio $c/b = 2$ for different δ/c values. It is clear from Figure 15 that the field magnitude near the bottom pole increases with increasing δ. This increase reflects the redistribution of charges to the area. However, the electric field hardly changes with δ on the upper half. The maximum field is at the top pole, similarly to the case of the grounded spheroid in section 4.1.1, as the electric field direction due to charge Q is in the same with E_0 at the top pole but the opposite direction with E_0 at the bottom pole.

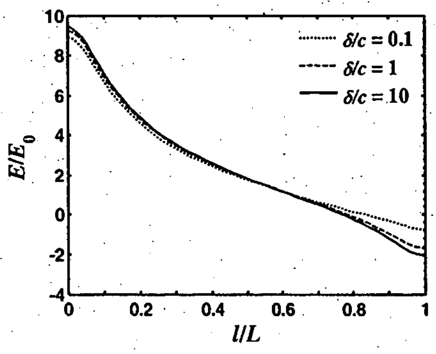

Figure 15. Electric field distribution on the fully charged spheroid for c/b=2.

Figure 16 shows the electrostatic force exerted on the spheroid for the variation of δ/c from 0.01 to 10. The force is normalized by the product QE_0. The figure implies that the normalized force increases with δ/c and is greater for higher c/b. The force converges well to QE_0 when $\delta/c \geq 10$.

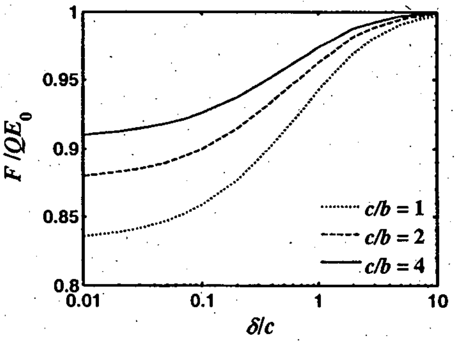

Figure 16. Force on the fully charged spheroid as a function of δ/c.

CONCLUSION

This paper applies the multipole image method to the analysis on electrostatic behavior of a conducting spheroid in axisymmetric configurations. The effects of the axis ratio c/b on the electric field, charge, and force have been clarified. The hemispheroidal approximation is found to be appropriate for estimating the charge and force on the grounded spheroid, especially when c/b is high. For the configuration of the uncharged spheroid above the grounded plane, the maximum field at the bottom pole increases significantly with decreasing δ/c, especially for δ/c smaller than 0.1. The relationship between the critical separation and the background field is investigated. For the fully charged spheroid above the grounded plane, the maximal field hardly varies with the separation from the plane.

ACKNOWLEDGMENTS

This work was supported by the AUN/SEED-Net program, JICA and the Thailand Research Fund. B.T. also thanks Prof. Tadasu Takuma of Tokyo Denki University, for the discussion on this work.

APPENDIX

Consider an *n*th-order unit harmonic

$$\psi_n(\mathbf{r}') = Q_n(\eta')P_n(\xi') \qquad \text{(A1)}$$

expanded in the coordinates (x', y', z'), where the position vector is denoted as $\mathbf{r}'$. The image charge representing $\psi_n(\mathbf{r}')$ is a line charge at $\eta' = 1$ having charge density $2\pi\varepsilon_E P_n(\xi')$ [12]. Thus, the harmonic may be written as an integral of the image line charge on the line $\eta' = 1$,

$$\psi_n(\mathbf{r}') = \frac{a}{2}\int_{-1}^{1} P_n(\xi'_s)\frac{1}{\|\mathbf{r}' - \mathbf{z}'_s\|}d\xi'_s, \qquad \text{(A2)}$$

where $\mathbf{z}'_s$ is the position vector of the charge ($\eta' = 1$, $\xi' = \xi'_s$) on the image line.

We want to re-expand $\psi_n(\mathbf{r}')$ about the origin of the coordinates (x, y, z), which is at distance d above the original origin ($x' = 0$, $y' = 0$, $z' = 0$), as shown in Figure 17, in the following form:

$$\psi_n(\mathbf{r}') = \sum_{m=0}^{\infty} L_{m,n}P_m(\eta)P_m(\xi). \qquad \text{(A3)}$$

where $L_{m,n}$ is the coefficient of re-expansion.

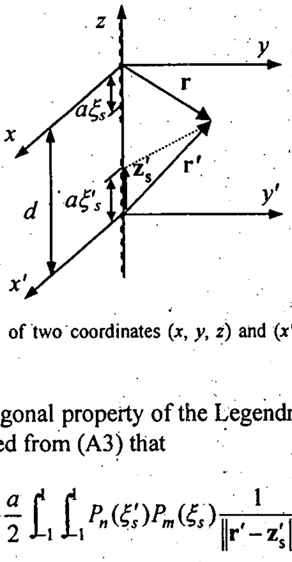

Figure 17. Origins of two coordinates (x, y, z) and (x', y', z') separated by distance *d*.

Using the orthogonal property of the Legendre polynomials, it can be concluded from (A3) that

$$L_{m,n} = \frac{2m+1}{2}\frac{a}{2}\int_{-1}^{1}\int_{-1}^{1} P_n(\xi'_s)P_m(\xi_s)\frac{1}{\|\mathbf{r}' - \mathbf{z}'_s\|}d\xi'_s d\xi_s \qquad \text{(A4)}$$

In equation (A4), $\|\mathbf{r}' - \mathbf{z}'_s\|$ is the vertical distance along the axis. Hence,

$$\frac{1}{\|\mathbf{r}' - \mathbf{z}'_s\|} = \frac{1}{d + a\xi_s - a\xi'_s} = \frac{1}{a}\left(\frac{1}{\eta_0 + \xi_s - \xi'_s}\right), \qquad \text{(A5)}$$

where $\eta_0 = d/a$. By expanding equation (A5) in term of (ξ_s, ξ'_s) about $(\xi_s = 0, \xi'_s = 0)$, we obtain

$$\frac{1}{\|\mathbf{r}' - \mathbf{z}'_s\|} = \frac{1}{a}\left(\sum_{j=0}^{\infty}\sum_{k=0}^{\infty}\frac{(-1)^j}{\eta_0^{j+k+1}}\frac{(j+k)!}{j!k!}\xi_s^j\xi_s'^k\right). \qquad \text{(A6)}$$

Substituting equation (A6) into equation (A4), we can obtain the re-expansion coefficient as a sum,

$$L_{m,n} = \frac{2m+1}{4}\sum_{j=0}^{\infty}\sum_{k=0}^{\infty}\frac{(-1)^j}{(d/a)^{j+k+1}}\frac{(j+k)!}{j!k!}I_{m,j}I_{n,k}, \qquad \text{(A7)}$$

where

$$I_{n,k} = \int_{-1}^{1}\xi^k P_n(\xi)d\xi. \qquad \text{(A8)}$$

$I_{n,k}$ is nonzero if $n + k$ is even and $k \geq n$:

$$I_{n,k} = \frac{2k!}{(k-n)!!(k+n+1)!!}. \qquad \text{(A9)}$$

REFERENCES

[1] M. M. Morcos, S. A. Ward, H. Anis, K. D. Srivastava and S. M. Gubanski, "Insulation integrity of GIS/GITL systems and management of particle contamination", IEEE Electr. Insul. Mag., Vol. 16, No. 5, pp. 25-37, 2000.

[2] K. Sakai, D. L. Abella, Y. Khan, J. Suehiro and M. Hara, "Experimental studies of free conducting wire particle behavior between non-parallel plane electrodes with ac voltages in air", IEEE Trans. Dielectr. Electr. Insul., Vol. 10, No. 3, pp. 418-424, 2003.

[3] K. Sakai, S. Tsuru, D. L. Abella and M. Hara, "Conducting particle motion and particle-initiated breakdown in dc electric field between diverging conducting plates in atmospheric air", IEEE Trans. Dielectr. Electr. Insul., Vol. 6, No. 1, pp. 122-130, 1999.

[4] K. Sakai, D. L. Abella, Y. Khan, J. Suehiro and M. Hara, "Theoretical and experimental studies for spherical free-conducting particle behavior between non-parallel plane electrodes with ac voltages in air", IEEE Trans. Dielectr. Electr. Insul., Vol. 10, No. 3, pp. 404-417, 2003.

[5] Y. Khan, K. Sakai, E. Lee, J. Suehiro and M. Hara, "Motion behavior and deactivation method of free-conducting particle around spacer between diverging conducting plates under dc voltage in atmospheric air", IEEE Trans. Dielectr. Electr. Insul., Vol. 10, No. 3, pp. 444-457, 2003.

[6] M. M. Morcos, S. Zhang, K. D. Srivastava and S. M. Gubanski, "Dynamics of metallic particle contaminants in GIS with dielectric-coated electrodes", IEEE Trans. Power Delivery, Vol. 15, No. 2, pp. 455-460, 2000.

[7] N. J. Félici, "Forces et charges de petits objets en contact avec une électrode affectée d'un champ électrique", Rev. Gén. Electric, Vol. 75, No. 10, pp. 1145-1160, 1966.

[8] M. Hara and M. Akazaki, "A method for prediction of gaseous discharge threshold voltage in the presence of a conducting particle", J. Electrost., Vol. 2, No. 3, pp. 223-239, 1977.

[9] Y. Khan, A. Oda, S. Okabe, J. Suehiro and M. Hara, "Wire particle motion behavior and breakdown characteristics around different shaped spacers within diverging air gap", IEEJ Trans. PE., Vol. 123, No. 11, pp. 1288-1295, 2003.

[10] K. Asano, K. Anno and Y. Higashiyama, "The behavior of charged conducting particles in electric fields", IEEE Trans. Ind. Appl., Vol. 33, No. 3, pp. 679-686, 1997.

[11] W. R. Smythe, *Static and dynamic electricity*, 2nd ed., McGRAW-HILL, New York, Ch. 5, 1950.

[12] B. Techaumnat and M. Washizu, "Equivalent image charges of a prolate spheroid under an external field", J. Electrost., Vol. 69, No. 4, pp. 388-393, 2011.

[13] N. Harfield, "Conductivity calculation for a two-phase composite with spheroidal inclusions", J. Phys. D: Appl. Phys., Vol. 32. No. 10, pp. 1104-1113, 1999.

[14] M. Washizu and T. B. Jones, "Dielectrophoretic interaction of two spherical particles calculated by equivalent multipole-moment method", IEEE Trans. Ind. Appl., Vol. 32, No. 2, pp. 233-242, 1996.

[15] T. B. Jones, *Electromechanics of particles*, Cambridge University Press, pp. 222-226, 1995.

[16] B. Techaumnat and T. Takuma, "Electric field and force on a conducting sphere in contact with a dielectric solid", J. Electrostat., Vol. 64, p. 165-175, 2006.

[17] K. Zhou and S. Boggs, "Derivation of exact and approximate formulas for the force on a conducting particle standing on a ground plane, and comparison with finite element computations", IEEE Trans. Dielectr. Electr. Insul., Vol. 17, No. 5, pp. 1602-1604, 2010.

[18] K. Zhou and S. Boggs, "Uniform field charge on a conducting particle", IEEE Trans. Dielectr. Electr. Insul., Vol. 16, No. 4, pp. 1158-1159, 2009.

[19] M. Hara and M. Akazaki, "Analysis of microdischarge threshold conditions between a conducting sphere and plane", J. Electrost., Vol. 13, No. 2, pp. 105-118, 1982.

[20] T. Ono, D. Y. Sim and M. Esashi, "Micro-discharge and electric breakdown in a micro-gap", J. Micromechanics and Microengineering, Vol. 10, No. 3, pp. 445-451, 2000.

Viet Quoc Huynh was born in Ben Tre, Vietnam in 1985. He received the B.Sc. degree from Ho Chi Minh city University of Technology, Vietnam in 2008, and the M.Sc. degree from Chulalongkorn University, Thailand in 2011. He is now a doctoral student at Faculty of Engineering of the Chulalongkorn University. His research interest is the analysis of electric field in high voltage engineering.

Boonchai Techaumnat (M'02) was born in Bangkok, Thailand in 1970. He received the B. Eng. in 1990, M.Eng. degrees in 1995 from Chulalongkorn University, Thailand, and the doctoral degree in electrical engineering from Kyoto University in 2001. He joined the Faculty of Engineering, Chulalongkorn University as a lecturer in 1995. He is now an Associate Professor at the faculty. Dr. Techaumnat received the medal prize for new scholars from the Thailand Research Fund in 2005, the Nanobiotechnology Premium from the Institution of Engineering and Technology (IET) in 2009, and the book prize from the Institute of Electrical Engineers Japan in 2011 for "Electric Fields in Composite Dielectrics and their Applications". His research interests include numerical field analysis, electrical insulation, bioelectromagnetics, and particle electrokinetics.

Kunihiko Hidaka received the B.E., M.E., and D.Eng. degrees from the University of Tokyo in 1976, 1978, and 1981 respectively. Since 1987 he has been with the Department of electrical engineering of the University of Tokyo and is now a professor of electrical engineering. He has been engaged in the development of electric field sensors, research on electrical breakdown phenomena concerned with high voltage technology, and has specialized in computer simulation of high-voltage structures. His work has won premiums and awards from both the Japanese and British IEE and the Institute of Electrostatics Japan. He is Fellow of IEEE and IEEJ. He is now acting as President-Elect of IEEJ.

Three-Dimensional Electromechanical Analysis of a Conducting Prolate Spheroid on a Grounded Plane

Boonchai Techaumnat, Viet Quoc Huynh
Department of Electrical Engineering, Chulalongkorn University
Phyathai road, Pathumwan, Bangkok 10330, Thailand

and **Kunihiko Hidaka**
Department of Electrical Engineering and Information Systems, University of Tokyo
7-3-1 Hongo, Bunkyo-ku, Tokyo 113-8656, Japan

ABSTRACT

This paper presents a 3D analysis of the electromechanics for a conducting prolate spheroid on a grounded plane under electric field. The objective of the analysis is to clarify the roles of tilt angle α between the particle and the plane on the electrostatic force and torque on the spheroid, which are the fundamentals of particle behavior in various applications. The method of multipole images and multipole re-expansion for the prolate spheroidal coordinates are applied to electric field calculation. The electrostatic force and torque on the spheroid are then determined. The calculation results show that the maximal field takes place at or near the higher pole of the spheroid for nonzero tilt angles. The electrostatic force is minimal and maximal when the spheroid lies and stands on the plane, respectively. We present empirical formulae for estimating the minimal and maximal force with error smaller than 1% for the major-to-minor axis ratio between 1 and 10. The electrostatic torque is in the increasing α direction, and it is magnified with increasing α from 0 to about 45°, and then reduces to zero at $\alpha = 90°$. The torque variation may be estimated by a quadratic relationship. When the gravitational force of the particle is taken into account, the electromechanical behavior can be classified into three regimes, depending on the externally applied field and the tilt angle. The presence of the electrostatic torque enhances the probability of a spheroid particle to be lifted from the grounded plane by the electric field.

Index Terms - **Electromechanical effects, electrostatic force, electric fields, prolate spheroid, multipole re-expansion, spheroidal harmonics.**

1 INTRODUCTION

MOST of failures in gas insulated systems are caused by foreign conducting particles [1]. The particles are unavoidable. They possibly enter the insulation system during the processes of manufacturing, assembly, or installation. Most of the particles found in the actual systems are smaller than 0.5 mm; however, particles longer than 2 mm were also collected [2]. A conducting particle gains charges when it makes a contact with an electrode. The charged particle tends to move between electrodes by the Coulomb force. Conducting particles intensify electric field significantly in their vicinity, as generally explained for composite dielectric systems in Ref. [3]. Therefore, they may cause corona discharge or complete breakdown in the gaseous dielectric [4, 5].

Although the behavior of a conducting particle under uniform electric is highly important in the field of electrostatics (e.g., particles in gas insulation systems), configurations in which the particle makes a tilt angle with the plane is hardly investigated. For studying the movement of conducting particles, the configuration of a conducting particle in contact with an electrode was examined as an important ground [5-9]. Spherical and cylindrical profiles were often considered for the particles. For a spherical particle, the charge and the Coulomb force were analyzed by Felici [10] and by Hara and Akazaki [11]. Experimental results on lifting field of spherical particles agreed well with the analytical ones under dc voltage [8]. In addition to Coulomb force, spherical particles may move along an electrode surface toward the higher-field region by the electrical gradient force and then elevate from the electrode [12]. The electrical gradient force can be utilized to activate and deactivate particle motion [13]. For a wire particle, the models of an infinite cylinder and a hemispheroid in contact with an electrode were applied to estimate the charge and force in the lying and standing positions [10], respectively.

Manuscript received on 29 August 2013, accepted 7 October 2013.

DOI 10.1109/TDEI.2013.004294

In practice, free particles in gas insulated systems have a variety of geometrical profiles not limited to the spherical or wire profile. However, the behavior of a non-spherical conducting particle under electric field in the systems is still unclear. The authors have reported an analysis of the electric field and force for axisymmetric configurations of a spheroid [14]. However, the behavior becomes more complicated, when a particle makes a tilt angle with an electrode possibly by electrostatic torque, mechanical operation or disturbance of the system. Although numerical methods may be used to calculate the electric field, the force, and torque on the particles, it is difficult to realize high accuracy for the 3D calculation of curved particle profiles.

This paper presents a 3D analysis of the electric field and electromechanical behavior of a conducting prolate spheroid on a grounded plane under an external electric field. The spheroidal profile is adopted here for varying the particle shapes from sphere-like to wire-like ones. The method of multipole images [15, 16] is used for the accurate field analysis. The objective of the current work is to clarify the fundamental electromechanical behavior in general 3D conditions including the effects of electrostatic torque on the spheroid.

2 CONFIGURATION OF ANALYSIS

Figure 1 shows the configuration of analysis, in which a conducting prolate spheroid centered at **o** is in contact with a grounded plane at point **p** under external electric field $\mathbf{E}_0$. The spheroid has minor semi-axis b and major semi-axis c. The major axis makes tilt angle α with the grounded plane. The permittivity of the surrounding medium is denoted by ε_E (= ε_0 for vacuum or a gaseous dielectric). We consider the range of the axis ratio c/b between 1 and 10. The surface area S and the volume V of the spheroid are determined by [17]

$$S = 2\pi b^2\left[1+\frac{c}{b}\frac{\arccos(b/c)}{\sqrt{1-(b/c)^2}}\right] \tag{1}$$

$$V = \frac{4}{3}\pi c b^2 \tag{2}$$

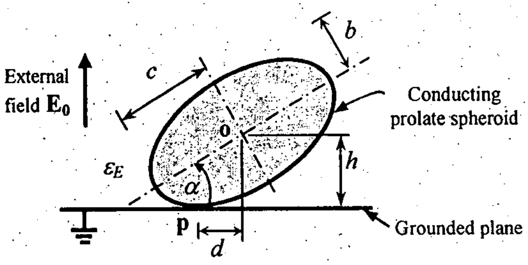

Figure 1. Conducting prolate spheroid making tilt angle α with a grounded plane under external electric field $\mathbf{E}_0$.

The horizontal distance d and vertical distance h between the contact point **p** and the center **o** are functions of b, c, and α as follows:

$$d = \frac{(c^2-b^2)\sin\alpha}{\sqrt{b^2+c^2\tan^2\alpha}} \tag{3}$$

$$h = \sqrt{b^2+c^2\tan^2\alpha}\cos\alpha \tag{4}$$

Two Cartesian coordinates having the origin at **o** shown in Figure 2a are used for the calculation. First, (X, Y, Z) are the global coordinates where the external field is in the +Z direction. Second, (x, y, z) are the local coordinates in which the major axis of the spheroid lies on the z axis. Coordinates (x, y, z) are obtained by rotating (X, Y, Z) about the Y (or y) axis by 90°−α. That is,

$$\begin{bmatrix} X \\ Y \\ Z \end{bmatrix} = \begin{bmatrix} \sin\alpha & 0 & \cos\alpha \\ 0 & 1 & 0 \\ -\cos\alpha & 0 & \sin\alpha \end{bmatrix}\begin{bmatrix} x \\ y \\ z \end{bmatrix} \tag{5}$$

Prolate spheroidal coordinates (η, ξ, φ) [18] are applied to (x, y, z) as shown in Figure 2b. The focal points of the spheroid are located on the z axis at $z = \pm a$, where $a^2 = c^2 - b^2$. The relationships between (x, y, z) and (η, ξ, φ) are

$$\begin{aligned} x &= a\sqrt{\eta^2-1}\sqrt{1-\xi^2}\cos\varphi \\ y &= a\sqrt{\eta^2-1}\sqrt{1-\xi^2}\sin\varphi \\ z &= a\eta\xi \end{aligned} \tag{6}$$

where $\eta \geq 1$, $-1 \leq \xi \leq 1$, $0 \leq \varphi < 2\pi$. In the spheroidal coordinates, the spheroid surface is presented by the surface $\eta = \eta_0 (=c/a)$, as shown in Figure 2b.

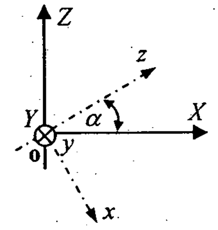

(a) Cartesian coordinates

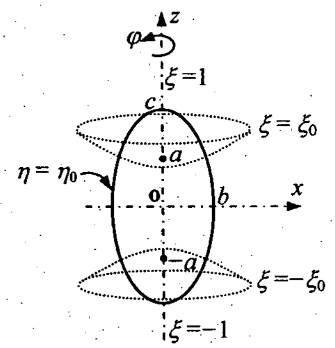

(b) Prolate spheroidal coordinates

Figure 2. Coordinates used for the calculation.

3 METHOD OF ANALYSIS

3.1 POTENTIAL HARMONICS

We apply the method of multipole images in the prolate spheroidal coordinates to the electric field calculation in an iterative manner [16]. General harmonic solutions to the Laplace equation in the prolate spheroidal coordinates are a sum of prolate spheroidal harmonics. For a spheroid whose surface is defined by $\eta = \eta_0$, we can express potential ψ_{ext} produced by any charges outside the spheroid as

$$\psi_{ext} = \sum_{n=0}^{\infty}\sum_{m=0}^{n} P_{n,m}(\eta)P_{n,m}(\xi)\left[L^c_{n,m}\cos m\varphi + L^s_{n,m}\sin m\varphi\right] \quad (7)$$

where $P_{n,m}$ is the associated Legendre function of the first kind of order n and degree m. $L^c{}_{n,m}$ and $L^s{}_{n,m}$ are real-number potential coefficients. The potential ψ_{ext} induces charges on the spheroid surface. The induced potential ψ_{ind} due to these charges can be expressed as a sum of multipole harmonics,

$$\psi_{ind} = \sum_{n=0}^{\infty}\sum_{m=0}^{n} Q_{n,m}(\eta)P_{n,m}(\xi)\left[B^c_{n,m}\cos m\varphi + B^s_{n,m}\sin m\varphi\right] \quad (8)$$

where $Q_{n,m}$ is the associated Legendre function of the second kind of order n and degree m. Note that $Q_{n,m}(\eta)$ vanishes as $\eta \rightarrow \infty$. Therefore, the resultant potential in the exterior of the spheroid ($\eta \geq \eta_0$) is

$$\psi = \psi_{ext} + \psi_{ind} \quad (9)$$

For Figure 1, the field is symmetric with respect to the plane $\varphi = 0°$. Hence, all $L^s{}_{n,m}$ and $B^s{}_{n,m}$ are zero, and we may simplify the potential expression as

$$\psi_{ext} = \sum_{n,m} L_{n,m}P_{n,m}(\eta)P_{n,m}(\xi)\cos m\varphi \quad (10)$$

$$\psi_{ind} = \sum_{n,m} B_{n,m}Q_{n,m}(\eta)P_{n,m}(\xi)\cos m\varphi \quad (11)$$

where $B_{n,m}$ is an (n, m)th-order spheroidal multipole at the origin.

3.2 MULTIPOLE IMAGES

3.2.1 GROUNDED PLANE

Consider multipole $B_{n,m}$ at point **o**, which is at height h above a grounded plane, as shown in Figure 3. The multipole direction (z axis) makes angle α with the plane. The potential due to $B_{n,m}$ is

$$\psi_B = B_{n,m}Q_{n,m}(\eta)P_{n,m}(\xi)\cos m\varphi \quad (12)$$

To satisfy the zero potential condition on the grounded plane, we place a multipole image $B'_{n,m}$ at **o'** corresponding to coordinates (x', y', z') below the plane by the same distance h, as shown in Figure 3. The magnitude $B'_{n,m}$ of the image is

$$B'_{n,m} = (-1)^{m+1}B_{n,m} \quad (13)$$

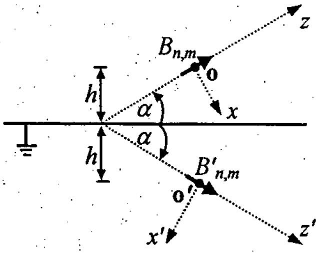

Figure 3. Image $B'_{n,m}$ of a multipole $B_{n,m}$ by a grounded plane.

3.2.2 GROUNDED CONDUCTING PROLATE SPHEROID

Let consider a multipole $B_{n,m}$ outside a grounded conducting prolate spheroid centered at **o**. We re-expand ψ_B about **o** in coordinates (η, ξ, φ) associated with the spheroid as

$$\psi_B = \sum_{i,j} L_{i,j}P_{i,j}(\eta)P_{i,j}(\xi)\cos(j\varphi) \quad (14)$$

where $L_{i,j}$ is the re-expansion coefficient. $L_{i,j}$ can be determined from [18]

$$L_{i,0} = \frac{2i+1}{4\pi P_{i,0}(\eta)}\int_{-1}^{1}\int_{-\pi}^{\pi}\psi_B P_{i,0}(\xi)\,\mathrm{d}\varphi\mathrm{d}\xi \quad (15)$$

and for $j \neq 0$,

$$L_{i,j} = \frac{(2i+1)(i-j)!}{2\pi(i+j)!P_{i,j}(\eta)}\int_{-1}^{1}\int_{-\pi}^{\pi}\psi_B P_{i,j}(\xi)\cos(j\varphi)\,\mathrm{d}\varphi\mathrm{d}\xi \quad (16)$$

Let define multipole $B'_{i,j}$ located at the spheroid center **o** as images of the multipole $B_{n,m}$. Resultant potential ψ outside the spheroid ($\eta \geq \eta_0$) is

$$\psi = \sum_{i,j}\left[L_{i,j}P_{i,j}(\eta) + B'_{i,j}Q_{i,j}(\eta)\right]P_{i,j}(\xi)\cos(j\varphi) \quad (17)$$

From the condition $\psi = 0$ at $\eta = \eta_0$, we can calculate the magnitude of the multipole images,

$$B'_{i,j} = -\frac{P_{i,j}(\eta_0)}{Q_{i,j}(\eta_0)}L_{i,j} \text{ for } i \geq 0 \quad (18)$$

3.3 CALCULATION PROCEDURE

Figure 4 shows the calculation procedure for the configuration in Figure 1. The calculation begins with the expression of the potential ϕ_0 due to $\mathbf{E_0}$ in the prolate spheroidal coordinates (η, ξ, φ).

$$\phi_0 = -(h+Z)E_0 = \sum_{n,m} L_{n,m}P_{n,m}(\eta)P_{n,m}(\xi)\cos(m\varphi) \quad (19)$$

where $L_{0,0} = -hE_0$, $L_{1,0} = -a\sin\alpha E_0$, and $L_{1,1} = a\cos\alpha E_0$.

From the boundary condition on the spheroid surface, we determine the induced multipole $B_{n,m}$ located at **o** from $L_{n,m}$ by using equation (18). That is,

$$B_{0,0} = \left[P_{0,0}(\eta_0)/Q_{0,0}(\eta_0)\right]hE_0 \quad (20a)$$

$$B_{1,0} = \left[P_{1,0}(\eta_0)/Q_{1,0}(\eta_0)\right]a\sin\alpha E_0 \quad (20b)$$

$$B_{1,1} = -\left[P_{1,1}(\eta_0)/Q_{1,1}(\eta_0)\right]a\cos\alpha E_0 \quad (20c)$$

Next, image $B'_{n,m}$ by the grounded plane is applied at **o'** to satisfy the zero-potential condition on the plane by using equation (13). Then, we re-expand potential by $B'_{n,m}$ about **o**, and calculate image multipoles to satisfy the condition of the conducting spheroid. Numerical quadratures are used to evaluate equations (15) and (16). The image application and the re-expansion are repeated until the potential on the spheroid converges.

The calculation in this paper uses the maximal harmonic order n_{max} = 20. We have confirmed that potential on the spheroid surface and the grounded plane differs from zero by not more than $5\times10^{-6}cE_0$.

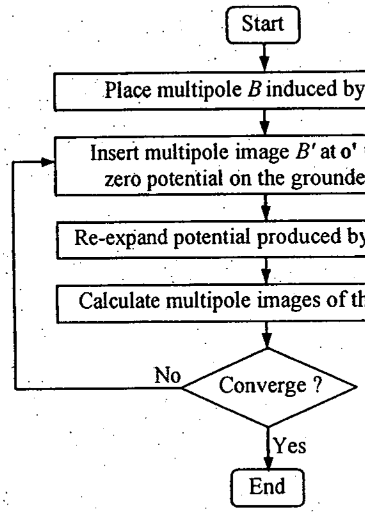

Figure 4. Iterative calculation scheme.

4 RESULTS AND DISCUSSION

4.1 ELECTRIC FIELD

The electric field E on the spheroid surface in Figure 1 is calculated analytically from the gradient of the potential harmonics. From equation (9), the electric field on the spheroid in the η direction is

$$E_\eta = -\frac{1}{h_\eta}\sum_{n,m}\left[L_{n,m}P'_{n,m}(\eta) + B_{n,m}Q'_{n,m}(\eta)\right]P_{n,m}(\xi)\cos(m\varphi) \quad (21)$$

where the prime notation denotes the derivative of the associated Legendre functions with respect to η, and h_η is the scale factor in the η coordinate [18].

Figures 5a and 5b show the distribution of electric field along the η_0 contour (spheroid surface) on the y = 0 plane when α = 0°, 15°, 45°, and 90° for c/b = 2 and 4, respectively. The electric field is plotted as a function of the normalized arc length l/L, where l is arc length measured from the lower pole and L is the arc length between two poles. For c/b = 2 in Figure 5a, when α = 0°, the electric field is more or less uniform on a wide range of l/L. With increasing α, the field distribution becomes more non-uniform on the contour. The field maximum E_{max} increases and takes place near the upper pole. The position of E_{max} moves to the top pole as α increases to 90°. For larger axis ratio c/b = 4, the field behavior in Figure 5b is similar to that for c/b = 2, but the field is more non-uniform and E_{max} is significantly higher for the same α. The position of E_{max} is clearly noticeable even when α = 0°.

Figure 6 presents the maximal field as a function of α for c/b = 1, 2, 4, and 6. Note that c/b = 1 corresponds to the case of a sphere. The figure clearly shows the field enhancement on the spheroids with increasing α. When the spheroid stands on the plane (α = 90°), the field is intensified by 3, 6.5, and 10 times from that in the lying position (α = 0°) for c/b = 2, 4, and 6, respectively.

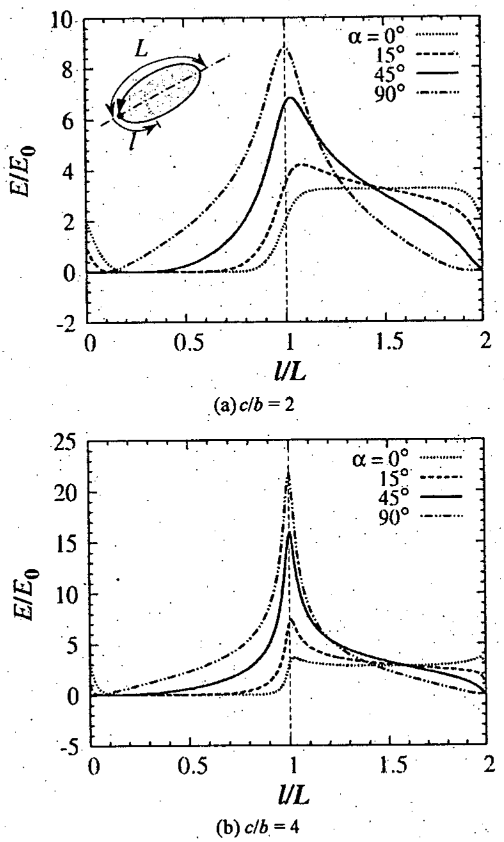

(a) c/b = 2

(b) c/b = 4

Figure 5. Distribution of electric field along the η_0 contour on the y = 0 plane with different tilt angles α for two c/b values.

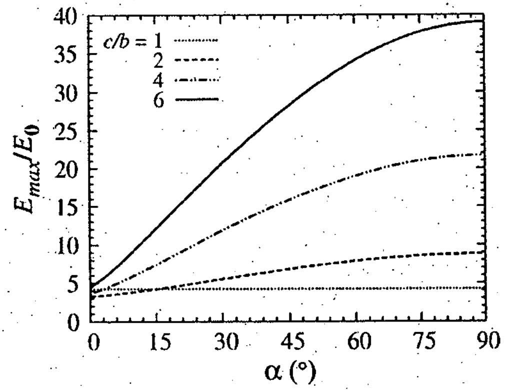

Figure 6. Maximal field as a function of angle α for different c/b ratios.

4.2 ELECTROSTATIC FORCE

The electrostatic force $\mathbf{F}_e$ on a conducting spheroid is determined by,

$$\mathbf{F}_e = \frac{\varepsilon_E}{2}\oint\!\!\!\oint_S E^2\mathbf{a}_n dS \quad (22)$$

where S is the surface of the spheroid and $\mathbf{a}_n$ is the unit outward normal vector. The invariance of energy with respect to the X and Y positions of the spheroid implies that $\mathbf{F}_e$

vanishes in the X and Y directions for the configuration in Figure 1. In addition, $\mathbf{F}_e$ is always in the upward direction. The magnitude F_e depends on its surface area. To examine the effects of the spheroid shape, we keep the minor axis constant, $b = b_0$, and vary the c/b ratio.

Figure 7 shows the electrostatic stress along the η_0 contour (spheroid surface) on the $y = 0$ plane for $\alpha = 0°$, 15°, 45°, and 90° when $c/b = 2$. The stress vectors are presented on the same scale for Figures 7a–7d. Figure 7 indicates that the force on the spheroid is governed by the stress on the upper half. The stress becomes concentrated near the higher pole when $\alpha > 0°$. Figures 7b and 7c imply that the force produces a torque rotating the spheroid about the contact point in the increasing-α direction.

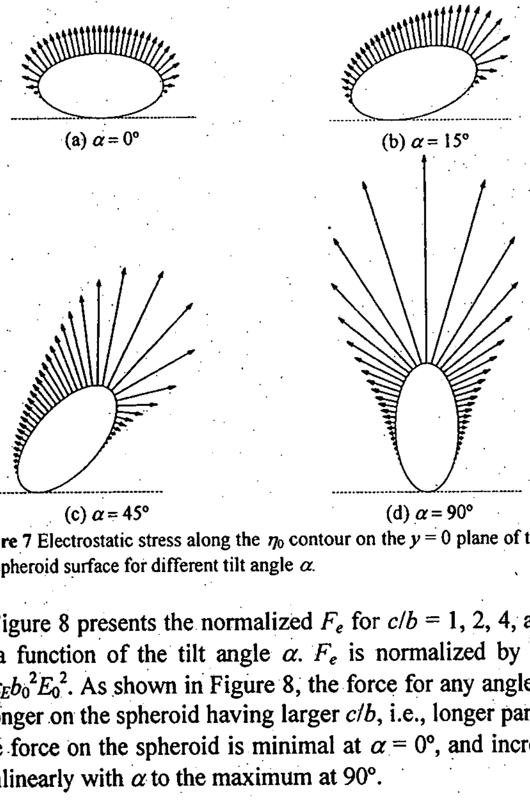
(a) $\alpha = 0°$ (b) $\alpha = 15°$

(c) $\alpha = 45°$ (d) $\alpha = 90°$

Figure 7 Electrostatic stress along the η_0 contour on the $y = 0$ plane of the c/b = 2 spheroid surface for different tilt angle α.

Figure 8 presents the normalized F_e for c/b = 1, 2, 4, and 6 as a function of the tilt angle α. F_e is normalized by $F_0 = 4\pi\varepsilon_E b_0^2 E_0^2$. As shown in Figure 8, the force for any angle α is stronger on the spheroid having larger c/b, i.e., longer particle. The force on the spheroid is minimal at $\alpha = 0°$, and increases nonlinearly with α to the maximum at 90°.

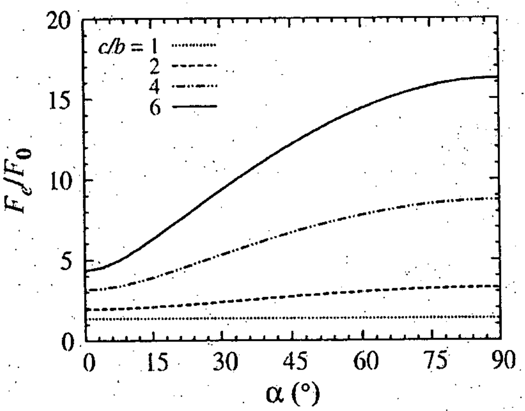

Figure 8. Electrostatic force on the spheroids having the same minor semi-axis for different c/b as a function of α.

Figures 9a and 9b show the minimal force F_{min} when $\alpha = 0°$ and the maximal force F_{max} when $\alpha = 90°$ in relation with c/b from 1 to 10, respectively. The minimal force in Figure 9a increases linearly with c/b. On the other hand, Figure 9b presents F_{max} on logarithmic scales, as F_{max} is highly intensified with increasing c/b ratio.

The following empirical formulae, obtained by curve fitting, may be used for estimating the minimal and maximal forces:

$$\frac{F_{min}}{F_0} = 0.6\frac{c}{b} + 0.76 \tag{23}$$

$$\frac{F_{max}}{F_0} = 0.63\left(\frac{c}{b} + 0.58\right)^{\sqrt{3}} \tag{24}$$

The approximated values are shown as the symbols in Figure 9. Equations (23) and (24) give F_{min} and F_{max} with error smaller than 1% for c/b between 1 and 10.

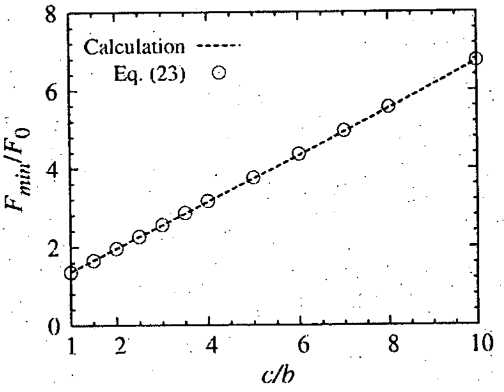

(a) Minimal force

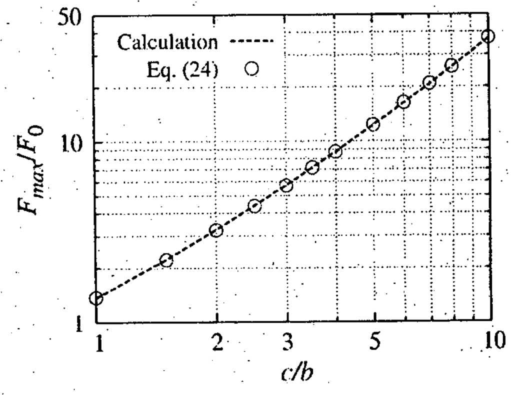

(b) Maximal force

Figure 9. Variation of the normalized minimal and maximal forces on the spheroids having the same minor semi-axis with axis ratio c/b.

4.3 ELECTROSTATIC TORQUE

The electrostatic torque T_e on the spheroid about the contact point $\mathbf{p}$ is determined from the electrostatic stress $\mathbf{f}$ as

$$T_e = \oiint_S (-v f_X + u f_Z)\,\mathrm{d}S \tag{25}$$

where the subscripts X and Z indicate the components of $\mathbf{f}$ and (u, v) are the (X, Z) coordinates in relation to $\mathbf{p}$, as shown in Figure 10. Positive torque is referred to the $+\alpha$ direction.

Figure 11 shows the normalized T_e on the spheroids having the same minor semi-axis b_0 for $c/b = 2, 4, 6$ as a function of α. T_e is normalized by $T_0 = F_0 b_0$. T_e is zero at $\alpha = 0°$ and 90° due to the symmetry of configuration in Figure 1. Figure 11 shows that T_e is always positive for α between 0° and 90°, i.e., in the increasing-α direction. Maximum of T_e is approximately at $\alpha = 45°$. Quadratic (parabolic) relationships are plotted in comparison with calculation results in Figure 11, and only small difference can be seen for $\alpha > 45°$. For the same α, the torque is greater on the spheroid having larger c/b (longer particle).

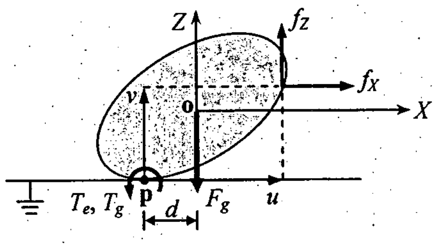

Figure 10. Calculation of torque T_e and T_g on a spheroid.

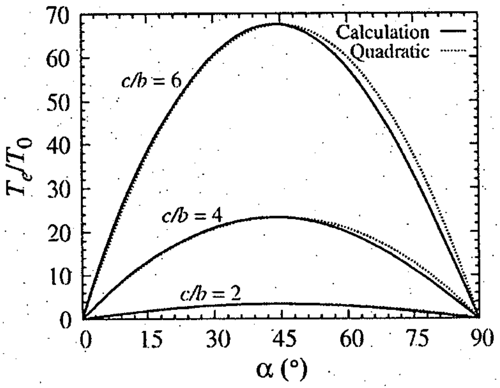

Figure 11. Electrostatic torque on the spheroids as a function of α.

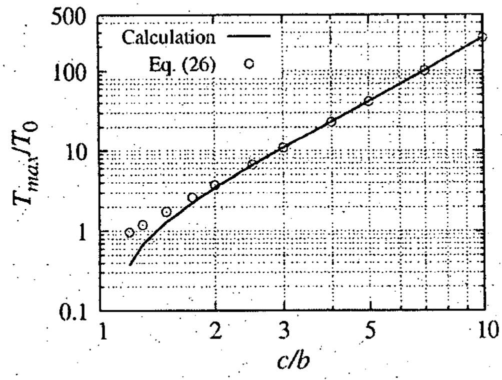

Figure 12. Maximal electrostatic torque on the spheroid in relation with c/b.

Figure 12 shows the variation of the maximal torque T_{max} with c/b from 1 to 10 on logarithmic scales. When $c/b \geq 2$, we may approximate T_{max} by

$$T_{max}/T_0 \approx 0.6(c/b)^{2.6} \tag{26}$$

The approximated values by equation (26) are compared with the calculation results in Figure 12.

4.4 ELECTROMECHANICAL BEHAVIOR WITH GRAVITATIONAL EFFECTS

In this section, we examine the electromechanical behavior of the conducting prolate spheroid in Figure 1 when the gravitational force F_g is taken into account. F_g does not only restrain the spheroid from lifting motion, but also contributes to torque T_g. For $\alpha = 0°$ or 90°, the spheroid is lifted from the grounded plane without rotation if F_e is greater than F_g. For other α values, the behavior of the spheroid is more complicated due to nonzero total torque T_{tot} that includes the gravitational torque. Note that there is also a normal force at **p**, but it does not produce torque about **p**.

4.4.1 Total Torque on Spheroid

The gravitational torque T_g is determined by

$$T_g = -F_g d \tag{27}$$

which is in the opposite direction to the electrostatic torque T_e.

As an example, we may consider aluminum spheroidal particles having the same $b = 0.25$ mm and different c. The mass density of aluminum is about 2700 kg/m^3. Figure 13 presents T_g on the aluminum particles as a function of α for $c = 0.5$, 1.0, and 1.5 mm. As F_g is constant for a particle, T_g magnitude follows the characteristic of d defined in equation (3). We can see from Figure 13 that T_g increases with increasing α from 0°, and reaches the peak at $\alpha < 45°$ and then decreases to zero at $\alpha = 90°$. The angle of maximal T_g reduces with increasing the particle length.

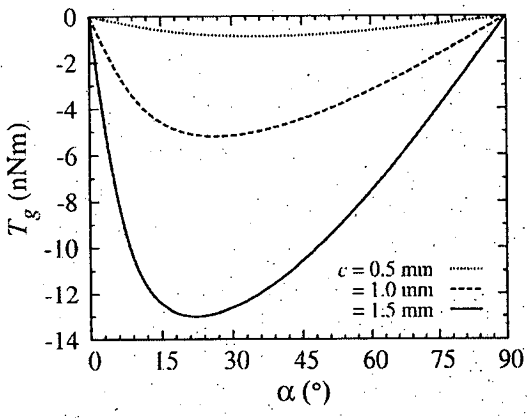

Figure 13. Gravitational torque on aluminum spheroidal particles having $b = 0.25$ mm.

Figure 14 shows the total torque T_{tot} (= $T_e + T_g$) on the aluminum particle of $b = 0.25$ mm and $c = 1$ mm for $E_0 = 2$, 3, 4, and 6 kV/cm. For small $E_0 = 2$ kV/cm, T_g is predominant over T_e for all α values, resulting in negative T_{tot} (reducing-α direction). On the other hand, for large $E_0 = 6$ kV/cm, T_e is predominant and T_{tot} is positive for the range $0° < \alpha < 90°$. For intermediate E_0 values, T_{tot} is negative at small α and becomes positive when α is greater than critical tilt angle α_c. The critical angle in Figure 14 decreases when E_0 increases from 3 to 4 kV/cm.

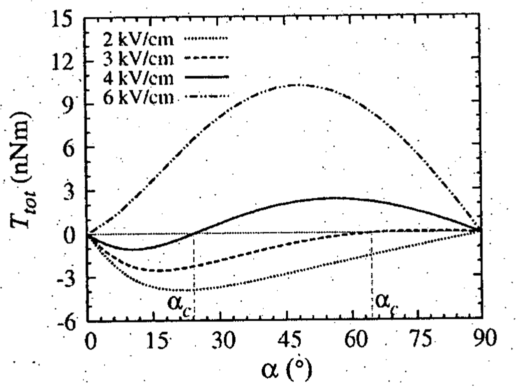

Figure 14. Total torque on an aluminum spheroidal particle of b = 0. 25 mm and c = 1 mm as a function of α for different E_0 values.

4.4.2 CLASSIFICATION OF ELECTROMECHANICAL BEHAVIOR

From the aforementioned results, we can deduce that for tilt angle 0° < α < 90°, the conducting spheroidal particle may be subject to (i) total torque about contact point whose direction depends on field strength and (ii) lifting force if the field is strong enough. Figure 15 presents the critical field E_R and E_L of the aluminum particle having b = 0.25 and c = 1 mm (c/b = 4) for the rotating (T_{tot} = 0) and lifting ($F_e = F_g$) conditions, respectively, as a function of α. Assume that an aluminum particle is at angle α_0, possibly caused by mechanical operation or disturbance, the electromechanical behavior may be classified as follows:

1. $E_0 < E_R(\alpha_0)$: the particle is rotated by T_{tot} to the lying orientation (α = 0°).
2. $E_R(\alpha_0) < E_0 < E_L(\alpha_0)$: the torque T_{tot} rotates to increase α.
   - 2a. If $E_0 < E_L(90°)$: the particle obtains the standing orientation (α = 90°) without lifting.
   - 2b. If $E_0 > E_L(90°)$: the particle rotates and then lifts.
3. $E_0 > E_L(\alpha_0)$: the particle is lifted from the plane and may be rotated as $E_0 > E_R(\alpha_0)$.

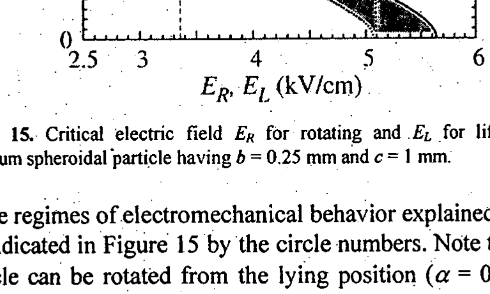

Figure 15. Critical electric field E_R for rotating and E_L for lifting the aluminum spheroidal particle having b = 0.25 mm and c = 1 mm.

The regimes of electromechanical behavior explained above are indicated in Figure 15 by the circle numbers. Note that the particle can be rotated from the lying position (α = 0°) with little mechanical disturbance when $E_0 > E_R(0°)$, by which $dT_{tot}/d\alpha > 0$. Moreover, if $E_R(0°)$ is greater than $E_L(90°)$, the particle is then lifted from the electrode when α reaches a critical angle between 0 and α_1, where $E_L(\alpha_1) = E_R(0°)$. Note that the minimum field that can lift the particle is $E_L(90°)$. The E_R and E_L characteristics imply that this minimum field $E_L(90°)$ can lift a particle making angle $\alpha_0 \geq \alpha_2$, where $E_R(\alpha_2) = E_L(90°)$. Figure 15 shows α_1 and α_2 for the aluminum spheroidal particle (b = 0.25 mm and c = 1 mm).

Figure 16 presents the characteristics of E_R and E_L of an aluminum particle for b = 0.25 mm and different c/b values, i.e., 1.2, 1.45, 2, and 6. The figure shows that $E_R(0°) < E_L(90°)$ for the small axis ratio c/b < 1.45 (sphere-like particle). For larger c/b values, $E_R(0°) > E_L(90°)$. That is, a wire-like particle tends to be lifted from the plane after rotated from the lying position by the electric field.

The angle α_1 and α_2 are calculated for the particles having b = 0.1, 0.25, and 0.5 mm. Figure 17 presents α_1 and α_2 as a function of c/b for the particles. It is clear from the figure that the angles mainly depend on the axis ratio not the minor axis. With c/b increasing (from 1.45), α_1 decreases but α_2 increases.

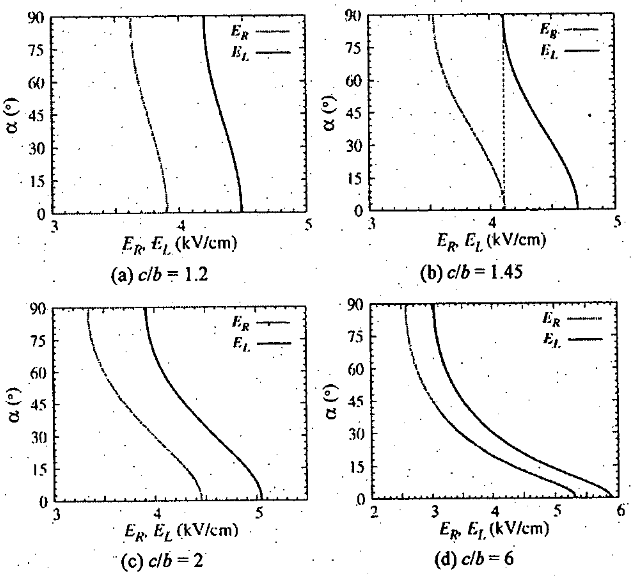

(a) c/b = 1.2

(b) c/b = 1.45

(c) c/b = 2

(d) c/b = 6

Figure 16. Rotating and lifting field of aluminum spheroidal particles having the same b = 0.25 mm for different c/b values.

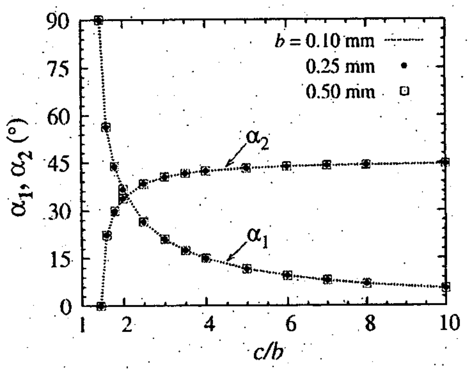

Figure 17. Angle α_1 and α_2 as a function of axis ratio c/b for the aluminum particles.

5 CONCLUSION

This work applies the multipole image method to an analysis on electromechanics of a conducting spheroid in a three-dimensional configuration. The effects of axis ratio c/b and tilt angle α on the electric field, force, and torque have been clarified. The electrostatic force on the spheroids having the same minor axis increases nonlinearly with major axis and α. The electrostatic torque always tends to rotate the spheroid to the standing position and the torque maximum is at α about 45°. The electromechanical behavior of a conducting spheroid is classified into three regimes based on the possibility of lifting and the direction of rotation. It is found from the behavior that the total torque on a conducting spheroid increases the probability of the spheroid to be lifted from the grounded plane.

ACKNOWLEDGMENTS

This work was supported by the AUN/SEED-Net program, JICA and the Thailand Research Fund. B.T. also thanks Prof. Tadasu Takuma at The Tokyo Denki University for the discussion and comments.

REFERENCES

[1] N. Fujimoto and G. L. Ford, "Results of recent GIS fault survey", IERE Workshop on Gas insulated substations, pp. 1.1-1.7, 1996.

[2] G. W. Brown, R. Samm and J. Cronin, "AC analysis and testing of realistically contaminated gas insulated system", IEEE Trans. Power App. Syst., Vol. 97, No. 1, pp. 59-67, 1978.

[3] T. Takuma and B. Techaumnat, *Electric fields in composite dielectrics and their applications*, Springer, Netherlands, 2010.

[4] M. M. Morcos, S. A. Ward, H. Anis, K. D. Srivastava and S. M. Gubanski, "Insulation Integrity of GIS/GITL systems and management of particle contamination", IEEE Electr. Insul. Mag., Vol. 16, No. 5, pp. 25-37, 2000.

[5] K. Sakai, D. L. Abella, Y. Khan, J. Suehiro and M. Hara, "Experimental studies of free conducting wire particle behavior between non-parallel plane electrodes with ac voltages in air", IEEE Trans. Dielectr. Electr. Insul., Vol. 10, No. 3, pp. 418-424, 2003.

[6] K. Asano, K. Anno and Y. Higashiyama, "The behavior of charged conducting particles in electric fields", IEEE Trans. Ind. Appl., Vol. 33, No. 3, pp. 679-686, 1997.

[7] K. Sakai, S. Tsuru, D. L. Abella and M. Hara, "Conducting particle motion and particle-initiated breakdown in dc electric field between diverging conducting plates in atmospheric air", IEEE Trans. Dielectr. Electr. Insul., Vol. 6, No. 1, pp. 122-130, 1999.

[8] K. Sakai, D. L. Abella, Y. Khan, J. Suehiro and M. Hara, "Theoretical and experimental studies for spherical free-conducting particle behavior between non-parallel plane electrodes with ac voltages in air", IEEE Trans. Dielectr. Electr. Insul., Vol. 10, No. 3, pp. 404-417, 2003.

[9] C. M. Cooke, R. E. Wootton and A. H. Cookson, "Influence of particles on ac and dc electrical performance of gas insulated systems at extra-high-voltage", IEEE Trans. Pow. App. Syst., Vol. 96, No. 3, pp. 768-777, 1977.

[10] N. J. Félici, "Forces et charges de petits objets en contact avec une électrode affectée d'un champ électrique", Rev. Gén. Elec., Vol. 75, No. 10, pp. 1145-1160, 1966.

[11] M. Hara and M. Akazaki, "A method for prediction of gaseous discharge threshold voltage in the presence of a conducting particle", J. Electrost., Vol. 2, No. 3, pp. 223-239, 1977.

[12] K. Sakai, D. L. Abella, J. Suehiro and M. Hara, "Charging and behavior of a spherically conducting particle on a dielectrically coated electrode in the presence of electrical gradient force in atmospheric air", IEEE Trans. Dielectr. Electr. Insul., Vol. 9, No. 4, pp. 577-587, 2002.

[13] N. Phansiri and B. Techaumnat, "Study on the electromechanics of a conducting particle under nonuniform electric field", IEEE Trans. Dielectr. Electr. Insul., Vol. 20, No. 2, pp. 488-495, 2013.

[14] V. Q. Huynh, B. Techaumnat and K. Hidaka, "Analysis on electrostatic behavior of a conducting prolate spheroid under an electric field", IEEE Trans. Dielectr. Electr. Insul., Vol. 20, No. 6, pp. 2230-2238 2013 (Paper TDEI No. 3898).

[15] B. Techaumnat and T. Takuma, "Calculation of electric field in two-dimensional arrangements by the method of multipole images", J. Electrost., Vol. 64, No. 10, pp. 706-716, 2006.

[16] B. Techaumnat and M. Washizu, "Equivalent image charges of a prolate spheroid under an external field", J. Electrost., Vol. 69, No. 4, pp. 388-393, 2011.

[17] J. Satterly, "Formulae for volumes, surface areas and radii of gyration of spheres, ellipsoids and spheroids", The Mathematical Gazette, Vol. 44, No. 347, pp. 15-19, 1960.

[18] W. R. Smythe, *Static and dynamic electricity*, 2nd ed., McGRAW-HILL, New York, Ch. 5, 1950.

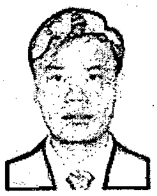

Viet Quoc Huynh was born in Ben Tre, Vietnam in 1985. He received the B.Sc. degree from Ho Chi Minh city University of Technology, Vietnam in 2008, and the M.Sc. degree from Chulalongkorn University, Thailand in 2011. He is now a doctoral student at Faculty of Engineering of the Chulalongkorn University. His research interest is the analysis of electric field in high voltage engineering.

Boonchai Techaumnat (M'02) was born in Bangkok, Thailand in 1970. He received the B.Eng. degree in 1990, M.Eng. degree in 1995 from Chulalongkorn University, Thailand, and the doctoral degree in electrical engineering from Kyoto University in 2001. He joined the Faculty of Engineering, Chulalongkorn University as a lecturer in 1995. He is now an Associate Professor at the faculty. Dr. Techaumnat received the medal prize for new scholars from the Thailand Research Fund in 2005, the Nanobiotechnology Premium from the Institution of Engineering and Technology (IET) in 2009, and the book prize from the Institute of Electrical Engineers Japan in 2011 for "Electric Fields in Composite Dielectrics and Their Applications". His research interests include numerical field analysis, electrical insulation, bioelectromagnetics, and particle electrokinetics.

Kunihiko Hidaka (M'76-SM'04-F'12) received the B.E., M.E., and D.Eng. degrees from the University of Tokyo in 1976, 1978, and 1981 respectively. Since 1987 he has been with the Department of electrical engineering of the University of Tokyo and is now a professor of electrical engineering. He has been engaged in the development of electric field sensors, research on electrical breakdown phenomena concerned with high voltage technology, and has specialized in computer simulation of high-voltage structures. His work has won premiums and awards from both the Japanese and British IEE and the Institute of Electrostatics Japan. He is a Fellow of IEEJ. He is now acting as President-Elect of IEEJ.

PW025

การศึกษาการเคลื่อนที่ของอนุภาคตัวนำภายใต้สนามไฟฟ้าไม่สม่ำเสมอ

Study on the Movement of Conducting Particles under Nonuniform Electric Field

นิศรุต พันธ์ศิริ[1] และ บุญชัย เตชะอำนาจ[1]
[1] ภาควิชาวิศวกรรมไฟฟ้า คณะวิศวกรรมศาสตร์ จุฬาลงกรณ์มหาวิทยาลัย
ถนนพญาไท เขตปทุมวัน กรุงเทพ 10330 โทรศัพท์ 02-218-6548 E-mail: nisarut_ph@hotmail.com, boonchai.t@chula.ac.th

บทคัดย่อ

บทความนี้กล่าวถึงการศึกษาการเคลื่อนที่ของอนุภาคตัวนำทรงกลมภายใต้สนามไฟฟ้าไม่สม่ำเสมอ โดยใช้การจำลองเชิงเลขและใช้การทดลองในระบบอิเล็กโตรดด้วยแรงดันไฟฟ้ากระแสตรงในอากาศ เป้าหมายของการวิเคราะห์ คือแรงที่กระทำและทิศทางการเคลื่อนที่ของอนุภาค การเคลื่อนที่ของอนุภาคคำนวณได้จากสมการของแรงคูลอมบ์ แรงเกรเดียนต์ไฟฟ้า แรงโน้มถ่วง และแรงหนืด ผลการศึกษาแสดงว่า ผลของแรงทางไฟฟ้าและคุณสมบัติการกระทบระหว่างอนุภาคและอิเล็กโตรดทำให้อนุภาคเคลื่อนที่ไปยังบริเวณที่มีค่าสนามไฟฟ้าที่ต่ำกว่า ระยะกระจัดในแนวระนาบที่อนุภาคกระทบอิเล็กโตรดกราวนด์เป็นครั้งที่สองที่ได้มาจากการคำนวณและการทดลองมีค่าใกล้เคียงกัน นอกจากนั้นเมื่อมุมระหว่างอิเล็กโตรดเพิ่มขึ้นทำให้ระยะกระจัดในแนวระนาบของการเคลื่อนที่ของอนุภาคเพิ่มขึ้นเช่นกัน ถ้าตำแหน่งเริ่มต้นของอนุภาคมีค่าสนามไฟฟ้าเท่ากัน

คำสำคัญ: สนามไฟฟ้าไม่สม่ำเสมอ, อนุภาคตัวนำ, สวิตช์เกียร์แบบฉนวนก๊าซ

Abstract

This article presents the study on the movement of particle under DC nonuniform electric field by using numerical calculation and experiment. The objective is to analyze the forces acting on particle and trajectory of the particle by using the equations of Coulomb force, gradient force, gravitational force and viscous force. The results show that the electrical forces and the impact between the particle and the electrodes take the particle to the lower electric field of region. The results are verified by experiment. The displacement of the second impact on the lower electrode from origin position agreed with the calculation result. Moreover, the displacement in the *x* direction of the particle increases with the angle between the electrodes if the magnitude of electric field at position of particle is the same.

Keywords: nonuniform electric field, conducting particle, gas insulated switchgears

1. บทนำ

ในปัจจุบันสถานีไฟฟ้าแรงสูงมีจำนวนเพิ่มขึ้นอย่างมาก เนื่องจากความจำเป็นในการใช้ประโยชน์จากพลังงานไฟฟ้าเพิ่มขึ้นอย่างต่อเนื่องทั้งในภาคอุตสาหกรรมการผลิต การขนส่ง การจำหน่าย และในชีวิตประจำวัน เมื่อเทคโนโลยีในการออกแบบอุปกรณ์สวิตช์เกียร์สำหรับระบบไฟฟ้าแรงสูงมีการพัฒนาดีขึ้น จึงมีแนวคิดที่จะออกแบบให้บรรจุอุปกรณ์สวิตช์เกียร์ในโครงสร้างปิดและบรรจุวัสดุฉนวน เช่น ก๊าซ สุญญากาศ หรือน้ำมันฉนวน ไว้ภายใน ตัวอย่างเช่น สวิตช์เกียร์แบบฉนวนก๊าซ (Gas Insulated Switchgears หรือ GIS) ที่รู้จักกันในปัจจุบัน โครงสร้างหลักของระบบสวิตช์เกียร์แบบปิดประกอบไปด้วย ตัวนำไฟฟ้าแรงสูง ตัวถังโลหะ และฉนวนก๊าซ แสดงในรูปที่ 1 สนามไฟฟ้าในระบบเป็นแบบไม่สม่ำเสมอ โดยมีค่าสูงที่ใกล้ตัวนำด้านใน

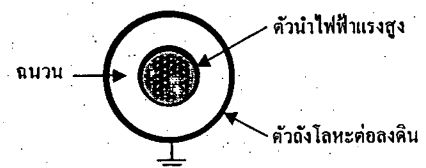

รูปที่ 1 โครงสร้างหลักของสวิตช์เกียร์แบบฉนวนก๊าซ

เป็นที่ทราบกันดีว่า อนุภาคตัวนำอิสระในระบบฉนวน ซึ่งอาจเกิดจากการบำรุงรักษาระบบ ปะปนมากับก๊าซฉนวน หรือเกิดจากการชำรุดของส่วนประกอบที่เป็นโลหะ ทำให้ความสามารถในการฉนวนของก๊าซลดลง ทั้งนี้อนุภาคทำให้สนามไฟฟ้าระหว่างตัวนำไฟฟ้าแรงสูงและกราวนด์เพิ่มขึ้นเฉพาะที่ จึงอาจนำไปสู่การเกิดดีสชาร์จบางส่วน หรือเกิดการเบรกดาวน์ในระบบ [1, 2] ซึ่งเหตุการณ์ดังกล่าวทำให้ระบบเกิดความเสียหายได้ สนามไฟฟ้าที่เกิดขึ้นระหว่างตัวนำไฟฟ้าแรงสูงและตัวถังโลหะเหนี่ยวนำให้เกิดประจุที่ผิวของอนุภาคตัวนำ และทำให้เกิดแรงไฟฟ้ากระทำกับอนุภาคขึ้น เนื่องจากปฏิกิริยาระหว่างประจุเหนี่ยวนำกับสนามไฟฟ้า เมื่อแรงไฟฟ้าที่เกิดขึ้นกับอนุภาคมีผลเหนือกว่าแรงโน้มถ่วงและแรงเสียดทานอื่นๆ อนุภาคตัวนำอิสระก็สามารถเคลื่อนที่ภายใต้สนามไฟฟ้าไปในทิศทางต่างๆได้ อนุภาคซึ่งเคลื่อนที่ไปในบริเวณใดๆ จะทำให้ค่าสนามไฟฟ้าบริเวณนั้นมีค่าสูงขึ้นมากกว่าสนามไฟฟ้าค่าปกติ และทำให้มีความเสี่ยงที่จะเกิดดีสชาร์จบางส่วน หรือเกิดเบรกดาวน์ขึ้นได้ ดังนั้นการศึกษาลักษณะสมบัติทางกลศาสตร์ไฟฟ้าของอนุภาคจึงมีความสำคัญอย่างยิ่งยวดต่อการพัฒนาระบบฉนวนไฟฟ้าแรงสูง

บทความนี้เสนอผลการศึกษาการเคลื่อนที่ของอนุภาคทรงกลมในระบบอิเล็กโตรด โดยทำการจำลองการเคลื่อนที่ของอนุภาคภายใต้สนามไฟฟ้าไม่สม่ำเสมอและผลทดลองการสังเกตการเคลื่อนที่ของอนุภาคเพื่อยืนยันผลการจำลองที่ได้ การศึกษามีวัตถุประสงค์ที่จะทำให้เข้าใจถึงลักษณะการเคลื่อนที่ของอนุภาคและผลของระดับความไม่สม่ำเสมอของสนามไฟฟ้า ความหนืดของตัวกลาง ที่มีต่อการเคลื่อนที่ของอนุภาค

2. ระบบอิเล็กโตรดและแรงที่กระทำกับอนุภาค

ระบบอิเล็กโตรดและอนุภาคที่พิจารณาแสดงในรูปที่ 2 อิเล็กโตรดเป็นแบบระนาบ 2 มิติ ซึ่งทำมุมกันเท่ากับ θ_0 โดยที่ระนาบอิเล็กโตรดด้านล่างต่อกราวนด์ และระนาบอิเล็กโตรดบนได้รับแรงดันไฟฟ้าจากแหล่งจ่าย ในการอ้างอิงตำแหน่งในระบบอิเล็กโตรดนี้ ผู้วิจัยใช้ระบบพิกัดเชิงขั้ว (r,θ) หรือระบบพิกัดคาร์ทีเซียน (x,z) ซึ่งมีจุดกำเนิดอยู่ที่จุดตัด ระหว่างแนวระนาบอิเล็กโตรด เมื่อใช้พิกัดดังกล่าวอ้างอิงตำแหน่งของอนุภาคในระบบอิเล็กโตรดนี้ จะใช้ดัชนีล่าง p กำกับไว้

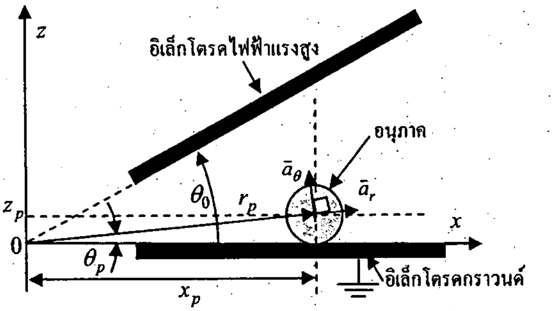

รูปที่ 2 ระบบอิเล็กโตรดและอนุภาคที่ใช้พิจารณา

สนามไฟฟ้าในระบบอิเล็กโตรดที่พิจารณาเป็นแบบไม่สม่ำเสมอ สามารถหาขนาดและทิศทางสนามไฟฟ้า ณ ตำแหน่ง (r,θ) ได้จาก

$$\bar{E}(r,\theta) = \frac{V}{r\theta_0}\bar{a}_\theta \qquad (1)$$

อนุภาคตัวนำที่วางอยู่บนระนาบอิเล็กโตรดภายใต้สนามภายนอก E_0 จะเกิดประจุเหนี่ยวนำ q_{ind} ขึ้น ถ้าพิจารณาอนุภาครัศมี a บนระนาบกราวนด์ภายใต้สนามไฟฟ้า E_0 ในทิศทางพุ่งลงมาที่ระนาบ จะได้ว่า [3]

$$q_{ind} = -\frac{2}{3}\pi^3\varepsilon_0\varepsilon_s E_0 a^2 \qquad (2)$$

เมื่อ ε_s คือ ค่าคงตัวไดอิเล็กตริกของตัวกลาง

แรงที่กระทำกับอนุภาคที่แสดงในรูปที่ 2 มีดังนี้

แรงคูลอมบ์

ประจุเหนี่ยวนำบนอนุภาคตัวนำ ซึ่งวางตัวอยู่บนระนาบอิเล็กโตรดจะเกิดแรงคูลอมบ์ F_q กระทำเนื่องจากสนามไฟฟ้าภายนอก E_0 เมื่ออ้างอิงแรง F_q ในทิศทาง $+z$ ขึ้นออกจากอิเล็กโตรด ขนาดของแรงเป็นไปตามสมการ

$$F_q = 0.832|q_{ind}|E_0 \qquad (3)$$

เมื่ออนุภาคตัวนำยกตัวออกจากระนาบอิเล็กโตรด ไม่สัมผัสกับระนาบอิเล็กโตรด แรงคูลอมบ์ที่กระทำกับอนุภาคประมาณได้เป็น

$$F_q = q_{ind}E_0 \qquad (4)$$

ซึ่งสามารถหาแรงคูลอมบ์ที่ตำแหน่ง (r_p,θ_p) คือ

$$\bar{F}_q = \pm\frac{2\pi^3\varepsilon_0\varepsilon_s a^2V^2}{3r_p^2\theta_0^2}\bar{a}_\theta \qquad (5)$$

ในสมการที่ (5) เครื่องหมายลบจะใช้เมื่ออนุภาคที่เคลื่อนที่ออกจากระนาบอิเล็กโตรดบน หลังจากได้รับประจุเหนี่ยวนำจากการกระทบกับอิเล็กโตรดบนแล้ว

แรงเกรเดียนต์ไฟฟ้า

เมื่ออนุภาคตัวนำอยู่ภายใต้สนามไฟฟ้าไม่สม่ำเสมอ จะเกิดปฏิกิริยาระหว่างไดโพลเหนี่ยวนำของอนุภาคกับสนามไฟฟ้า ไดโพลเหนี่ยวนำ p_{ind} สามารถหาได้จาก [4]

$$\bar{p}_{ind} = 4\pi\varepsilon_0 K_{CM}a^3\bar{E}_0 \qquad (6)$$

เมื่อ K_{CM} คือตัวประกอบ Clausius-Mossotti

แรงเกรเดียนต์ไฟฟ้า $\bar{F}_{gd}$ คือแรงที่กระทำกับไดโพลเหนี่ยวนำนี้เนื่องจากสนามไฟฟ้า $\bar{E}_0$ $\bar{F}_{gd}$ คำนวณได้จาก

$$\bar{F}_{gd} = (\bar{p}_{ind}\cdot\nabla)\bar{E}_0 \qquad (7)$$

ซึ่งได้แรงเกรเดียนไฟฟ้าเป็น [5]

$$\bar{F}_{gd} = \frac{4\pi\varepsilon_0\varepsilon_s a^3V^2}{r_p^3\theta_0^2}\bar{a}_r \qquad (8)$$

สังเกตว่าแรงเกรเดียนต์ไฟฟ้า มีทิศทางที่จะเคลื่อนที่อนุภาคไปยังบริเวณที่มีสนามไฟฟ้าสูงกว่าตำแหน่งปัจจุบัน

แรงโน้มถ่วง

แรงโน้มถ่วงที่ทำกับอนุภาคในรูปที่ 2 มีทิศทาง $-z$ และคำนวณได้จาก

$$\bar{F}_g = -\frac{4}{3}\pi a^3 g(\rho_p - \rho_s)\bar{a}_z \qquad (9)$$

เมื่อ ρ_p คือความหนาแน่นอนุภาค, ρ_s คือความหนาแน่นอากาศ และ g ความเร่งเนื่องจากแรงโน้มถ่วง

แรงหนืด

แรงหนืดมีทิศทางตรงข้ามกับการเคลื่อนที่ของอนุภาค สำหรับ อนุภาคทรงกลมที่เคลื่อนที่ด้วยความเร็ว $\bar{v}$ ภายในตัวกลางที่มีสัมประสิทธิ์ความหนืด η

$$\bar{F}_v = -6\pi\eta a\bar{v} \qquad (10)$$

3. การจำลองการเคลื่อนที่ของอนุภาค

การคำนวณการเคลื่อนที่ของอนุภาคในระบบอิเล็กโตรดใช้วิธีการคำนวณการเคลื่อนที่แบบ 2 มิติ แรงทั้งหมดที่กระทำกับอนุภาคจะ

ถูกแยกองค์ประกอบในแกน x และ z เมื่อพิจารณาอนุภาคมวล m เคลื่อนที่ภายใต้สนามไฟฟ้าแสดงในรูปที่ 3 ความเร่ง $\bar{a}_x$ และ $\bar{a}_z$ ของอนุภาคบนตำแหน่ง (r_p, θ_p) คำนวณได้จาก

$$F_x = -F_q \sin\theta_p - F_{gd}\cos\theta_p + F_{vx} = ma_x \tag{11}$$

$$F_z = F_q \cos\theta_p - F_{gd}\sin\theta_p - F_{vz} - F_g = ma_z \tag{12}$$

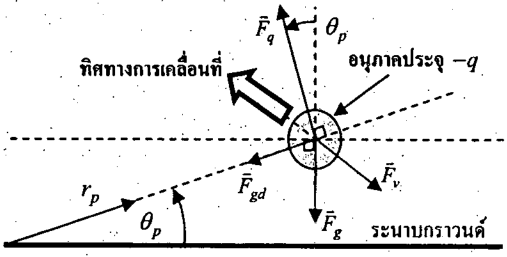

รูปที่ 3 แรงที่กระทำต่ออนุภาคและชนิดประจุ

สัมประสิทธิ์การกระทบระหว่างอนุภาคกับอิเล็กโตรด

อนุภาคเคลื่อนที่ในระบบอิเล็กโตรด เมื่ออนุภาคกระทบอิเล็กโตรด ความเร็วของอนุภาคเกิดการเปลี่ยนแปลง สัมประสิทธิ์การกระทบระหว่างอนุภาคและอิเล็กโตรดจึงเป็นพารามิเตอร์สำคัญที่กำหนดแนวการเคลื่อนที่ของอนุภาคในระบบที่ศึกษา ผู้วิจัยสมมติให้ความเร็วก่อนกระทบ v_1 และความเร็วหลังกระทบ v_2 เป็นไปตามความสัมพันธ์ต่อไปนี้

$$v_{2,\perp} = -k_\perp v_{1,\perp} \tag{13}$$

$$v_{2,//} = k_{//} v_{1,//} \tag{14}$$

เมื่อ k คือสัมประสิทธิ์การกระทบระหว่างอนุภาคกับอิเล็กโตรด ดัชนีล่าง $\perp$ และ $//$ ในสมการ (13) และ (14) ระบุค่าของสัมประสิทธิ์การกระทบในแนวตั้งฉากและขนานกับระนาบอิเล็กโตรดตามลำดับ ในการวิเคราะห์การเคลื่อนที่ของอนุภาค ค่า k ทั้งสองที่ใช้ในงานวิจัยนี้ได้จากการทดลองวัดจริง

พารามิเตอร์ที่ใช้ในการคำนวณ

รัศมีของอนุภาคอลูมิเนียม a = 0.403 mm, มุมระหว่างอิเล็กโตรด θ_0 = 3 องศา, สภาพยอมของสุญญากาศ $\varepsilon_0 = 8.854\times10^{-12}$ F/m, ค่าคงตัวไดอิเล็กตริกของตัวกลาง ε_s = 1, ความหนาแน่นอนุภาคอลูมิเนียม ρ_p = 2700 kg/m^3, ความหนาแน่นอากาศ ρ_s = 1.184 kg/m^3, สัมประสิทธิ์แรงหนืดของอากาศ $\eta = 18.2\times10^{-6}$ Pa s, สัมประสิทธิ์การกระทบแนวตั้งฉาก $k_\perp$ = 0.6, สัมประสิทธิ์การกระทบแนวขนาน $k_{//}$ = 0.7, แรงดันไฟฟ้าที่จ่ายให้กับระบบอิเล็กโตรด V = 4 kV., หนึ่งช่วงเวลาคำนวณ Δt = 10 μs

4. การทดลองการสังเกตการเคลื่อนที่ของอนุภาค

การสังเกตพฤติกรรมการเคลื่อนที่ของอนุภาคแสดงในรูปที่ 4 อิเล็กโตรดไฟฟ้าแรงสูงได้รับแรงดันจากเครื่องกำเนิดสัญญาณ (Tektronix รุ่น AFG 3021B) และเครื่องขยายแรงดันไฟฟ้า (Trek รุ่น 610E) โดยสัญญาณขาออกจากเครื่องขยายแรงดันผ่านตัวต้านทานจำกัดกระแส 10 MΩ อิเล็กโตรดที่ใช้มีการตัดให้เป็น Rogowski Profile ที่ขอบเพื่อหลีกเลี่ยงค่าสนามไฟฟ้าสูงที่ขอบอิเล็กโตรดซึ่งอาจทำให้เกิดประจุค้างในระบบอิเล็กโตรดได้ พฤติกรรมการเคลื่อนที่ของอนุภาคนั้น บันทึกด้วยกล้องวีดีโอ CCD camera (WAT-902H Ultimate, Watec) ซึ่งต่อกับเครื่องคอมพิวเตอร์ อนุภาคที่ใช้ทำจากอลูมิเนียม รัศมี 0.403 mm ซึ่งมีขนาดต่ำกว่า 1 mm ตามวัตถุประสงค์ของการศึกษา (ผู้ผลิต Bal-tec Div.) อิเล็กโตรดในการทดลอง แสดงในรูปที่ 5

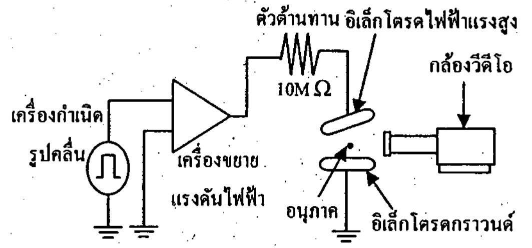

รูปที่ 4 แผนภูมิการจัดเตรียมการทดลอง

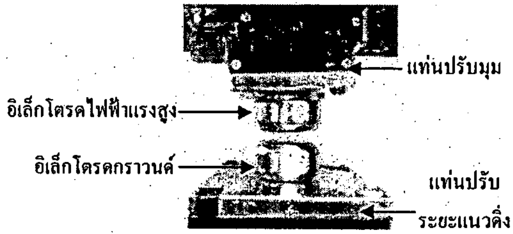

รูปที่ 5 ระบบอิเล็กโตรด

ในการทดลองผู้วิจัยใช้ฉนวนพอลิเมอร์ Polydimethylsiloxane (PDMS) หนา 0.03 mm (ผู้ผลิต Shin Etsu) วางบนอิเล็กโตรดกราวนด์ด้านสนามไฟฟ้าต่ำกว่าตำแหน่งเริ่มต้นของอนุภาค เพื่อหยุดการเคลื่อนที่ของอนุภาค อนุภาคถูกวางที่ตำแหน่งเริ่มต้น x_p = 106 mm และ θ_0 = 3° ทำการจ่ายแรงดันไฟฟ้ารูปคลื่นสี่เหลี่ยม แรงดันไฟฟ้า 4 kVpeak เป็นเวลา 500 ms การสังเกตพบว่า อนุภาคถูกยกขึ้นจนกระทบอิเล็กโตรดบน และกระดอนลงมากระทบอิเล็กโตรดล่าง และถูกยกขึ้นอีกครั้ง เป็นเช่นนี้จนกระทั่งอนุภาคหยุดบน PDMS ภาพจากวิดีโอของอนุภาคที่บันทึกแสดง ในรูปที่ 6ก และ 6ข ระยะกระจัด Δx_p ในแนวระนาบจากตำแหน่งเริ่มต้นในรูปที่ 6ก ถึงตำแหน่งที่อนุภาคกระทบอิเล็กโตรดกราวนด์เป็นครั้งที่สองและหยุดในรูปที่ 6ข มีค่าเท่ากับ 0.75 mm

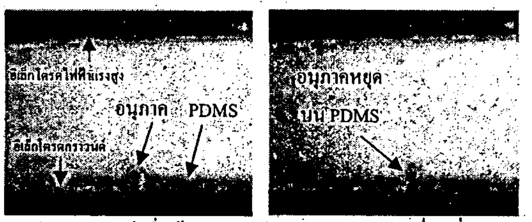

(ก) ตำแหน่งเริ่มต้น (ข) หยุดการเคลื่อนที่

รูปที่ 6 การทดลองระยะการเคลื่อนที่ของอนุภาค

5. ผลการจำลองการเคลื่อนที่ของอนุภาค

หัวข้อนี้แสดงเส้นทางการเคลื่อนของอนุภาคอลูมิเนียมในแกน x และ z เมื่อตำแหน่งเริ่มต้นของอนุภาค x_p = 106 mm ที่ได้จากการจำลอง ผู้วิจัยพบว่าเมื่ออนุภาคถูกยกขึ้นจนกระทบกับอิเล็กโตรดบนและกระดอนกลับลงมากระทบอิเล็กโตรดล่าง ผลของแรงทางไฟฟ้าและคุณสมบัติการกระทบทำให้อนุภาคเคลื่อนที่ไปยังบริเวณที่มีสนามไฟฟ้าที่ต่ำกว่า และใช้เวลาการเคลื่อนที่เท่ากับ 0.24 วินาที ดังแสดงในรูปที่ 7 จากการจำลอง อนุภาคมีระยะกระจัด Δx_p มีค่าเท่ากับ 0.83 mm ซึ่งแตกต่างจากการทดลอง 9.6% แสดงในรูปที่ 8

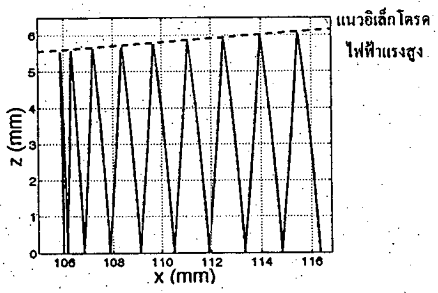

รูปที่ 7 ผลการจำลองการเคลื่อนที่ของอนุภาค

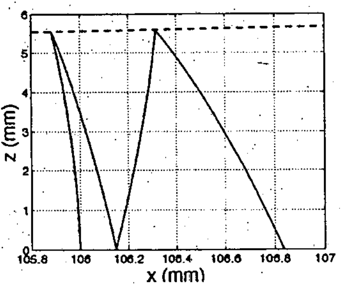

รูปที่ 8 แนวการเคลื่อนที่ของอนุภาคข้ามแกปในสองรอบแรก

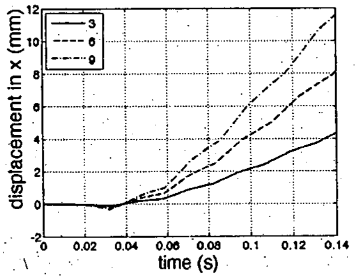

รูปที่ 9 ระยะกระจัดของอนุภาคในแนวระดับ (จากตำแหน่งเริ่มต้น) เมื่อ $\theta_0 = 3°, 6°$ และ 9°

เมื่อเปรียบเทียบผลสำหรับผลของความหนืดของอากาศ การจำลองที่ได้จากการพิจารณาและไม่พิจารณาความหนืดพบว่า ระยะกระจัดการเคลื่อนที่ของอนุภาค เมื่ออนุภาคกระทบอิเล็กโตรดกราวนด์เป็นครั้งที่ 9 มีค่าแตกต่างกันเพียงเล็กน้อย หรือประมาณ 0.14%

นอกจากนี้ผู้วิจัยได้ศึกษาผลของมุม θ_0 ระหว่างอิเล็กโตรด เมื่ออนุภาคมีตำแหน่งเริ่มต้นที่ได้รับความเครียดสนามไฟฟ้าเท่ากัน โดยที่ θ_0 เท่ากับ 3, 6 และ 9 องศา ระยะกระจัดในแนวแกน x ที่อนุภาคเคลื่อนที่ไปได้ เทียบกับเวลาของการเคลื่อนที่แสดงในรูปที่ 9 ผู้วิจัยพบว่าเมื่อมุมระหว่างอิเล็กโตรดเพิ่มขึ้นทำให้ระยะกระจัดในแนวระนาบของการเคลื่อนที่ของอนุภาคเพิ่มขึ้นด้วยเช่นกัน

6. สรุปผล

การศึกษาพบว่า เมื่ออนุภาคถูกยกขึ้นด้วยแรงทางไฟฟ้าจนกระทบอิเล็กโตรดบนและกระดอนกลับลงมากระทบอิเล็กโตรดล่าง ผลของแรงทางไฟฟ้าและคุณสมบัติการกระทบทำให้อนุภาคเคลื่อนที่ไฟยังบริเวณที่มีค่าสนามไฟฟ้าต่ำกว่า จากผลการคำนวณและการทดลองพบว่าระยะกระจัดในแนวระนาบเมื่ออนุภาคกระทบกับอิเล็กโตรดกราวนด์เป็นครั้งที่สองมีค่าใกล้เคียงกัน ความคลาดเคลื่อนเท่ากับ 9.6% ผลของมุมระหว่างอิเล็กโตรดเมื่อมีค่าเพิ่มขึ้นทำให้ระยะกระจัดในแนวระนาบของการเคลื่อนที่ของอนุภาคเพิ่มขึ้นเช่นกัน ถ้าตำแหน่งเริ่มต้นของอนุภาคมีค่าสนามไฟฟ้าเท่ากัน

7. กิตติกรรมประกาศ

งานวิจัยนี้ได้การสนับสนุนทุนวิจัยจาก "ทุนอุดหนุนวิทยานิพนธ์สำหรับนิสิต" บัณฑิตวิทยาลัย จุฬาลงกรณ์มหาวิทยาลัย

เอกสารอ้างอิง

[1] K. Sakal, S. Tsuru, D.L. Abella and M. Hara, *IEEE Trans. Electrical Insulation*, vol. 6, pp. 122-130, 1999.

[2] K. Sakal, D.L. Abella, Y. Khan and M. Hara, *IEEE Trans. Electrical Insulation*, vol. 10, pp. 418-424, 2003.

[3] M. Hara and et al., *J. Electrical.*, Vol. 2, No. 3, pp. 223-239, 1977.

[4] Thomas B Jones, "Electromechanics of Particle," Cambridge University Press 1995, Chapter 1-3.

[5] K. Sakal, D.L. Abella, J. Suehiro and M. Hara, *IEEE Trans. Electrical Insulation*, vol. 9, pp. 577-587, 2002.

นิศรุต พันธ์ศิริ จบปริญญาตรีจากสถาบันเทคโนโลยีพระจอมเกล้าเจ้าคุณทหารลาดกระบัง คณะวิศวกรรมศาสตร์ สาขาวิศวกรรมอิเล็กทรอนิกส์ในปี 2551 ปัจจุบันศึกษาหลักสูตรวิศวกรรมศาสตร์มหาบัณฑิต ภาควิชาวิศวกรรมไฟฟ้า จุฬาลงกรณ์มหาวิทยาลัย

บุญชัย เตชะอำนาจ จบปริญญาตรีและโทจากจุฬาลงกรณ์มหาวิทยาลัย จบปริญญาเอกจาก Kyoto University ในปีพ.ศ. 2544 ในสาขาวิศวกรรมไฟฟ้า งานวิจัยที่สนใจคือวิศวกรรมไฟฟ้าแรงสูง